Antenna Laboratory Report No. 71-5

THE EFFECT OF COHERENCE AND MULTIPLE SCATTERING ON LASER RADAR AIR POLLUTION MEASUREMENTS

by

H. C. Sievering and R. Mittra

Scientific Report No. 16

June 1971

Sponsored by

National Aeronautics and Space Administration

NGR-14-005-009

Antenna Laboratory
Department of Electrical Engineering
Engineering Experiment Station
University of Illinois
Urbana, Illinois 61801

UILU-ENG-71-2544

Antenna Laboratory Report No. 71-5

THE EFFECT OF COHERENCE AND MULTIPLE SCATTERING ON LASER RADAR AIR POLLUTION MEASUREMENTS

by

H. C. Sievering and R. Mittra

Scientific Report No. 16

June 1971

Sponsored by

National Aeronautics and Space Administration

NGR-14-005-009

Antenna Laboratory
Department of Electrical Engineering
Engineering Experiment Station
University of Illinois
Urbana, Illinois 61801

UILU-ENG-71-2544

ACKNOWLEDGMENT

The work reported in this thesis was made possible through the contributions of a number of individuals and institutions. Support for this work was funded primarily by the National Aeronautics and Space Administration (Grant No. NGR 14 005 009) and the University of Illinois Industrial Affiliates Program on Electromagnetics.

Thanks are given to my major professor, Raj Mittra, for encouragement during the difficult parts of the work as well as for many informal discussions of the work--whether on the tennis court, or while jogging on the track behind MOG. Appreciation is also extended to Richard Semonin, Atmospheric Sciences Section of the Illinois State Water Survey for encouragement and support (National Science Foundation, NSF Grant GA-4576) during the early stages of the work. A number of discussions of theoretical concepts with V. Twersky of the Mathematics Department, University of Illinois, have been invaluable to this work. Earl Barrett of the Environmental Science Services Administration in Boulder, Colorado, has contributed a number of ideas on experimental problems associated with laser radar. The use of laboratory equipment (particularly the ruby laser) belonging to Professor C. Taylor of Theoretical and Applied Mechanics and the laboratory assistance of James Spinhirne has been greatly appreciated. Discussions with several members of the Antenna Laboratory and of Argonne National Laboratory have been quite useful. Many thanks are due to the staff of the G-20 computer for running the numerical programs on the machine.

The efforts of Rick Davis, Mr. Bela Sandorfi, Mrs. Margaret Hyde, and Mrs. Penny Thornbrugh in the careful preparation of the figures and in the typing and proofreading of the manuscript are appreciated.

This thesis is dedicated to my mother and father.

TABLE OF CONTENTS

LIST OF FIGURES

Figure | Page

Figure Page

LIST OF TABLES

1. REMOTE SENSING FOR AIR POLLUTION MEASUREMENTS

There are nine and sixty ways of constructing tribal lays,
And every one of them is right.

--Kipling

1.1 Introduction

As has been pointed out in the preface, day and night data about the concentration, spatial distribution, and diffusion fallout rates of pollutants under meteorological influences would be most beneficial. Conversely, the effects of pollution on meteorological climatological parameters must be determined. For example, the consequences of stratospheric pollution by supersonic transport flights can only be surmised.

Progress on these and many associated problems has been impeded by the lack of direct measurements of atmospheric parameters in three dimensions, over large volumes and with sufficient resolution in time and space. Remote sensing methods appear to offer solutions to this motley group of problems. However, of the nine and sixty techniques available, which does one choose? The transmitter alone--basic to any remote sensing method--raises a number of questions. Should it be active or passive; continuous or pulsed; ground based, airborne, or on board a satellite? The first section of this chapter will give a brief description of the various remote sensing methods. The second section will consider their applicability to air pollution measurements.

1.2 Atmospheric Remote Sensing Techniques

Until recently, the study of wave propagation in the atmosphere has emphasized the "deleterious" consequences of that propagation. Studies

have generally considered the analysis of the degradation of electromagnetic waves with passage through an air mass and minimization of this degradation. Remote sensing, on the other hand, is concerned with maximizing the air mass information one can glean from analysis of the "degraded" electromagnetic wave. For this reason, the theory of remote sensing is still in an early stage of development.

Remote sensing--encompassing any observation in which the sensor is not in direct contact with the object of study--can be divided into two classes: active and passive. An active system involves transmission of a signal, interaction with a target, and quantitative as well as qualitative detection. A passive system involves the detection of natural emanations of the target and in no way interacts with it.

Because passive systems require only moderate power and size, they have been extensively used in spacecraft. Active systems, requiring large amounts of power and massive components, are practical from stations on the earth's surface.

1.2.1 Active Systems

Active systems have potentially greater information content due to one's control over the probing signal. Present active sensing techniques can loosely be grouped into five categories:

1. Radar
2. Laser radar
3. Acoustic
4. Microwave line-of-sight propagation
5. Optical and infrared line-of-sight propagation.

1.2.1.1 Radar

The radar technique is characterized by energy scattered off of dielectric inhomogeneities present in a limited atmospheric volume. Measurements of the echo power, Doppler shift, polarization, and attenuation along the path allow interpretation of the state of the probed medium.

The primary radar measurements are reflectivity and Doppler shift. Reflectivity measurements can be related to the size and number of particles giving rise to the echoes. Doppler shift measurements allow for the measurements of atmospheric motions. Two secondary measurements should be mentioned: Bistatic Radar (i.e., angular separation of transmitter and receiver) and concomitant measurement of polarization effects which give an indication of particle shape. Recent theoretical work indicates that particle size distributions may also be obtained from bistatic radar. Measurement of the path attenuation due to absorption by atmospheric constituents may allow determination of total or height discriminated concentrations. At normal radar wavelengths only water vapor concentration measurements appear feasible.

Recent attention has been given to a study of scattering from sharp gradients of refractive index. Radar determinations of the cross section per unit volume of a refractively perturbed medium can be used to obtain the intensity of refractive index fluctuations. While some powerful radars have had sufficient sensitivity to detect the relatively weak refractive index perturbations which commonly mark interfaces across which the mean refractivity changes sharply, none have had both sufficiently high resolution and sensitivity to detect the fine-scale structure of the scattering medium. The combination of great sensitivity and ultra-high

resolution has recently been achieved by Atlas et al.[1] This has been made possible by the use of a unique frequency-modulated, continuous wave radar developed by Atlas et al.[1]

A second area of recent interest is large-scale radar mapping. A major reason for its importance is the need for the collection of data which is on a scale and with coverage either prohibitively expensive or nearly impossible by conventional means. Meteorological measurement requirements can no longer be met by any system of in situ sensors. Weather prediction as well as maximum allowable pollution concentrations requires large-scale quantitative data. Both satellite radar and the correlation of data obtained by many surface-based stations suggest themselves as possible approaches. However, the first suffers from the inherent problem of discriminating ground from atmospheric returns.

1.2.1.2 Laser Radar

Laser radar is very similar in operation to radar, for the backscattered signal as a function of range is observed upon transmission of a short pulse of radiation. The major difference is in the operating wavelength. A Q-switched ruby or neodymium laser of 6943 Å and 10600 Å, respectively, is the source. Being in the optical range of the spectrum, backscattered energy is collected at a telescope, passed through collimating optics and a narrow band optical filder centered at the laser wavelength, and detected by a photomultiplier tube.

Backscatter from the atmosphere can occur in any one of three ways: off atmospheric molecular constituents, off natural aerosols and pollutant particulates, and off refractive index variations. The signal level return from refractive index variations is far below that from either atmospheric constituents or pollutant particulates. In the lower atmosphere (below

25 km) both aerosol/pollutant and molecular backscatter are observed. Above 25 km the scatter is mainly molecular and thus allows for air density determination.

As in radar, bistatic laser radar permits measurement of the polarization dependence of the scattered signal. These measurements can, in theory, give information about the concentration and size distribution of the scatterers.

Schotland et al.[2] suggest that Doppler techniques could be applied to determine temperature from the width of the molecular scattering spectra as well as wind velocity from the mean Doppler shift.

Recent laser radar experiments have been concerned with shifted wavelength signal returns. Two approaches appear to be particularly promising: (1) absorption in which the difference in signal return from a laser radar "tuned" to and away from atmospheric absorption lines is observed, and (2) Raman scattering in which the scattered energy is frequency shifted and the shifted wavelength signal return, unique to a specific atmospheric constituent, is observed.

1.2.1.3 Acoustic

In remote probing of the atmosphere by electromagnetic waves, the interaction with the gases of the lower atmosphere (excluding water vapor) is generally very weak. Thus sensitive and sophisticated equipment is required to measure the interactions. However, the interaction of acoustic (longitudinal pressure) waves with the atmosphere is very strong. Thus, the propagation of these waves is strongly affected by atmospheric wind, temperature, and humidity. Until recently,[3,4] this fact has been little exploited. Partially due to concern for identification of acoustic waves of natural origin, for which the power radiated

is quite low, studies have focused on passive remote sensing for turbulence measurements.[5]

The potential of active remote sensing with acoustic scattered energy for atmospheric information has been considered by Little.[3] Under the conditions of complete measurement of scattered power as a function of wavelength and scattered angle, atmospheric information on the following could be obtained:

a. the intensity of temperature fluctuations, which is directly proportional to the refractive index;

b. the intensity of velocity fluctuations as a function of direction and height. These three-dimensional data are useful in determining atmospheric turbulence and diffusion;

c. the mean wind speed and direction may be obtained from Doppler shift or bistatic acoustic measurements;

d. the time history of temperature inversion layers including intensity can be observed.

The major limitation in the use of acoustic probing is its short range capability. 1500 m heights is a probable limit on range for meaningful atmospheric information content. Of course, it complements radar in that very short ranges (down to 30 m) can be realized.

1.2.1.4 Microwave Line-of-Sight

Wave propagation from one location to another is affected by the refractive index. For electromagnetic waves greater than 1 mm, the refractive index is a function of temperature, pressure, and water vapor content.

The perturbation due to refractive index fluctuations is well enough understood to allow: (1) total oxygen and water vapor concentrations

integrated across the propagation path, and (2) the amplitude of refractive-index fluctuations and the spectral distribution and internal rate of change of refractivity.

Although most measurements are carried out on a horizontal basis, satellite-to-ground measurements have been made in a more limited context. When absorption becomes comparable to refractive effects, the above no longer holds. However, absorption effects have application in the determination of water vapor content.

1.2.1.5 Optical and Infrared Line-of-Sight

The major atmospheric measurements obtainable by this technique are turbulence and wind structure, and path-averaged temperature and gas densities. Thermal inhomogeneities allow for the ability to measure turbulence structure, as do refractivity irregularities in giving rise to wind structure measurements. Measurement of optical path length gives a straightforward manner of obtaining average temperature. To measure gas densities, tunable transmitters are needed. Two transmission wavelengths, one on and one off an absorption line, are compared to give the path averaged density of an atmospheric gas. Because of the very high sensitivity of this technique, it appears feasible that very rare gases and very low pollutant gas concentrations may be observed using short paths.

1.2.2 Passive Systems

Several sources for passive system operation exist. The transmitted and scattered radiation from the sun, the moon or the earth can be observed by a passive system. Passive systems also can utilize the natural emanations from gas or aerosol constituents of the atmosphere. Passive systems

can be grouped into two categories:

1. Infrared optical

2. Microwave radiometric.

1.2.2.1 Infrared Optical

The absolute temperature of a body and its coefficient of emissivity determine the radiating properties of any object. At earth surface temperatures of approximately 300°K, the intensity maximum of thermal radiation falls between 10 and 20 microns. Thus, infrared probing appears the obvious choice for radiation measurements of the earth's surface or atmosphere. Conversely, at wavelengths below about three microns solar energy reflected from the surface of the earth is greater than the thermal emission from the earth and atmosphere. Generally, thermal radiation can be neglected below about two microns and optical probing assumed to be measuring only reflected solar energy.

Most applications of infrared optical probing have emphasized global meteorological measurements. Thus, satellite systems have received most attention. The theory of infrared probing has dealt mainly with atmospheric thermal structure inference by inversion of radiation measurements[8] and earth surface or cloud-type properties by multiwavelength observation.[9] Since interest is here focused on atmospheric measurements, nothing further will be said of the second category.

The most useful passive infrared technique is the inference of vertical profiles of temperature, water-vapor content, and ozone content.[10] The accuracy of atmospheric inferences by inversion techniques is, however, not as great as one might at first suspect. It is normally said that the accuracy of inversion techniques is limited by the number of viewing channels of the observing equipment (n pieces of information

allowing inference of n characteristics of atmospheric structure) and its accuracy (i.e., signal-to-noise ratio of the observational data). However, as Twomey[11] points out, the number of pieces of information obtained is usually far less than the number of viewing channels available.

A second important method of passive infrared probing is that of interferometry. In theory, infrared interferometry (also called Fourier spectroscopy) is also an inversion technique. Instead of sensing at preselected wavelengths or bands of wavelengths, the sensor records a pattern of interference maxima and minima which can be converted to the more conventional spectrum of wavelength versus intensity. Numerous spurious effects are present, some of which cannot easily be corrected.

1.2.2.2 Microwave Radiometric

The microwave radiometric method of probing the atmosphere measures the properties of thermal emission and absorption by the atmosphere itself. The intensity, spectrum, and polarization of the radiation as measured by the microwave radiometer (now among the most sensitive electromagnetic detectors) can provide atmospheric constituent profiles, temperature profiles, and, possibly, pollutant profiles as well.

Microwave probing is generally subdivided into ground and satellite-based measurements. Ground measurements may utilize either emission by the atmosphere or absorption of an external source of microwave emission. The theoretical potential of satellite sensors for water vapor and oxygen profiles appears good, particularly when its all-weather capabilities are considered. No experiments have, however, been flown. Thus, satellite microwave detection must be considered as conjecture.

Ground-based emission measurements provide most microwave atmospheric data. Data near five mm wavelength measure thermal emission by molecular oxygen. By shifting the wavelength from a resonant frequency of oxygen to a wavelength in the clear of absorption, the probing range can be varied. This allows for temperature profile determination. Emission observations at wavelengths near 1.35 cm detect water vapor thermal emission and thus a capability for water vapor profile data.

Absorption measurements can give detectable signals with smaller amounts of a constituent present than can emission measurements. Thus, in addition to water vapor, oxygen, and ozone measurements, trace constituents may be observed through the use of absorption techniques. Examples might be SO_2, CO, NO, and NO_2. The major limitation in the use of this technique is the need for an external emission source. Thus, atmospheric observations are line-of-sight path to the sun.

A technique which utilizies both passive and active systems is crossed-beam correlation. It employs two detecting systems with view fields that intersect. Turbulence-induced fluctuations result in fluctuations in the detector output signals. By cross-correlating the detector signals, information relating to the intensity of fluctuations, the wind speeds, and the spectrum of turbulence can be obtained. Oftentimes, the magnitude of the correlated signal is far down from that of the uncorrelated signal. Under this condition active probing systems must be used.

1.3 Applications to Air Pollution Measurements

The present capabilities of remote sensing, as described in section 1.2, indicate that emphasis has been placed on measurement of meteorological

parameters without much consideration for its use in air pollution analysis. Also, research is being carried on in a fragmented fashion. That remote meteorological measurement schemes are in a sophisticated stage of development is certain, but techniques which measure the same or interdependent parameters must be better coordinated. A facility at which the various measurement schemes can be correlated would be highly desirable. Although greater consideration for the impact of meteorological measurements on air pollution parameters is needed, the measurement schemes themselves are progressing well.

What of the use of remote sensing for direct air pollution measurements? Until recently, little attempt has been made to sophisticate this purpose. A survey of pollutants by type and by their scattering, absorption and emission characteristics is in order.

Air pollutants can occur in the form of gases, solid particles, or liquid aerosols. These forms can exist either separately or in combinations. Gaseous pollutants constitute about 90 per cent of the total mass emitted to the atmosphere, while particulates make up most of the rest. Given suitable conditions, many of the primary pollutants will participate in reactions in the atmosphere that produce secondary pollutants such as are found in photochemical smog. The most important pollutant types are:

a. Particulates including carbon fly ash, lead, zinc oxide, and arsenic.

b. Nitrogen compounds including NO, NO_2, NO_3, HNO_2, and HNO_3.

c. Sulfur compounds including SO_2, SO_3, and H_2SO_4.

d. Carbon compounds including CO, CO_2, and CH_4.

e. Oxygen compounds; in particular O_3.

In addition, hydrogen chloride and other halogen compounds, ammonia, and peroxyl acetyl nitrate (PAN) are important pollutants to be measured and monitored.

1.3.1 Pollutant Particulates

The types of atmospheric particles and their size ranges are shown in Figure 1. Aerosol particles, including pollutant particulates, are not equally distributed in size. The atmosphere's carrying capacity is far greater for smaller particles than for larger ones. A typical size distribution plot[12] is shown in Figure 2, with an approximation to the curve also indicated. The approximation to the curve is the Junge distribution $\frac{dN}{d(\log r)} = \gamma r^{-\nu}$. For most lower atmospheric distributions, $\nu = 3$. Scattering intensity is a function of the particulate number concentration, size distribution, shape and absorption/emission characteristics. Pollutant particulates are generally passive scatterers and because of their high relative number densities and random shape can be assumed to exhibit no shape characteristics in the scattering process. That is, an ensemble of randomly shaped particles is equivalent to the same number of spherically shaped particles of a specified mean diameter. The question then remains as to which wavelength will optimize pollutant particulate signal detection.

In meteorological radar measurements of cloud water droplets, rain drops, snow crystals, and hailstones, optimum wavelengths are on the order of 1 cm. The drops detected have a geometric-mean diameter of 0.1 cm. The ratio of wavelength to diameter is thus of order ten. Since the geometric-mean diameter of atmospheric particulates is of the order of 0.1 microns, it would follow that an optimum transmitter wavelength

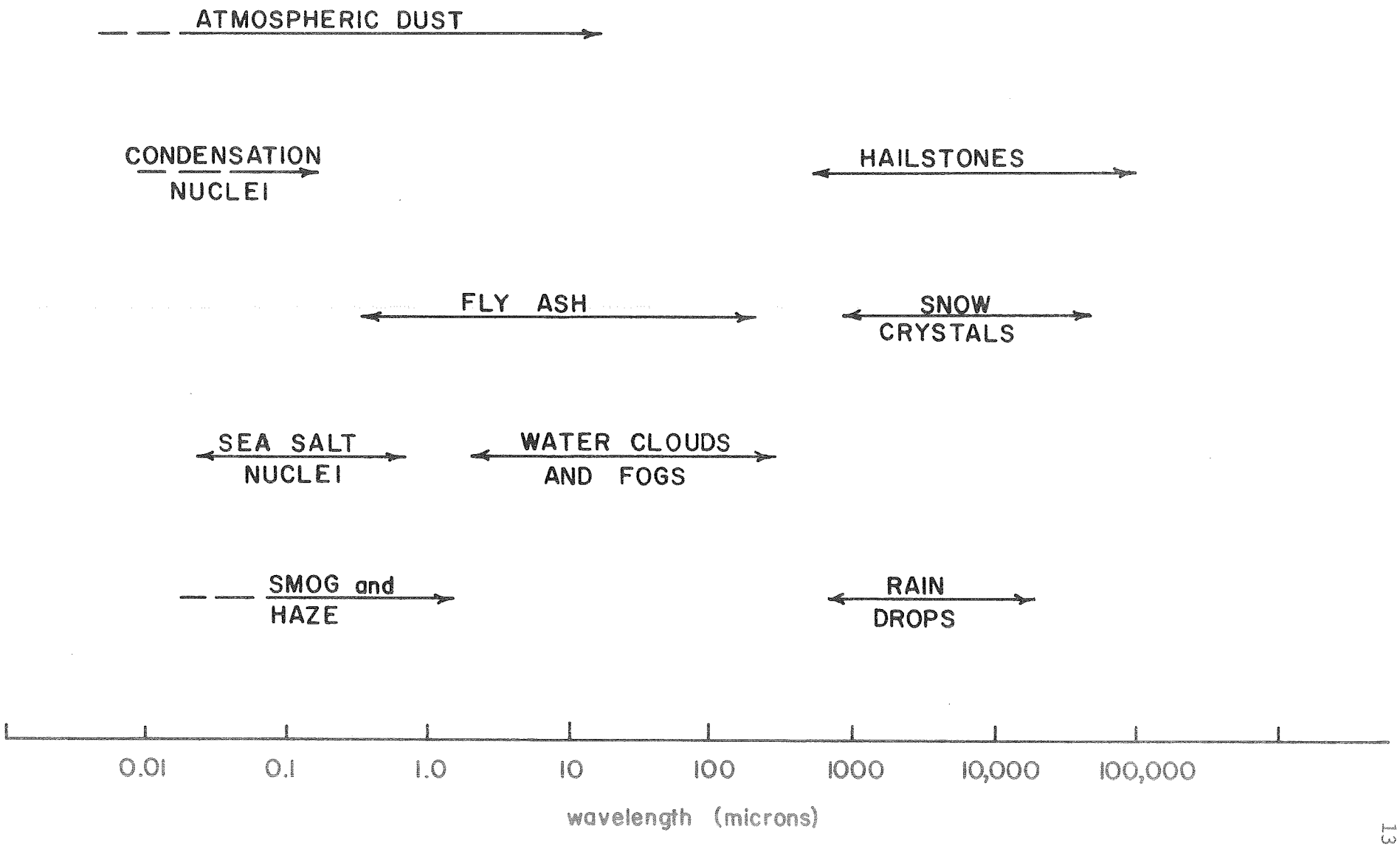

Figure 1. Relation of transmitter wavelength to diameter of atmospheric particles.

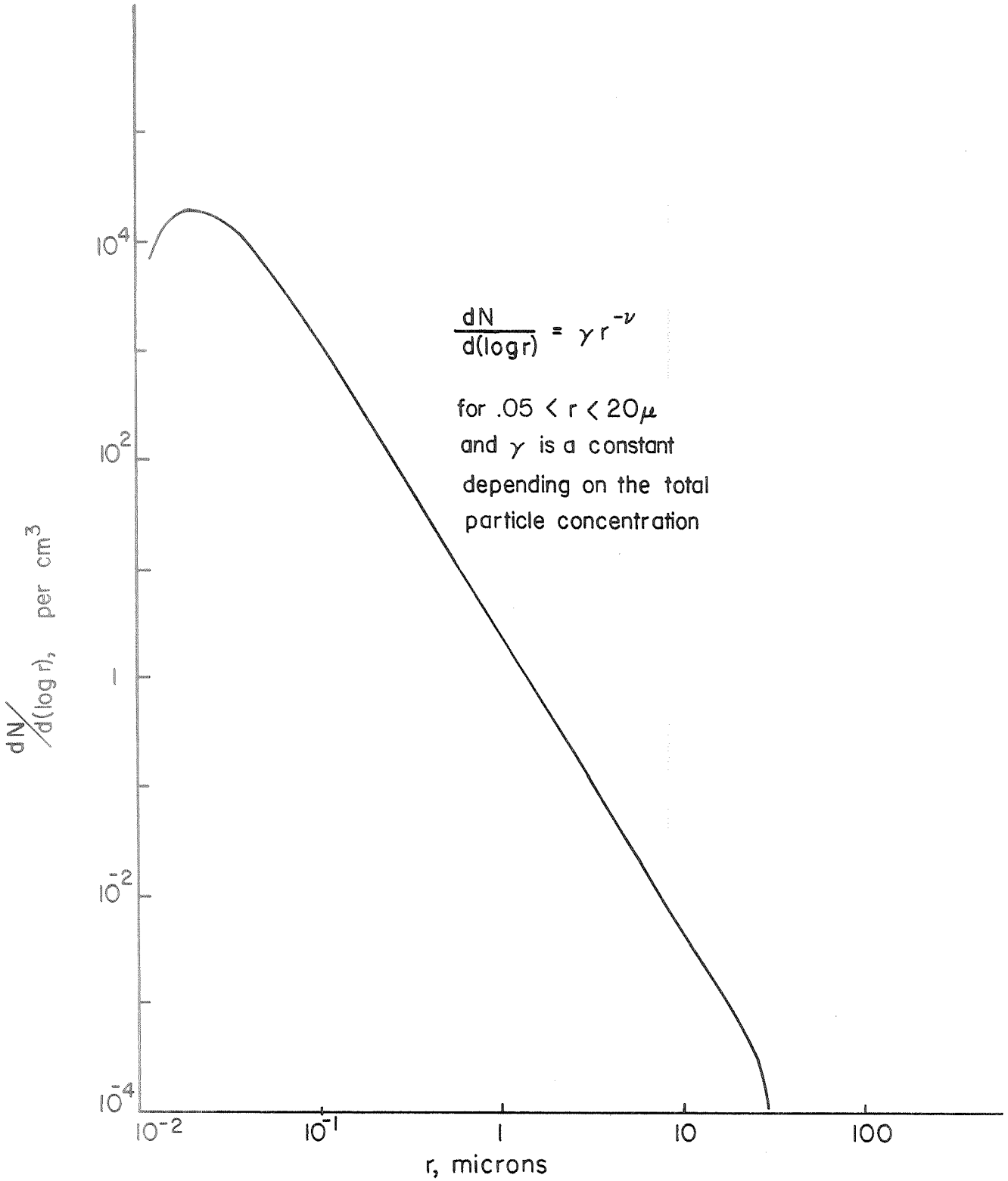

Figure 2. Aerosol size distribution in continental air.

for pollutant particulate remote detection is 1 micron. For those familiar with electromagnetic wave scattering processes, this result might well be expected. When the wavelength of electromagnetic radiation is on the order of the scattering particle diameter, the scattering cross section per particle may be as much as 10^{18} larger than at a wavelength far removed from the particle diameter.

Assuming an optimal wavelength near 1 micron, several techniques appear as possible candidates:

1. Passive satellite optical probing
2. Passive or active correlation techniques
3. Optical infrared line-or sight
4. Laser radar.

Passive satellite probing and line-of-sight measurements have limited use because of the small value of volume extinction coefficient. The extinction of a monochromatic beam propagating in a scattering medium is given by

$$dI(\lambda) = -B_{ext.}(\lambda,n)\ I(\lambda)\ dr \qquad (1)$$

where the intensity $I(\lambda)$ of the beam is defined as the energy per unit bandwidth, at wavelength λ, transmitted per second through a unit area normal to the propagating direction; dr is the amount of scatterer in a volume of unit cross sectional area and length dl; and $B_{ext.}(\lambda,n)$ is the volume extinction coefficient (per unit length) for scatterers with index of refraction $n = m_1 + im_2$. Long and Rensch[13] have calculated $B_{ext.}$ for a Junge distribution with a particulate concentration of 10^9 per m^3 and relative humidity of less than 90 per cent. Results are shown in Figure 3. At a wavelength of one micron ($B_{ext.}$ being 0.02/km),

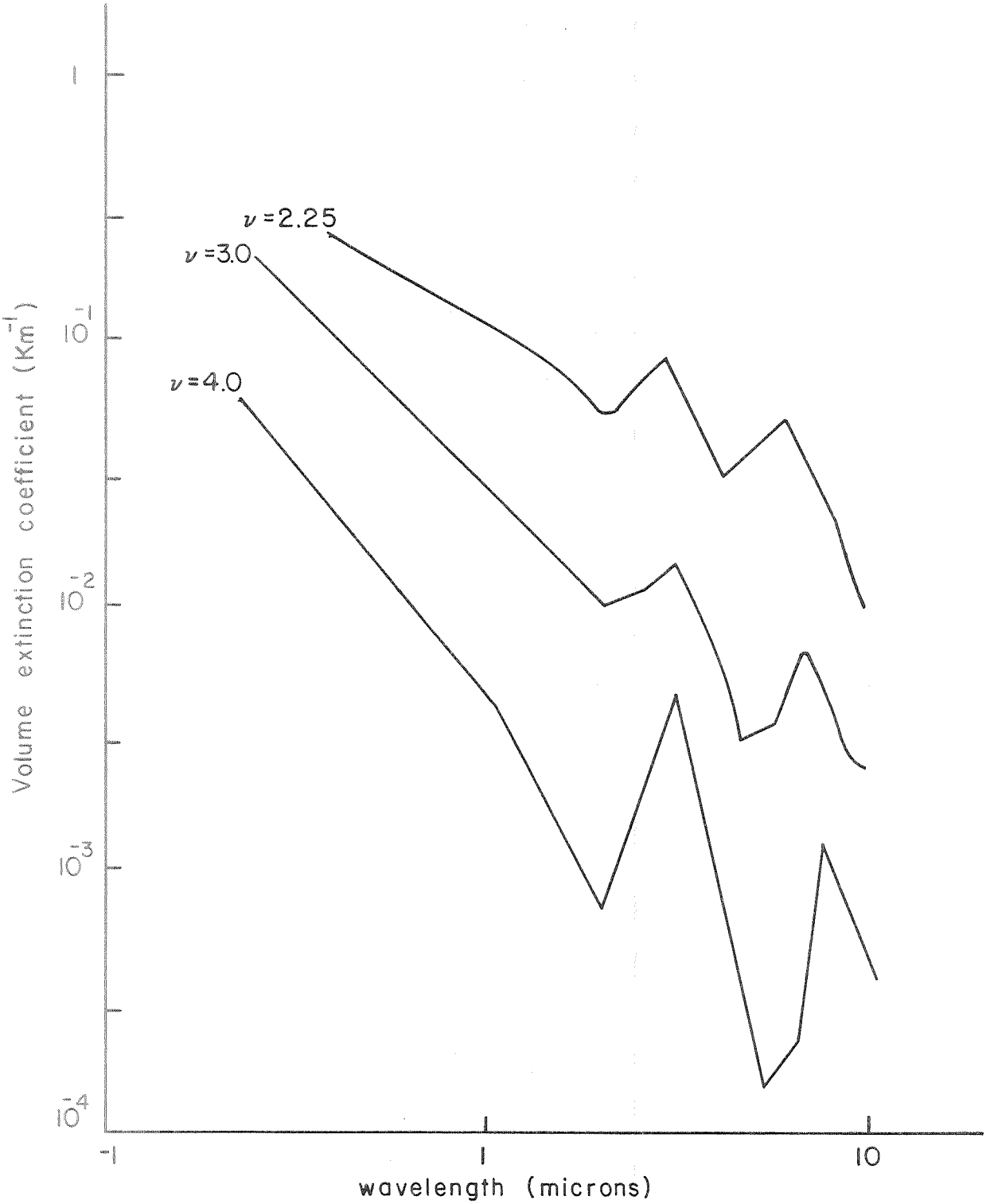

Figure 3. Volume extinction coefficient vs. wavelength for aerosol model with relative humidity <90 per cent and aerosol concentration of $10^9/m^3$.

an approximate 0.002/100 m signal change in the first several hundred meters can be expected. With the relatively short paths used in line-of-sight measurements, this technique will not allow for particulate measurements. Passive satellite probing can give total path particulate attenuation but cannot determine distribution along the path. Of course, this assumes a wavelength at which attenuation is due only to particulate scattering--a criterion not easy to meet. Satellite probing may thus be useful in particulate measurements only to the extent of mapping total atmospheric loading with no determination of height or time variations.

A consideration of the magnitude of backscatter coefficient indicates that more complete particulate measurements may be obtained by utilization of backscattered energy. The energy transfer equation relating source power to backscattered power received from a scattering volume[13] is

$$\Delta P_R(\lambda,180°) = WAT_1T_2\omega b_{sca.}(\lambda,m)\ \Delta l \qquad (2)$$

where $\Delta P_R(\lambda,180°)$ is the received backscatter power in watts from the scattering volume of length Δl(m), W is the irradiance incident on the scattering volume with area A($W/_m2$), T_1 is the transmittance between transmitter and scatter volume, T_2 is the transmittance between scatter volume and detector, ω is the solid angle subtended by detector (ster.) and $b_{sca.}(\lambda,m)$ is the backscatter coefficient $(km.ster.)^{-1}$ for scatterers with index of refraction $n = m_1 + im_2$. The backscatter coefficient can be written as

$$b_{sca.}(\lambda,m) = \frac{1}{K^2}\int_{r_1}^{r_2} |S(n,\lambda,180°)|^2\, N(r)dr \qquad (3)$$

where K is the free-space propagation constant (m^{-1}), $S(n,\lambda,180°)$ is the scattering amplitude function for a single particle,[14] and N(r) is the scatterer size density distribution with lower and upper radius limits of r_1 and r_2, respectively. An exact solution for $S(n,\lambda,180°)$ can be found using the classical boundary value method of Mie where an infinite set of eigenfunctions is used to represent the scattered field.[15] Calculations of $b_{sca.}$ were made by Long and Rensch[13] using the exact Mie theory and a Junge size distribution with r_1 = 0.1 microns and r_2 = 10.0 microns. The results are shown in Figure 4. Again note that a concentration of 10^9 per m^3 and relative humidity of less than 90 per cent were used.

At one micron wavelength $b_{sca.}$ is approximately 2.5×10^{-4} $(km\ ster.)^{-1}$ for $\nu = 3.0$. In a typical laser radar $W \tilde{\sim} 1$ megawatt, $A \tilde{\sim} 1m^2$ and $T_1 = T_2 = .98$ at one kilometer range, $\omega \tilde{\sim} 10^{-6}$ and $\Delta l \tilde{\sim} 1m$. Thus, $\Delta P_R(\lambda,180°)$ equals approximately 0.1 microwatt. This being far above the noise level of red sensitive multistage photomultiplier tubes, detection of pollutant particulates appears quite conducive to the laser radar technique. Note that vertical profiles can be obtained because of the relatively large signal returns from highly resolved (10 m or less because of the short pulses of laser light used) scattering volume heights.

As alluded to in Section 1.2.1, a problem does, however, present itself. So far, the backscatter power has been discussed only with regard to natural aerosols and pollutant particulates (i.e., particles for which Mie scattering applies). Since r_1 above was taken as 0.1 microns, no consideration was given to atmospheric molecular constituent scattering. Lawrence et al.[16] have calculated the variation in backscatter

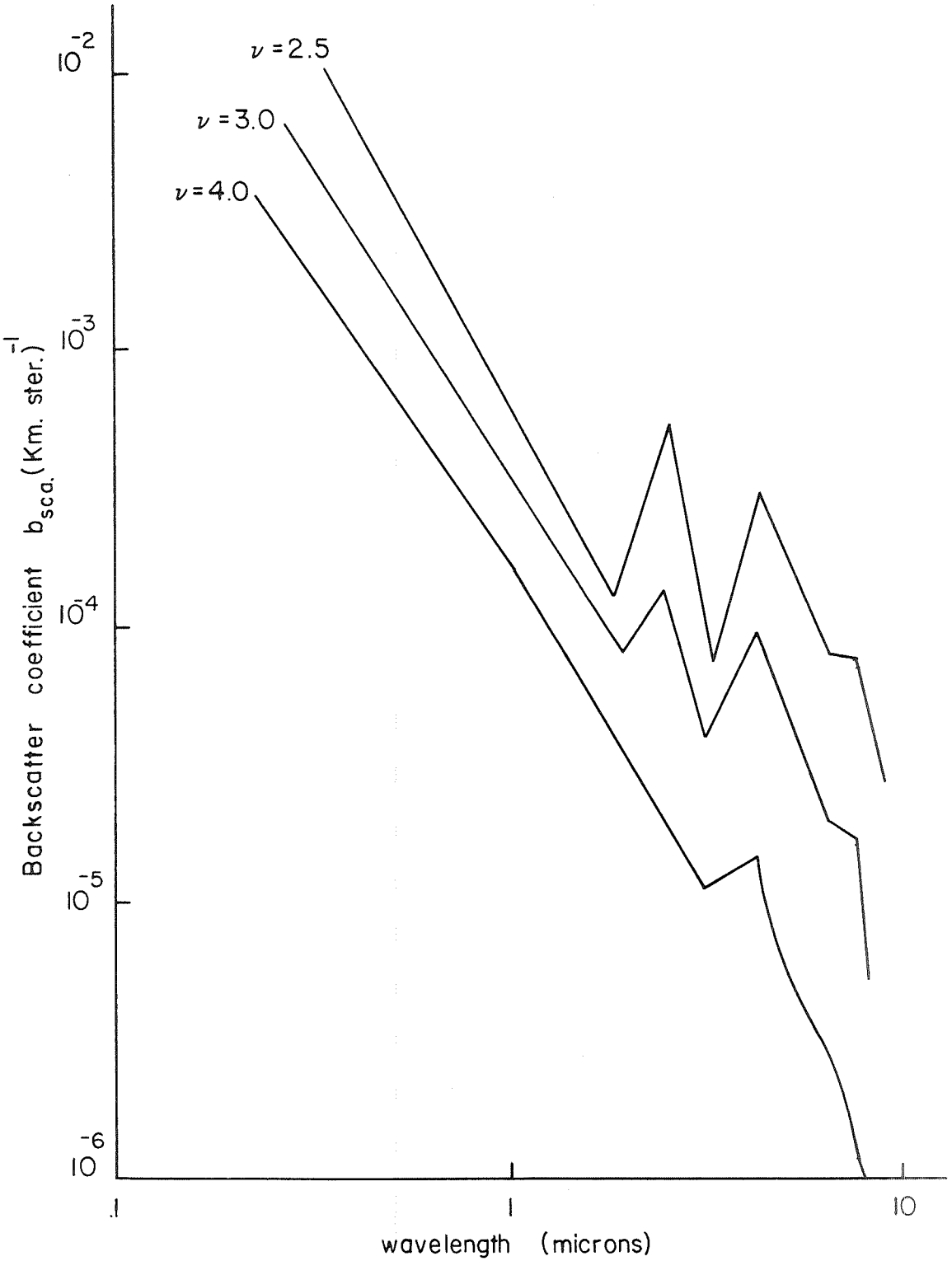

Figure 4. Backscatter coefficient vs. wavelength for aerosol model with relative humidity <90 per cent and aerosol concentration of $10^9/m^3$.

coefficient versus height for a clear atmosphere of natural aerosols and for a Rayleigh atmosphere (i.e., scattering particles much smaller than the wavelength as is true for the molecular constituents). Results are shown in Figure 5.

In a highly polluted atmosphere the Mie scattering curve may be 20 to 40 times the magnitude shown in Figure 5. Two questions thus arise. How does one discriminate backscatter contributed by pollutant particulates from that by atmospheric molecular constituents as well as from natural aerosols? Some researchers[17,18] have assumed the theoretical curves of Figure 5 as fitting the real atmosphere so that "background scattering" can be subtracted from the total observed scatter to give pollutant particulate concentrations.

Deirmendjian[19] and Penndorf[20] have analyzed the angular scattering properties of atmospheric Mie scatterers. These studies indicate that bistatic laser radar,[21,22,23] by measuring intensity and polarization of light scattered at angles other than 180°, may allow for the required discrimination. Measurements of the ellipticity of angularly scattered light which is initially linearly polarized can unambiguously be accounted for by aerosols and pollutant particulates since molecular (Rayleigh) scattering does not give rise to elliptical polarization (assuming no multiple scattering). Further, the ellipticity of angular scattering is sensitive to the size distribution and shape of aerosols and pollutant particulates, thus allowing for possible discrimination of these two scatterer types. However, again referring to Twomey,[11] bistatic laser radar cannot be expected to uniquely determine the size distributions or type of scatterer.

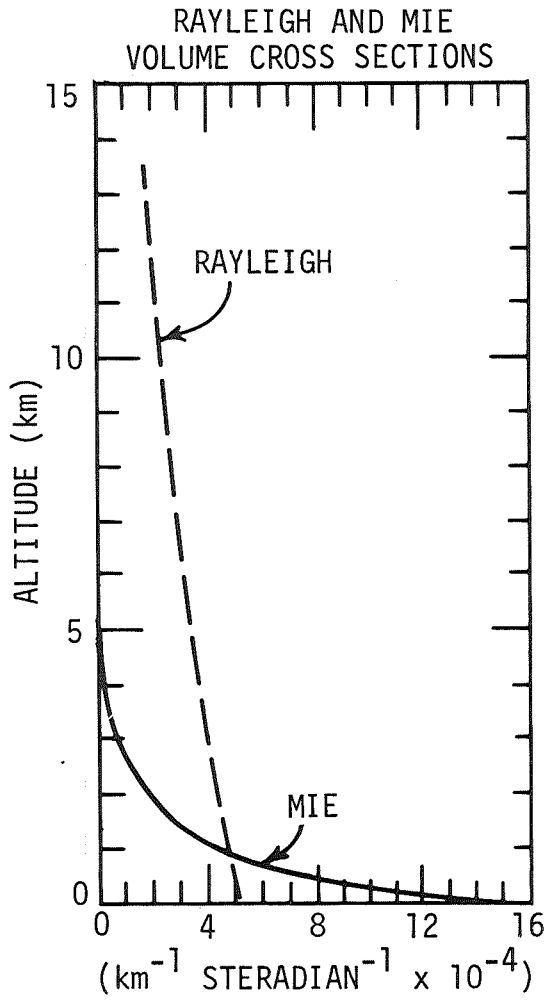

Figure 5. Backscatter coefficient vs. altitude at λ=0.7 microns.

Yet another technique (possibly used in conjunction with bistatic measurements) may achieve the desired discrimination. The laser radar equation, (2), assumes the scattering process to be an independent one. This implies the source illuminating the scattering volume of (2) to be an incoherent source. However, the laser is known to be a partially coherent source giving rise to partially dependent scattering processes (i.e., phase angle relationships between individual scatterers). This point will be expanded upon and pursued in ensuing chapters.

Although many interesting problems exist, remote sensing for pollutant particulates appears best suited to laser radar probing. The additional use of laser radar cross-correlation should prove of further significance in accurate pollutant particulate distribution observations.

1.3.2 Gaseous Pollutants

Gaseous pollutants give rise to molecular (Rayleigh) scattering. Since nonpollutant atmospheric constituents give rise to Rayleigh scattering which is of far greater magnitude than that caused by pollutant gases, scattering processes alone cannot be expected to allow discrimination and monitoring of these gaseous pollutants. However, absorption and re-emission processes may allow pollutant gas monitoring.

The absorption of energy by various chemical materials is based on Beer's Law. The monochromatic transmission, $\tau(\lambda)$, is given by

$$\tau(\lambda) = \frac{I(\lambda)}{I_o(\lambda)} = e^{-k(\lambda)pl} \qquad (5)$$

where $I(\lambda)$ is the transmitted portion of the monochromatic energy and $I_o(\lambda)$ is that portion incident on the gas layer. The partial pressure of

absorbing gas is p and the thickness of gas layer is one. The absorption coefficient, $k(\lambda)$, is a function of the gas observed, the operating wavelength, and total pressure present in the gas layer. The partial concentration of a gas can then be determined if the signal ratio at a particular wavelength where the ratio is not one is measured and if one knows which gas is present, its corresponding absorption coefficient, and the measurement path length.

If more than one gas is present, quantitative analysis requires a knowledge of which gases are present. A completely independent signal ratio must then be determined for every gas present. Although scattering has been assumed not to occur, this can easily be compensated for.[24]

Ludwig, Bartle, and Griggs[25] have tabulated the low resolution per cent radiance changes on passage through total clean and polluted atmospheres. Figure 6, taken from Ludwig et al., shows the results assuming a temperature profile of 1°C change per 100 meters with increasing temperature to 400 meters, decreasing temperature to 10 km, constant temperature to 25 km, and increasing temperature above this height. Also shown in Figure 6 are the assumed concentrations for various pollutants. The uppermost curve indicates the radiance change when all assumed pollutants are present. The other curves indicate the contribution to radiance change of individual pollutants. Of present interest is the fact that Ludwig et al. have concluded from these calculations that differences between the earth's temperature and that of pollutants play an important role in the quantitative determination of pollutant concentrations by radiance measurements. Temperature profiles are also necessary if quantitative measurements are to be achieved. Probably most important is the fact that considerable spectral interference can be seen to exist

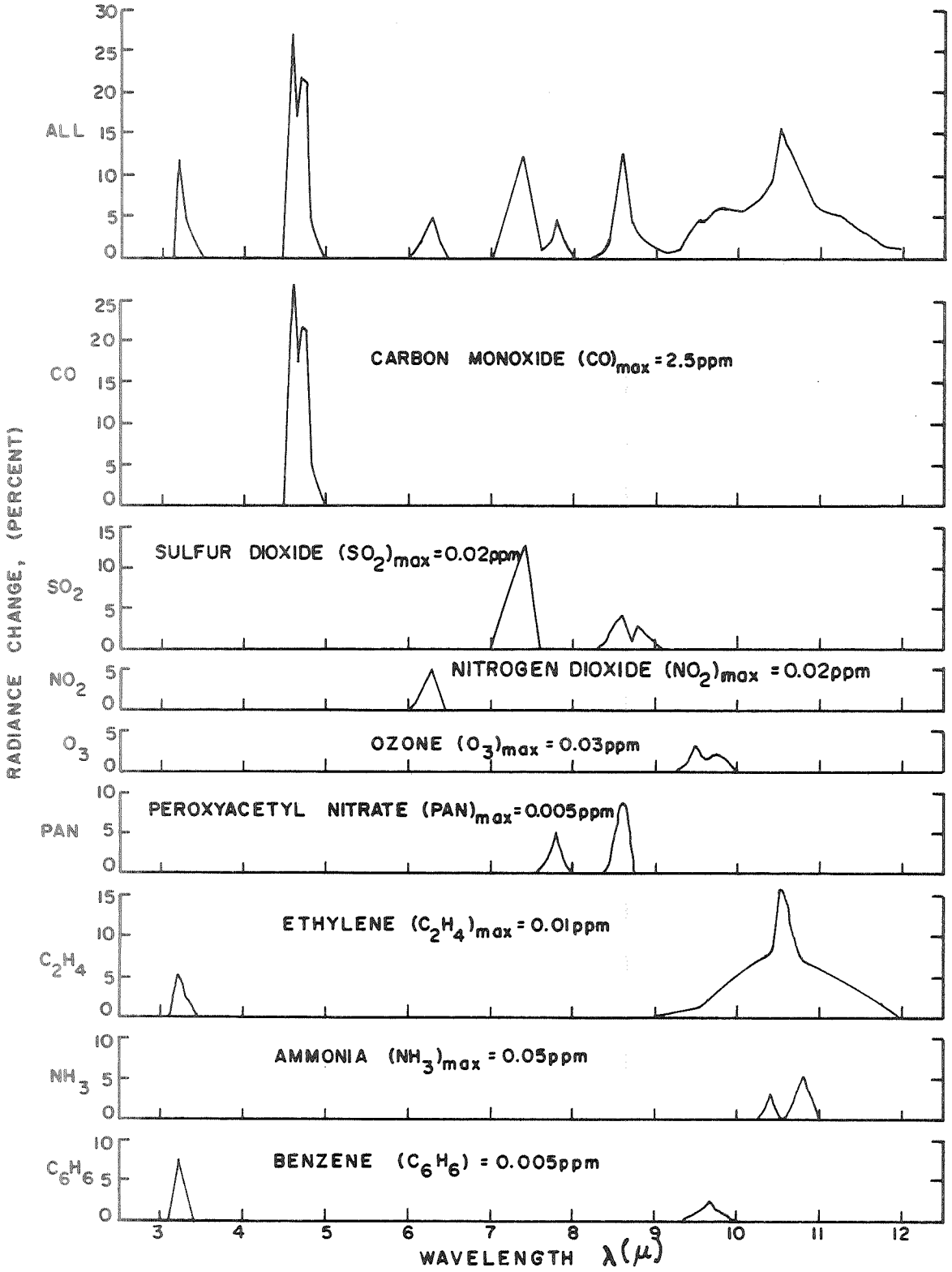

Figure 6. Per cent radiance changes between clear and polluted atmospheres.

between individual pollutants that are present in a typically polluted atmosphere. It would appear that higher spectral resolution experiments may allow for unique determination. An added benefit of high resolution experiments is larger values of absorption coefficients, possibly allowing shorter path measurements.

The most complete compilations of high resolution absorption spectra for pollutant gases are to be found in the articles of Long[26] and Hanst and Henson.[27] These tabulations indicate that almost all pollutants have strong high resolution absorption spectra in the near infrared between 2 and 25 microns. A number of pollutants also have absorption spectra in the microwave region. Due to pressure-broadening of these absorption lines, considerable overlapping of pollutant spectra occurs. Thus, overall pollution content may be determined by microwave measurements but no quantitative data on specific pollutants can be expected. Although overlapping of spectra occurs in the infrared as well, high resolution instrumentation available in the infrared should still allow discrimination of the various pollutants.

As example spectra, Figures 7 and 8 taken from Hanst and Henson[27] show the sulfur dioxide spectrum from 7.2 to 7.6 microns and ozone spectrum from 9.2 to 10.2 microns, respectively. Figure 9, taken from Long,[26] shows the CO line at 4.609 microns. The infrared spectra shown in the Long and Hanst articles do not interfere with the strong absorption spectra of water and CO_2.

In order to obtain a value for the partial pressure of a pollutant, the absorption coefficient must be known. At constant temperature and at pressures above one-tenth atmosphere, the absorption coefficient, $k(\lambda)$, will depend on pressure P, as

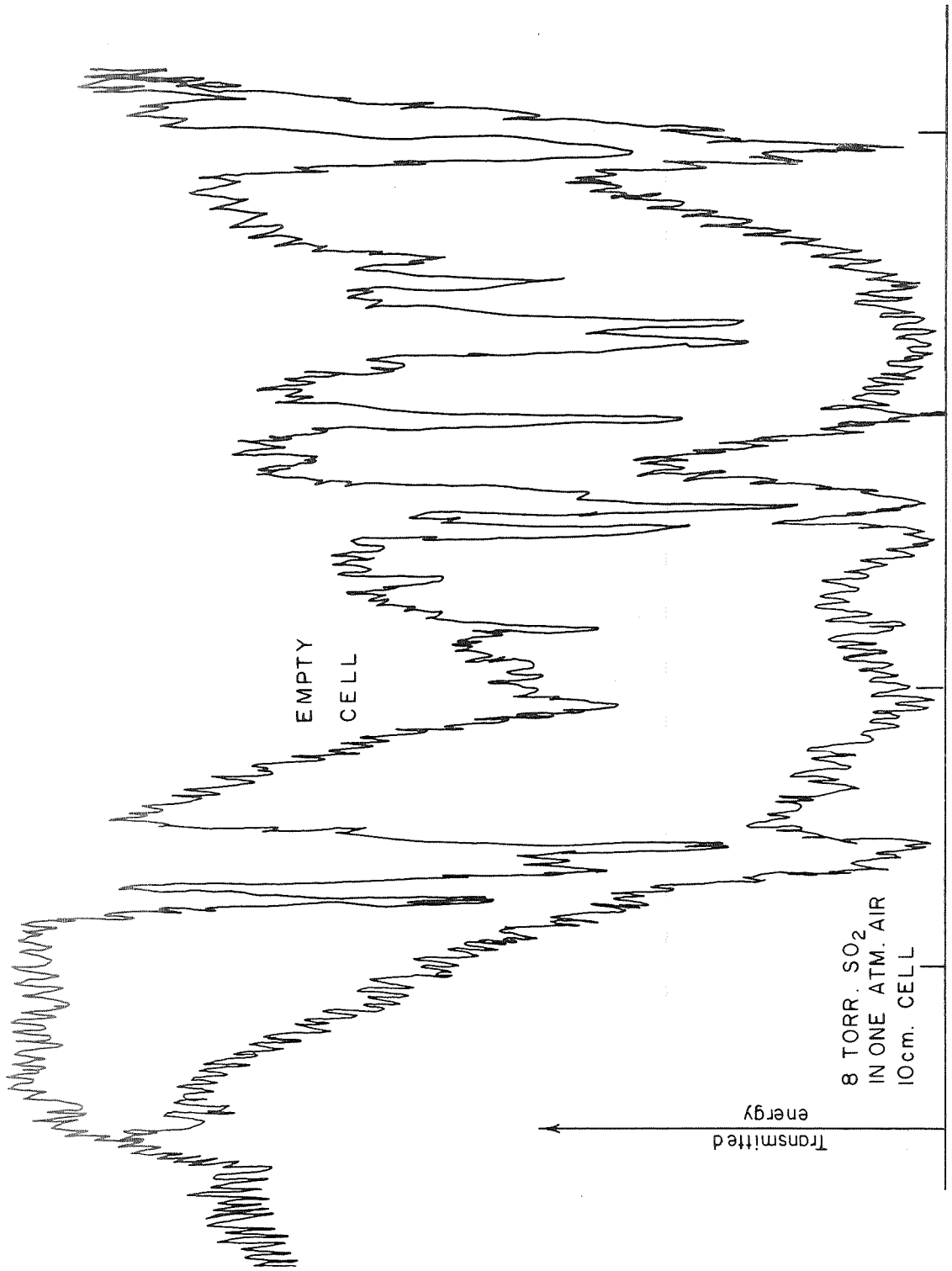

Figure 7. Absorption of SO_2 from 7.2 to 7.6 microns.

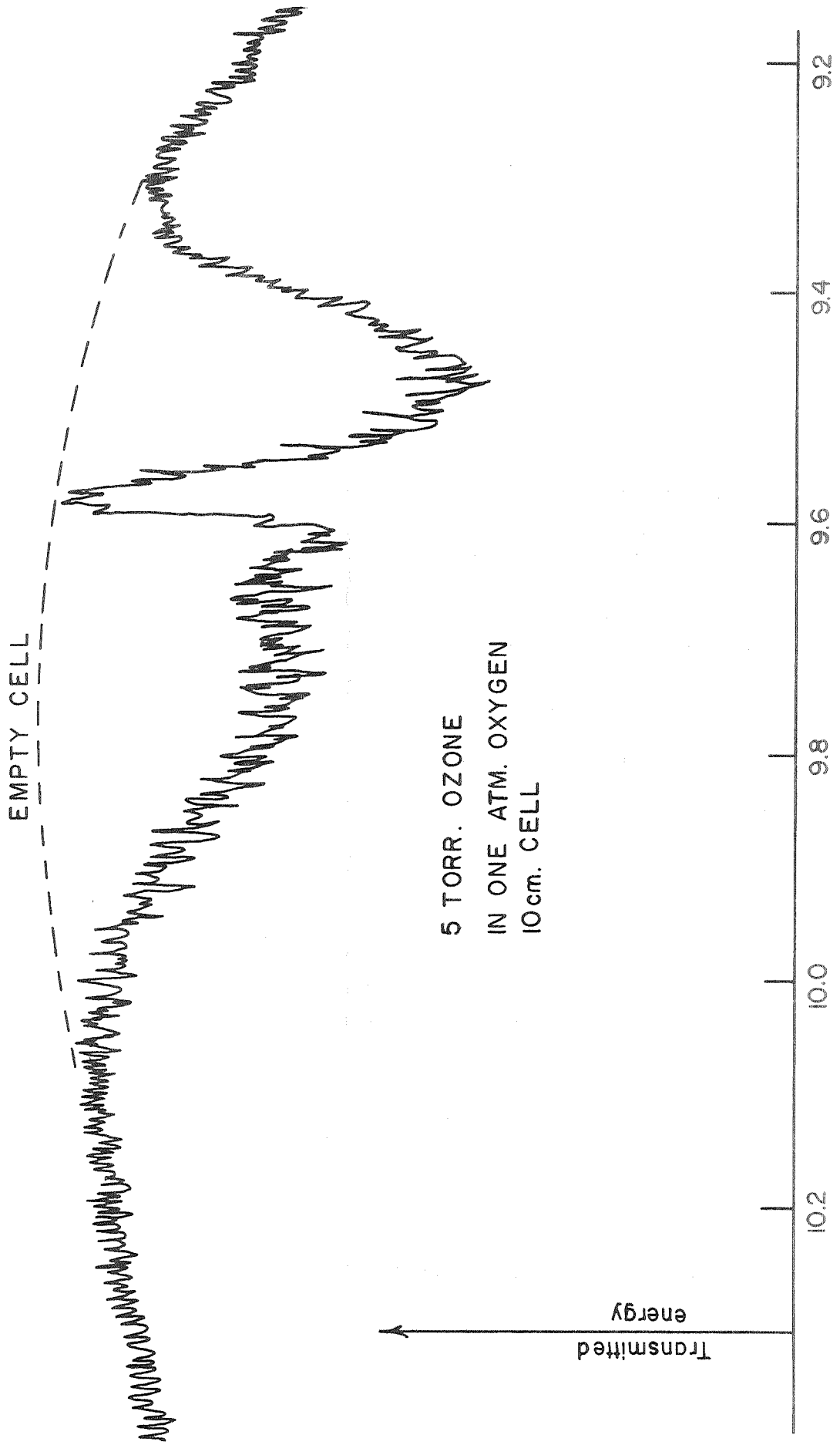

Figure 8. Absorption of ozone from 9.2 to 10.2 microns.

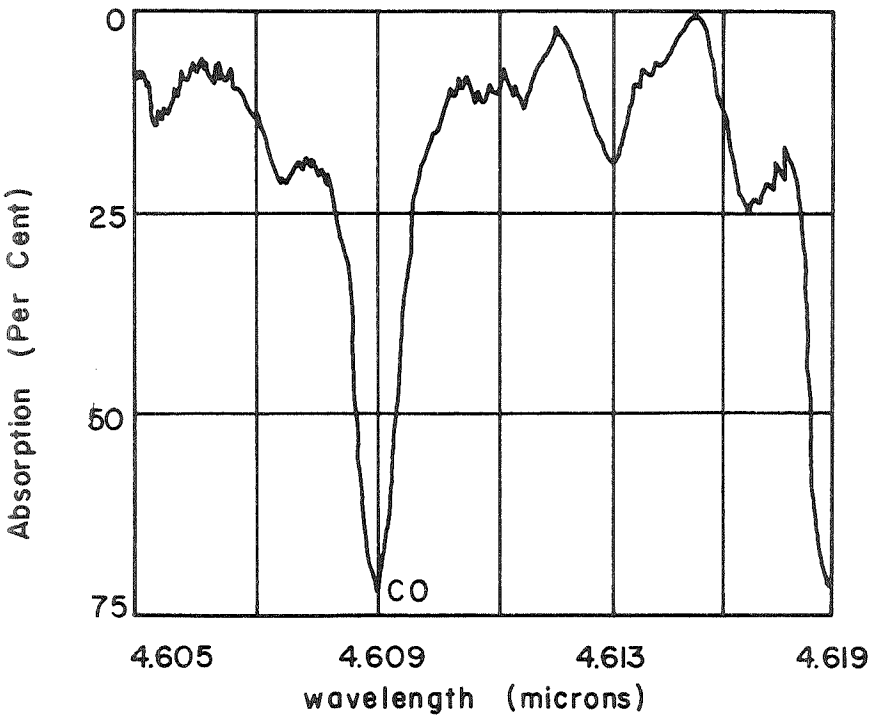

Figure 9. Atmospheric absorption near the 4.609 micron CO line.

$$k(\lambda) = \frac{(\lambda\lambda_0)^2 C_1 P}{(\lambda_0-\lambda)^2+(\lambda\lambda_0 P)^2 C_2} \qquad (6)$$

where λ_0 is the wavelength at the center of the absorption line, λ is the operating wavelength, and C_1 and C_2 are constants characteristic of the absorbing gas. $k(\lambda)$ will be directly proportional to pressure far from line center. At the center of the line ($\lambda=\lambda_0$), $k(\lambda)$ will be inversely proportional to pressure. This effect must also be taken into account in any measurement scheme hoping to take advantage of the absorption properties of pollutant gases.

Pollutant gas concentration measurements utilizing absorption may also be made through fluorescent scattering. Fluorescent scattering can occur only when the wavelength of incident radiation is in an absorption line or band of the scattering medium. Transition to a higher state of higher energy may then occur, followed by relaxation and emission of light at wavelengths equal to, greater than, or less than the incident wavelength. The longer wavelength energy, called Stokes fluorescence, is stronger by a factor of 10^3.

Both the direct absorption and fluorescence techniques require wavelength controlled sources. Unless one is extremely lucky, the source must be tunable. One scattering phenomenon which occurs regardless of the incident wavelength (within limits) is Raman scattering. The radiation wavelength does not have to be matched with absorption lines to allow transitions of the molecule. The source need not, thus, be tunable. The longer wavelength lines are of higher intensity and the wavelength displacement is related to the rotation-vibration spectrum of a molecule. The listing of Raman lines may be found in Herzberg.[28]

Note that unique determination of constituents is allowed by Raman scattering, for each molecule causes a unique wavelength displacement spectra.

Having noted the phenomena available for discriminatory pollutant gas observation, some of the section 1 sensing methods can immediately be eliminated. Several still appear as candidates:

1. Passive satellite infrared probing
2. Infrared line-of-sight
3. Laser radar.

Passive satellite infrared probing has, in essence, already been scrutinized in an earlier part of this section dealing with radiance measurements. Reference to Figure 6 shows the per cent radiance changes we can expect for low resolution satellite measurements. As Ludwig et al. indicate, passive satellite techniques can best be used for total pollutant load measurements. Of course, this is useful, for data on horizontal distributions on a world basis is necessary. The difficulties that Ludwig et al. have indicated in obtaining even these data are, however, cause enough to consider other techniques. As alluded to earlier, the problems inherent in obtaining unique pollutant data by low resolution measurements are indeed fierce.

In attempting to use high resolution absorption spectroscopy, a major restriction has been the limited amount of energy available from sources of radiation. For infrared line-of-sight absorption analysis of trace constituents of gas mixtures, a long path is usually required. The radiation from light sources being naturally divergent, the receiver signal after long paths causes weak signals. If data on very localized samples are desired, a White cell may be used, which folds the beam over a long path without losing energy through beam divergence. However,

even if such cells are used, the detection sensitivity is energy limited. With the development of the laser, not only are energy limitations no longer a problem, but long path real atmosphere line-of-sight absorption analysis has also become feasible. The laser energy is confined to a very narrow range of wavelengths. Thus the high resolution needed for absorption analysis of spectra such as are shown in Figures 7, 8, and 9 is easily available with the laser as a source; in fact, the laser energy is generally so narrow in spectra that ill-knowledge of the exact location of the laser spectra with respect to the pollutant spectra can cause large errors in pollutant concentration values. Further, it should be obvious that one may not be able to find lasers which emit at wavelengths coincident with large pollutant absorption coefficients. Hanst[29] has considered this problem for a number of pollutants, resulting in the data appearing in Table 1.

Table 1. Pollutant Absorption for Laser Lines.

Pollutant	Laser Line (microns)	Concentration in ppm for 5 per cent signal change over 1 km path
C_2H_2	Ne - 13.76	0.03
C_2H_4	CO_2 - 10.53	0.10
C_4H_{10}	I_2 - 3.43	0.05
PAN	He Ne - ?	0.10
NO	I_2 - 5.5	1.0
CO	I_2 - 4.86	2.0
O_3	CO_2 - 9.5	0.15
SO_2	CO_2 - 9.1	1.0
NH_3	CO_2 - 10.6	0.10

Perusal of Table I indicates that the carbon dioxide and iodine lasers will be most useful for pollutant detection. With both lasers having numerous possible wavelength outputs, the appropriate one is selected by utilization of an absorbing-gas cell which enhances the relative gain of the desired output wavelength with respect to other wavelengths. Long paths are needed to obtain significant signal changes. This need not, however, restrict one to horizontal ground-based measurements. The major criticism of infrared line-of-sight measurements is the inability to discriminate pollutant concentration along the path. That is, total path absorption is measured with no capability for a profile of concentration along the path. By using tunable or multiwavelength laser radar this problem can be overcome.

The laser wavelength normally used in laser radar does not fall on any atmospheric or pollutant absorption lines. Figure 10, taken from Long,[26] shows the solar spectrum near the ruby laser wavelength. A first means of tuning a laser radar is indicated by the lower scales in Figure 10. These show the relationship of wavelength output versus temperature of the ruby rod. By utilizing a ruby laser in a temperature controlled water bath as the laser radar source, emission at and around the 6943.8 Å atmospheric water vapor line can be achieved. Whether laser radar emission can be made narrow enough to scan absorption lines is still uncertain. For example, the water vapor line at 6943.8 Å has a width of 0.1 Å at half-intensity. Thus a laser line of approximately 0.01 Å width is necessary. Tiffany,[30] using a solid sapphire etalon for laser mode control, has achieved a half-width of < 0.015 Å. However, field experiments do not allow for the ideal conditions Tiffany experienced in the laboratory.

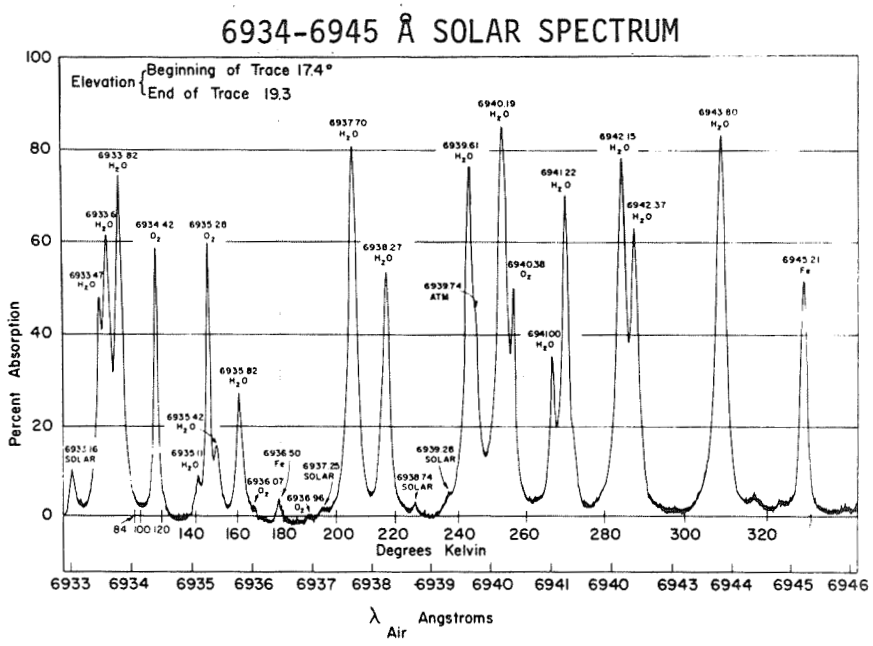

Figure 10. Solar spectrum near the 0.6943 micron ruby laser line.

If laser radar is to be effectively used in gaseous pollutant measurements, lasers with high pulsed power at pollutant gas absorption lines (i.e., 2 to 25 micron range) must be used. Some mention has been made of stimulated Raman emission to shift the source wavelength to the near infrared. In shifting the 6943 Å ruby laser emission, one generally finds too low energy conversion to the infrared wavelength, too broad a laser emission spectrum, and not enough control over the wavelength output. By making use of the fast developing dye laser, these difficulties may be overcome.

First reported in 1963[31] and best described by P. Sorokin,[32] efficient conversion ($\geq$ 5 per cent) with little pulse distortion and accurate tuning capabilities presently exist. By mounting a dye laser system on a laser radar, a system can easily be designed to give equal power levels at the normal ruby and tunable dye wavelengths. Locating the dye laser output at a water vapor or pollutant gas absorption line and the normal ruby λ being in the clear of absorption, humidity, temperature, and pollutant gas profiles may be obtained through the difference in signal return for each of these wavelengths. A major difficulty is the fact that no dyes have yet been made to lase past 1.5 microns. Until efficiently lasing dyes are found in the infrared (past 2 microns), another laser radar technique must be used for gas pollutant detection.

The most successful technique for atmospheric constituent and pollutant gas observation by laser radar is through measurement of the Raman component of backscatter. Two recent papers[33,34] have shown that field data can be obtained. Cooney[33] has observed the first Stokes (longer wavelength) Raman backscatter off the vibrational levels of atmospheric N_2 and H_2O to > 2 km heights. Noting that the Raman

backscatter cross section has a $1/\lambda^4$ dependence, ruby laser emission was first frequency doubled, so that signal emission occurred at 3472 Å and backscatter return in the case of water vapor occurs at 3976 Å. An added benefit is that the spectral response of the detector peaks near this wavelength. A profile on absolute humidity obtained by Cooney is shown in Figure 11.

Kobayasi and Inaba[34] have detected the Raman component of sulfur dioxide and carbon dioxide backscatter using laser radar. They did so using the 6943 Å ruby emission as source and observing SO_2 signal return at 7545 Å and CO_2 return at 7683 Å. This experiment demonstrates that laser radar can be used not only to uniquely identify gaseous pollutants but also to measure their spatial distribution on a real-time basis. With further improvements in lasers and use of mobile platforms (including satellites), the laser radar technique appears to be the best candidate for reliable, quantitative, spatial distribution, and real-time gaseous pollutant remote sensing.

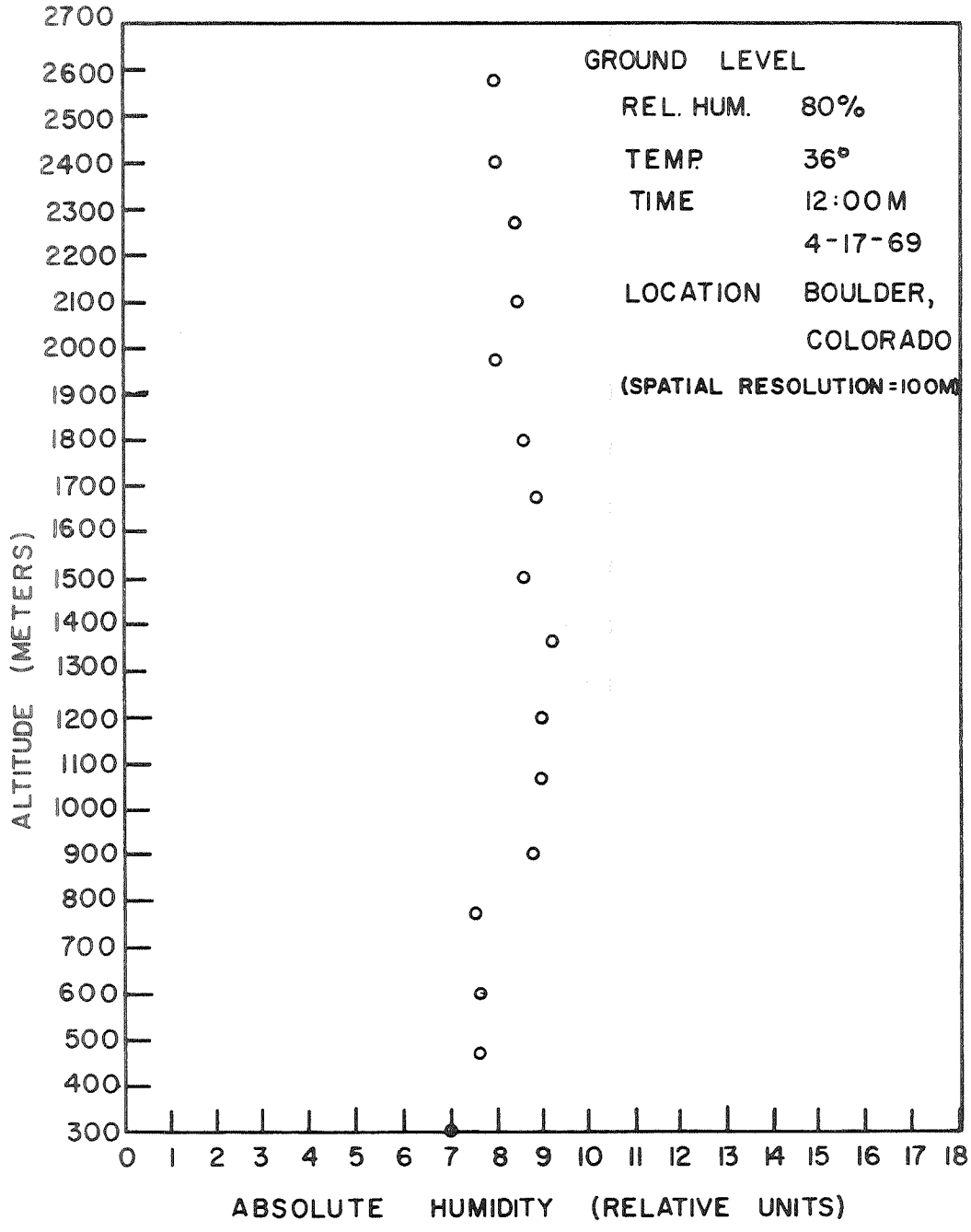

Figure 11. Vertical profile of absolute humidity at Boulder, Colorado, on 17 April 1969.

2. THE LASER RADAR TECHNIQUE

Don't ask me nothin about nothin
I just might tell you the truth
--Bob Dylan

Although Chapter 1 has "proven" the laser radar technique to be the most promising of the available remote sensing schemes for air pollution and salient atmospheric measurements, a thorough description of the technique is in order so that its shortcomings can be perceived, pondered upon, and, hopefully, corrected or compensated for.

Figure 12 depicts the information handling components of a laser radar system. A Q-switched ruby or neodymium laser, respectively, of 6943 Å and 10600 Å wavelength is the source. The normal mode of operation is vertical with a pulse duration of 20 nanoseconds giving a height resolution of 3 m. For measurements less than 5 km in range, a pulse energy of 1 joule is sufficient. The backscattered energy is collected at a telescope, passed through collimating optics, an optical filter centered at the laser wavelength with a 10 Å passband (allowing for daytime observation); and detected by a 10- to 16-stage photomultiplier with an S-20 red-sensitive surface. The photomultiplier signal is inserted at the vertical input of an oscilloscope. The horizontal input of the scope is triggered at laser firing. Thus, the received signal signature has its range (i.e., vertical height) scaled to the oscilloscope screen. The deflection at any one point on the oscilloscope display can be related to an instantaneous scattering volume at known range. At this stage, one major "hang-up" in the use of laser radar may be observed.

Present Q-switched lasers, water-cooled or not, do not have a high enough pulse repetition rate to allow for persistence at the oscilloscope

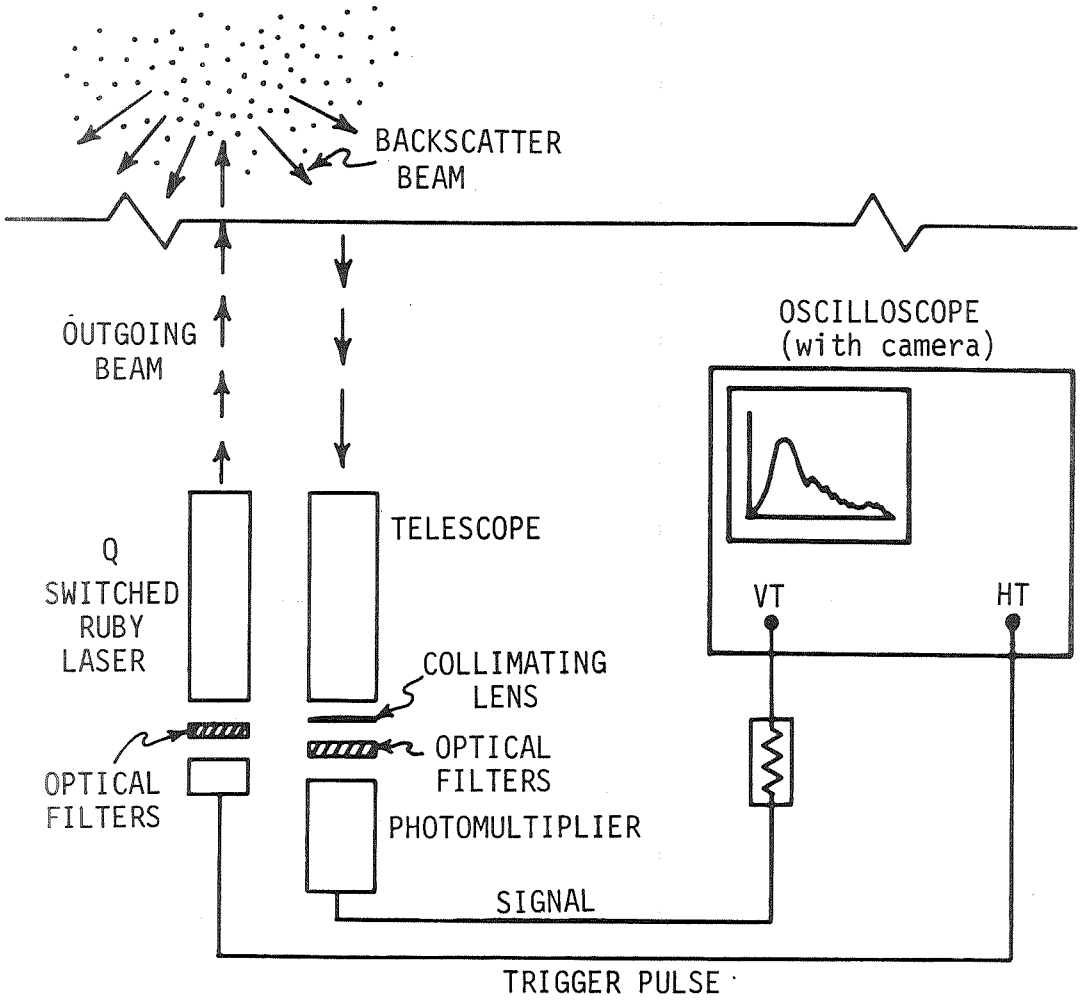

Figure 12. Basic components of the laser radar system.

screen or for a digitized output. Data analysis is a cumbersome process of visual measurement of a signal signature photo. As improvement in laser technology allows high repetition rates, this problem will solve itself.

The scattering volume observed at any instant of time is determined by the pulse duration of the laser and beam divergence of the output beam (laser plus source collimating optics). Nominally, a one milliradian beam divergence resulting in a one-meter diameter scattering volume at one kilometer height is used. As noted earlier, a typical pulse duration might be 40 nanoseconds, giving a volume length of six meters. Thus, the instantaneous scattering volume is on the order of five to ten cubic meters.

The radar equation for meteorological echoes presently forms the theoretical foundation for laser radar echo analysis. The radar equation widely used at present may be written as

$$P_r = P_t \frac{A_r T_a \tau c}{8\pi R^2} \beta \qquad (7)$$

where

P_r = received power (watts)

P_t = power transmitted by laser (watts)

A_r = receiver collecting area (m^2)

T_a = atmospheric transmission factor, Lidar to scattering volume and return (dimensionless)

τ = pulse duration (seconds)

c = (velocity of light ($m\ sec^{-1}$)

R = range, Lidar to scattering volume (m)

β = backscattering function at the laser wavelength ($m^{-1}\ ster^{-1}$).

T_a, of course, depends on β. If we consider operation over a few kilometers only, T_a may be set equal to one. Otherwise, (7) results in an integral equation in β. With this assumption in mind, one can easily arrive at the result:

$$\beta = (\text{system constant})\ R^2 X \tag{8}$$

where

R = range as before

X = vertical deflection at the oscilloscope (m).

Once β has been experimentally determined, several atmospheric parameters can easily be obtained. Barrett[17] has shown that the turbidity (T), visibility (V), and particulate load density (Q) are linear functions of β:

$$T = 0.764 + 0.041\beta \tag{9a}$$

$$V = 1212/(\beta - 1.98) \tag{9b}$$

$$Q = 4.96(\beta - 5.8). \tag{9c}$$

(9a), (9b), and (9c) are based on the assumed wavelength, $\lambda = 0.6943\mu$, the refractive index, n = 1.5, and the Junge size distribution

$$N = c \int_{r_1}^{r_2} r^{-m}\, d(\ell n\ r) \tag{10}$$

with $r_1 = 0.04\mu$, $r_2 = 10\mu$, and m = 3.

Typical signal signatures are shown in Figures 13, 14 (Barrett[17]), and 15 (Johnson[18]). Figure 13 is an oscilloscope trace when a shelf of pollutants was present at the 400-foot region. As was pointed out earlier, the theoretical curves of Figure 5 can be assumed to fit the real atmosphere so that "background clear air scatter" can be subtracted from the total observed scatter to give pollutant particulate concentrations.

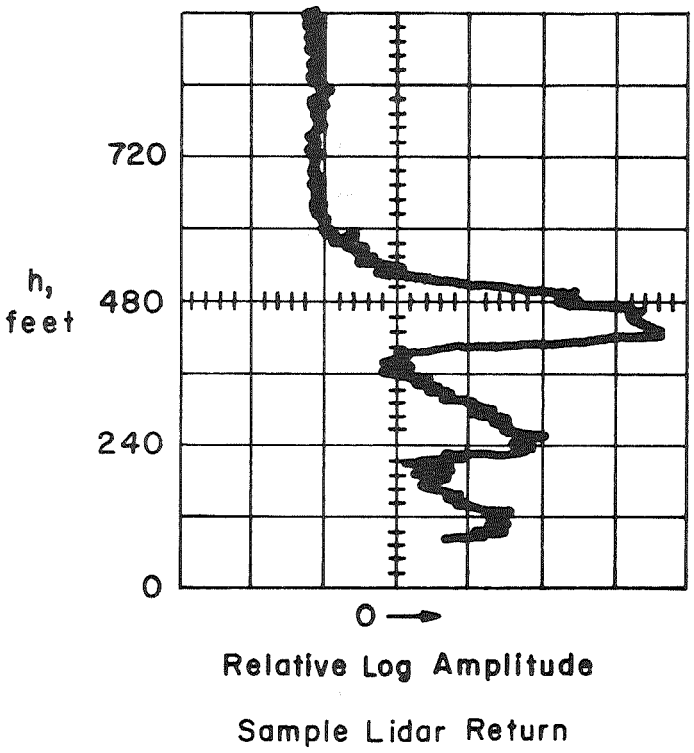

Figure 13. Relative log amplitude sample laser radar return.

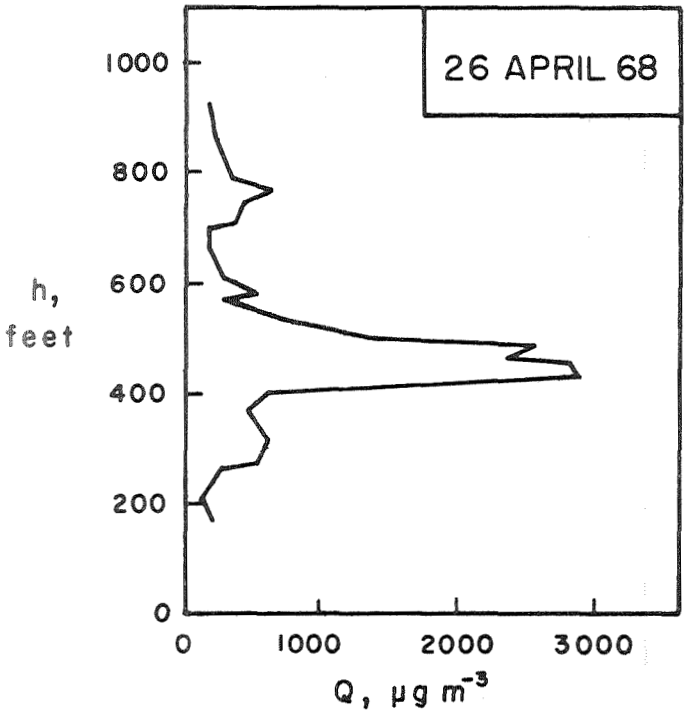

Plot of particulate loading vs. height

Figure 14. Plot of particulate loading vs. height.

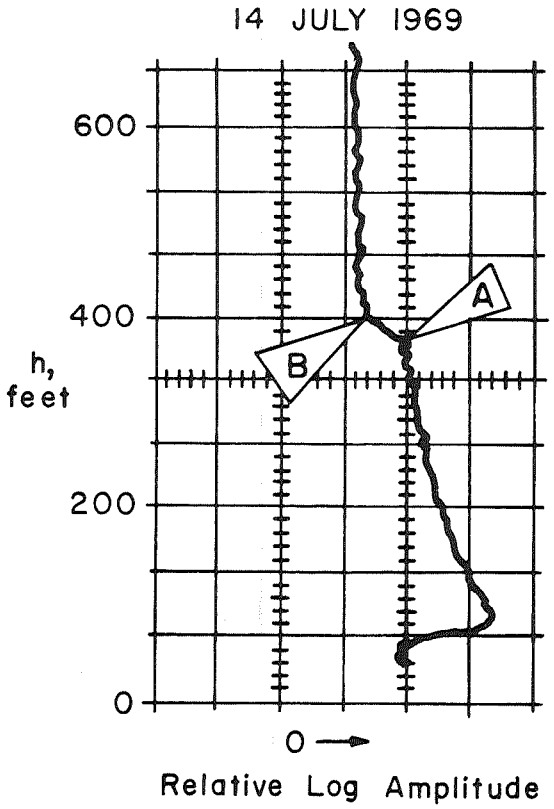

Figure 15. Sample laser radar return showing transition from relatively polluted air below the inversion base to cleaner air above.

However, this assumption has not proved entirely satisfactory to most laser radar researchers. More often, a background is approximated by averaging data taken at times when the atmosphere is suspected to be "most clean." Although crude, it is the most-used technique. Barrett has used this method to obtain the corrected plot of particulate loading (Figure 14) and real atmosphere data (Figure 13).

It has been suggested that the temperature inversion height can be monitored by observation of pollutant particulates. As described in the preface, temperature inversions allow much less mixing through the inversion, and, thus, particulate loading should fall sharply at the inversion. Figure 15 shows such a sharp drop in signal return near 400 feet. Although this most likely is the inversion height, laser radar returns rarely show only one such clear demarcation, as in Figure 15. As already indicated in the preface, the importance of temperature inversion and low-level temperature profile measurements can not be underestimated. It behooves us to explore more sophisticated techniques than the above to obtain these measurements. A literature search uncovered no techniques suitable to laser radar to obtain such profiles.

Section 1.3.2 described the utilization of pollutant gas and water vapor absorption lines to determine their vertical profiles. The difference in scattered signal from a laser radar tuned to and away from these absorption lines can be related to temperature lapse rates.

The temperature versus height profile can, in theory, be constructed from the lapse rate measurements and a single temperature measurement along the path. Absorption line shapes in the lower atmosphere are Lorentz collision broadened.[35] This is true in the infrared and red spectral regions of the lower atmosphere ($\leq$ 20 km) since the pressure is sufficiently high. For collision-broadened lines, the half-width at

half-intensity (α) is given by:

$$\alpha = \alpha_o \frac{p}{p_o}\sqrt{\frac{T_o}{T}} \tag{11}$$

where

α_o = half-width at half-intensity at initial conditions of pressure and temperature

p_o = initial pressure

T_o = initial temperature.

The hydrostatic equation and the equation of state with the assumption of a constant temperature lapse rate, Γ, can be used to rewrite (11) as

$$\alpha(x) = \alpha_o \left(\frac{T_o - \Gamma z}{T_o} \right)^{(g/\Gamma R - 1/2)} . \tag{12}$$

The lapse rate can be deduced from (12) since all the remaining terms are either observed or known constants. Once the lapse rate is found, and given an initial temperature at $z = 0$, the temperature height profile can easily be plotted. However, as pointed out in section 1.3.2, substantial line-width narrowing must be achieved before absorption line scanning can be made practical for laser radar.

A rather intriguing and yet simple (at least, in theory) way of obtaining temperature profiles would accrue through unique determination of the distribution of molecular atmospheric constituents. Rayleigh scattering, caused by the molecular constituents, is directly proportional to the density of scatterers:[14]

$$I = \rho \frac{9\pi^2 V^2}{2R^2 \lambda^4} \left(\frac{m^2-1}{m^2+2} \right)^2 (1+\cos^2\theta) \tag{13}$$

where

I = scattered intensity (watts m^{-2})

ρ = density of scattering medium (m^{-3})

V = volume of scattering medium (m^3)

λ = wavelength of incident light (A)

R = range (m)

m = mean refractive index of particles (dimensionless)

θ = scattering angle measured from the forward direction (°).

Now the density scale height is given by:

$$H = RT/Mg \tag{14}$$

where

H = scale height (m)

R = gas constant (joule kgm^{-1} $mole^{-1}$ $°K^{-1}$)

T = absolute temperature (°K)

M = mean molecular mass (kgm)

g = acceleration due to gravity (m sec^{-2}).

Since the scale height is defined by

$$H = -\rho / \Delta\rho/\Delta h, \tag{15}$$

the temperature at any height can then be written as

$$T_h = - \frac{Mg\rho}{R} \left(\frac{\Delta h}{\Delta \rho} \right). \tag{16}$$

Now ρ and $\Delta\rho/\Delta h$ can easily be read off a Rayleigh signal signature return. Thus, if the laser radar scheme can be operated so as to monitor backscatter return from the molecular constituents alone, temperature profile measurements can be achieved.

Section 1.3.1 also concluded with the importance of a discriminatory process so that a "true" background signal return could be determined. There, dependent scattering was alluded to as a possible mechanism for discrimination. Because dependent scattering (arising from the coherence properties of the illuminating source) gives rise to a signal return proportional to the square of the number of scattering particles and because the ratio of the density of atmospheric molecular constituents to the density of aerosols and pollutant particulates is on the order of 10^{15}, dependent scattering return is essentially due only to the molecular atmospheric constituents.

Analysis of dependent scattering is important for another reason. Up to the present, laser radar investigations have assumed the radar equation for meteorological echoes to apply to laser radar atmospheric applications. However, with progress in source line-width narrowing to achieve the capability for absorption line scanning, a concomitant increase in the per cent of dependent scattering may result. This is true because the coherence length of any source is inversely related to the source line width. It appears then that a thorough analysis of source coherence effects upon the scattering process is in order. This is doubly true now that laser radar is recognized as the most promising "all purpose" air pollution monitoring scheme.

3. DEPENDENT SCATTERING EFFECTS

The whole thing is a low put-up job on our noble credulity.
--Norman Lindsay

The fast-growing interest in statistical properties of optical fields brings new attention to the problems of light scattering by media with random parameters. As described by Twersky,[36] the approach usually depends on the range of parameters describing the medium and radiation. If the medium consists of particles of diameter a, with the average distance between them ℓ, then for $a << \ell << \lambda$, the medium may be regarded as continuous with the average dielectric constant ε. Scattering depends on the fluctuations in ε. Tatarski[37] has clarified this problem.

On the other hand, comparatively little attention has been paid to the study of statistical properties of radiation scattered by media with $\ell >> a$, $\ell >> \lambda$ (many particle systems). In this case (in the absence of long-range potential interaction between particles), scattering by each particle is usually regarded as independent[38]--implying no phase-angle relationships among individual rays in the backscattered signal. Equation (7) of Chapter 2 makes this implicit assumption. β in (7) is assumed to be linearly related to the number of scatterers. Thus, (7) can, for convenience, be written as

$$P_r = c\delta N \tag{17}$$

where c is a coefficient as a function of the range, R, and other laser radar parameters, δ is the backscattering volume cross section in $m^{-1}ster^{-1}$, and N is the number of scattering particles.

The concluding portion of Chapter 2 seriously questioned whether this assumption of independent scattering can be made in laser radar. The purpose

of the present Chapter is the analysis of laser radar scattering for the effect of dependent scattering. In determining an equation corresponding to (17)--but including dependent scattering effects--the first question to be answered is whether or not conventional radar coherence analysis is applicable. That is, must quantum effects be considered?

3.1 Quantum Effects in Laser Radar

Note that certain inconsistencies in classical field theory become evident at very high optical frequencies. It is impossible merely to translate usual ideas from microwave theory to optical wavelengths without considering the effects that appear at very short wavelengths. The source of the problems arises out of the discrete nature of the photon. At microwave frequencies, the lower limit of detectable power corresponds to a very large photon rate because the energy of each photon is small. Thus, if a signal is to be detected above this noise level, the photon rate of the signal must be even larger.

At optical wavelengths, the energy of each photon is considerably greater, and it is possible to observe the effect of a single photon. As at microwave wavelengths, the alternating component of the field is proportional to the square root of the photon rate; thus, detectable fields at a low photon rate will have a large alternating component when compared with the field strength. In addition, at a low photon rate large phase fluctuations appear. Therefore, at optical wavelengths, usual coherent radar techniques may not be applicable. The implications of these discrete or quantum effects on the performance of laser radar must be considered.

The energy received per pulse can be evaluated in terms of conventional geometrical optics. The power density at a target can be defined

by considering the configuration shown in Figure 16. For simplicity, consider a diffuse target covering the entire beam (i.e., neglect target

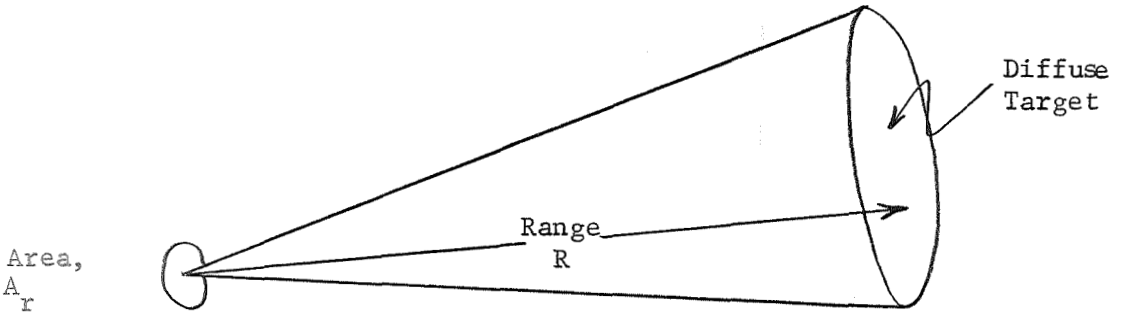

Figure 16. Received power and the fluctuation therein.

effects), a monostatic system, and no transmission loss along the path. The received power, under these conditions, will be

$$P_r = \frac{P_t A_r}{4\pi R^2} \tag{18}$$

where R is the range and A_r is the area of the receiver. The energy received by the system per pulse is

$$E = \frac{P_r \tau}{\left(\frac{4\pi A_r}{\lambda^2}\right)} \tag{19}$$

where τ is the pulse length.

Recognizing that the Poisson law of small probabilities describes the probability of observing exactly n photons passing through the aperture A_r in time t, one can write

$$P(n) = \frac{(\rho A_r t)^n}{n!} e^{-\rho A_r t} \tag{20}$$

where ρ is the average number of photons passing through an aperture of area A_r in a time of t seconds.

A fair determination of the amplitude of the fluctuating component of the field can be determined from the statistical parameters of n. Let the fluctuation in n be defined by

$$(\Delta n)^2 = \overline{n^2} - \bar{n}^2 \tag{21}$$

where $\bar{n}$ is the first moment of n and $\overline{n^2}$ is the second moment. The mean value of n is

$$\bar{n} = \sum_{n=0}^{\infty} \frac{n(\rho A_r t)^n e^{-\rho A_r t}}{n!} = \rho A_r t \tag{22}$$

and

$$\overline{n^2} = \sum_{n=0}^{\infty} \frac{n^2(\rho A_r t)^n e^{-\rho A_r t}}{n!} = \rho A_r t + (\rho A_r t)^2. \tag{23}$$

Thus,

$$(\Delta n)^2 = \rho A_r t \quad \text{or} \quad \Delta n = \sqrt{\rho A_r t}. \tag{24}$$

Note that Δn has the units of photons even though its algebraic definition appears to give a different meaning.

The net energy passing through the receiving aperture A_r in time t is

$$E = h\nu\rho A_r t \tag{25}$$

and the fluctuating component is

$$\Delta E = h\nu\sqrt{\rho A_r t} \tag{26}$$

which is the uncertainty in received energy. Additionally, the ability to measure the phase of the detected field must be considered. This problem can be reduced to that of detecting the amplitudes of the in-phase and quadrature components of the field when compared with a standard frequency. It can then be easily shown that the uncertainty in phase becomes

$$\Delta\phi \geq \frac{1}{2}\frac{h\nu}{E} \quad , \qquad \text{or using (25),}$$

$$\Delta\phi \geq \frac{1}{2\rho A_r t} \, . \tag{27}$$

Now the importance of the magnitude of ΔE as given by (26) can only be viewed when compared with the energy level being considered. Thus, the ratio of energy received to the uncertainty in energy (the signal-to-noise ratio) is the parameter of interest.

$$E/\Delta E = \sqrt{\rho A_r t} = \sqrt{n}. \tag{28}$$

Since the product of the received power and pulse length is the energy received per pulse, and the number of photons received per pulse is the ratio of this energy to $h\nu$, the signal-to-noise ratio, in terms of system parameters, can be expressed as

$$S/N \approx E/\Delta E = \frac{1}{2R}\sqrt{\frac{P_t A_r}{\pi h\nu}}\,\tau \tag{29}$$

and

$$\Delta\phi \geq \frac{1}{2}\left(\frac{\Delta E}{E}\right)^2 \quad \text{or}$$

$$\Delta\phi \geq 2R^2\,\frac{\pi h\nu}{P_t A_r \tau} \, . \tag{30}$$

For a typical laser radar with

$$P_t = 10^8 \text{ watts}$$

$$A_r = .01 \text{ m}^2$$

$$\tau = 3\text{x}10^{-8} \text{ seconds}$$

$$h\nu = 6.625\text{x}10^{-20} \text{ j}$$

$$S/N \tilde{\geq} 1.32\text{x}10^{13}/R \quad \text{and} \quad \Delta\phi \geq 1.39\text{x}10^{-25} R^2. \tag{31}$$

The important conclusion is that, in laser radar, for lower atmospheric ($\leq$ 10km) work the S/N $\tilde{\geq}$ 10^9 (i.e., the energy received is 10^9 larger than the fluctuation in energy due to the discrete nature of light); the wave nature of light dominates. Thus, classical coherence theory applies to the problem at hand.

Although classical coherence theory can be applied to the laser radar problem, this does not necessarily mean that conventional radar coherence analysis holds. Because radar coherence theory is often specific to system parameters in microwave radar and because system parameters are widely varying in optical vs. microwave radar, coherence properties may have entirely different implications for laser radar.

3.2 Spatial Detection Effects

The analysis of this section has matured due to a number of helpful suggestions by J. W. Goodman[40] and G. Biernson and R. F. Lucy.[41,42]

Assume a dependent scattering process. For laser radar this means complete coherence in the backscattered light from the scattering volume. (This assumption will be scrutinized in section 3.3.) Under the conditions of this assumption, the scattered field at plane s, immediately in front

of the scattering volume (see Figure 17) is

$$E_s(x,y;t) = E(x,y)\ \exp[-i2\pi\nu_s t]. \tag{32}$$

Note that polarization effects will be neglected but ν_s may differ from the incident frequency. ν_s is the scattered radiation frequency as measured at the system receiver.

The field at the detector plane is

$$E_r(u,v;t) = E(u,v)\ \exp[-i2\pi\nu_s t]. \tag{33}$$

The spatial energy density, $\rho(u,v)$ (i.e., the energy per unit area incident at (u,v) during the reception of the pulse), is

$$\rho(u,v) = \frac{\tau}{2z_o}\ |E(u,v)|^2 \tag{34}$$

where τ is the pulse length and z_o is the characteristic impedance of the medium in which the fields propagate.

First-order statistics cannot determine the "coarseness" of the pattern of energy density at the detector plane. Sufficient information can, however, be made available if the spatial coherence functions of the received field components are known.

The two-dimensional normalized spatial coherence function is given by

$$\gamma(u_1,v_1;u_2,v_2) = \frac{\langle E(u_1,v_1)E^*(u_2,v_2)\rangle}{2\delta^2} \tag{35}$$

where $\langle\ \rangle$ represents ensemble averaging and δ is the variance of E(u,v).

γ can be described[43] in terms of the ensemble averaged scattered power density P(x,y) as

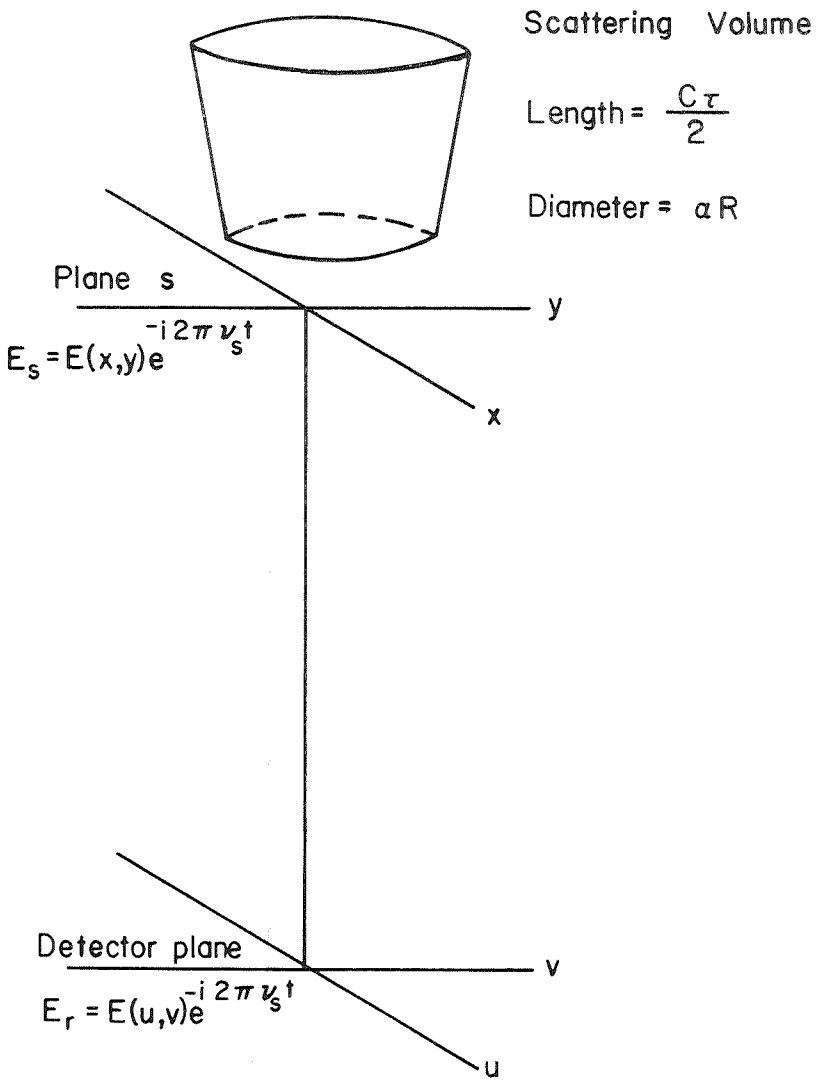

Figure 17. Configuration for spatial detection effects.

$$\gamma(u_1,v_1;u_2,v_2) = \exp\left[\frac{ik}{2r}(u_1^2+v_1^2-u_2^2-v_2^2)\right]$$

$$\times \frac{\iint_{-\infty}^{\infty} P(x,y)\exp\left[-\frac{ik}{r}(x\Delta u+y\Delta v)\right]\,dxdy}{\iint_{-\infty}^{\infty} P(x,y)\,dxdy} \qquad (36)$$

where $P(x,y) = \frac{\langle|E(x,y)|^2\rangle}{2z_o}$,

$$\Delta u = u_1 - u_2,$$

$$\Delta v = v_1 - v_2.$$

and proper consideration of phase properties due to varying range has been taken into consideration. This result for γ is in agreement with the van Cittert-Zernike theorem.

The total energy ε incident on the receiving aperture of area A at the detector plane is

$$\varepsilon = \iint_A \rho(u,v)\,dudv. \qquad (37)$$

The total energy is thus a random variable over an ensemble of scattering centers.

The properties of the signal photoelectrons emitted during reception of a return are influenced by the statistical properties of ε. Let the receiving aperture be regarded as consisting of K independent spatial coherence cells--the energy density being approximately constant within any one coherence cell and statistically independent of the energy density in other coherence cells. Mandel[44] has shown the total energy for such

a problem is approximately a gamma variate, obeying the probability-density function

$$p(\varepsilon) = \begin{cases} c^K \varepsilon^{K-1} \exp[-c\,\varepsilon] & \varepsilon \geq 0 \\ 0 & \varepsilon < 0 \end{cases} \tag{38}$$

where c and K are to be determined.

By direct analogy to Rice's work[45] on time fluctuations,

$$\frac{K}{c} = \bar{\varepsilon} \qquad \text{and} \qquad \frac{K}{c^2} = \overline{\varepsilon^2} - (\bar{\varepsilon})^2 \tag{39}$$

Crane[46] points out that the autocorrelation function a_e of the energy density incident on the receiving aperture defined by

$$a_e(u_1,v_1;u_2,v_2) = \langle e(u_1,v_1)e(u_2,v_2)\rangle \tag{40}$$

can be related to γ by

$$a_e(u_1,v_1;u_2,v_2) = \frac{\bar{\varepsilon}^2}{A_r^2}\left(1+|\gamma(u_1,v_1;u_2,v_2)|^2\right). \tag{41}$$

Crane[46] further points out that

$$\overline{\varepsilon^2} = \iint_{A_r} du_1 dv_1 \iint_{A_r} du_2 dv_2 a_e(u_1,v_1;u_2,v_2). \tag{42}$$

Combining (41) and (42) with (39) gives

$$\frac{1}{K} = \frac{\iint_{A_r} du_1 dv_1 \iint_{A_r} du_2 dv_2\, a_e(u_1,v_1;u_2,v_2)}{(\bar{\varepsilon})^2} - 1 \tag{43}$$

or

$$K = A_r^2\left[\int_{A_r}\int du_1 dv_1 \int_{A_r}\int du_2 dv_2 |\gamma(u_1,v_1;u_2,v_2)|^2 \right]^{-1} \qquad (44)$$

and $$c = K/\bar{\varepsilon}.$$

Of course, the quantity of interest is the number of observed coherence cells at the receiving aperture. To find this, Equation (44) must be put in a form more amenable to solution.

Define

$$D(u,v) = \begin{cases} 1 & (u,v) \text{ in } A_r \\ 0 & \text{otherwise} \end{cases} . \qquad (45)$$

Then

$$K = A_r^2\left[\iint_{-\infty}^{\infty} du_1 dv_1 D(u_1,v_1) \iint_{-\infty}^{\infty} du_2 dv_2 D(u_2,v_2) |\gamma(u_1,v_1;u_2,v_2)|^2 \right]^{-1} . \qquad (46)$$

Now, γ can be expressed as in (35) or, noting that $|\gamma|^2$, as expressed in (36), depends only on the coordinate differences $\Delta u = u_1 - u_2$ and $\Delta v = v_1 - v_2$ since

$$|\gamma|^2 = \left| \frac{\iint_{-\infty}^{\infty} P(x,y)\exp[-\frac{i2\pi}{2\tau}(\Delta ux+\Delta vy)]dxdy}{\iint_{-\infty}^{\infty} P(x,y)dxdy} \right|^2 . \qquad (47)$$

Thus, a change in variables allows

$$K = A_r^2\left[\iint_{-\infty}^{\infty} d(\Delta u)d(\Delta v)|\gamma(\Delta u,\Delta v)|^2 \iint_{-\infty}^{\infty} du_2 dv_2 D(u_2,v_2)D(u_2+\Delta u,v_2+\Delta v) \right]^{-1} . \qquad (48)$$

Define

$$a(\Delta u,\Delta v) = \frac{\iint_{-\infty}^{\infty} D(u_2,v_2)D(u_2+\Delta u,v_2+\Delta v)du_2dv_2}{A_r} \quad . \tag{49}$$

$a(\Delta u,\Delta v)$ is the normalized autocorrelation function of the pupil function.

For a circular receiving aperture of diameter ℓ_r,

$$K = A_r\left[\iint_{-\infty}^{\infty} a(\Delta u,\Delta v)\left|\gamma(\Delta u,\Delta v)\right|^2 d(\Delta u)d(\Delta v)\right]^{-1}$$

$$= \frac{\pi\ell_r^2}{4}\left[\int_0^{\ell_r/2}\int_0^{2\pi} a(r\cos\theta, r\sin\theta)\left|\gamma(r\cos\theta, r\sin\theta)\right|^2 r d\theta dr\right]^{-1} . \tag{50}$$

Letting $\rho = \frac{2}{\ell_r}\, dr$,

$$K = \pi\left[\int_0^1\int_0^{2\pi} \frac{\iint_{-\infty}^{\infty} D(u_2,v_2)D(u_2+\frac{\ell_r\rho}{2}\cos\theta,\ v_2+\frac{\ell_r\rho}{2}\sin\theta)\ du_2dv_2}{\pi\ell_r^2/2}\right.$$

$$\left. x\ \left|\gamma(\frac{\ell_r\rho}{2}\cos\theta,\ \frac{\ell_r\rho}{2}\sin\theta)\right|^2\rho d\theta d\rho\right]^{-1} \tag{51}$$

Goodman[47] has shown

$$\iint_{-\infty}^{\infty} D(u_2,v_2)D(u_2+\frac{\ell_r\rho}{2}\cos\theta, v_2+\frac{\ell_r\rho}{2}\sin\theta)du_2dv_2 = 2\ell_r^2[\cos^{-1}\rho-\rho(1-\rho^2)^{1/2}]. \tag{52}$$

Thus,

$$K = \frac{\pi^2}{8}\left[\int_0^1\int_0^{2\pi} \rho(\cos^{-1}\rho-\rho(1-\rho^2)^{1/2})\left|\gamma(\frac{\ell_r\rho}{2}\cos\theta,\ \frac{\ell_r\rho}{2}\sin\theta)\right|^2 d\theta d\rho\right]^{-1} \tag{53}$$

Two situations can arise: either partial or total interception of the transmitted beam. In laser radar the latter applies. Of course, the assumption is made that a finite spot size exists (i.e., the Gaussian beam pattern for laser output is cut off at, say the 1/e point).

The quantity still to be found is $|\gamma|^2$. Specifically, we are interested in the circular aperture case for which

$$|\gamma(\ell_r\rho,\theta)|^2 = \left| \frac{\int_{-\infty}^{\infty}\int P(x,y)\exp[-\frac{i2\pi}{\lambda r}(\frac{\ell_r\rho x}{2}\cos\theta+\frac{\ell_r\rho y}{2}\sin\theta)]dxdy}{\int_{-\infty}^{\infty}\int P(x,y)dxdy} \right|^2 \quad (54)$$

where

$$P(x,y) = \frac{<|E(x,y)|^2>}{2z_o} .$$

$E(x,y)$, the scattered-field distribution across the plane lying just in front of the scattering region, has random spatial properties for the type of random scattering process considered. The analysis of this problem proves too difficult to solve.[48]

Under the condition of total interception of the transmitted beam, γ may be calculated in a simpler manner. Note, the source field $E(x,y)$ is planar (although optically rough). In such a case, $P(x,y)$ (the radar brightness distribution) is linearly proportional to the intensity distribution across the beam incident at the scattering region. Thus, the normalized coherence function can be found from a Fourier transform of the incident intensity distribution. That is

$$\gamma(x,y)\alpha\mathcal{F}_T(I(x,y)) \quad (55)$$

Also, since the scattering region is in the far field of the transmitting optics, a second Fourier transform relation exists between the

complex field distribution impressed across the transmitting aperture and the complex field distribution incident at the scattering region.[49] That is,

$$\mathcal{F}_T(x,y) = \mathcal{F}(u,v) \exp[-i \frac{\pi r}{\lambda f^2} (x^2-y^2)]. \qquad (56)$$

(55) and (56) together imply the coherence function to be given by the normalized autocorrelation function of the complex field distribution E(u,v) impressed at the transmitting aperture. Thus,

$$|\gamma(\Delta u,\Delta v)| = \frac{\left| \int_{-\infty}^{\infty}\int E(\zeta,\eta)E^*(\zeta+\Delta u,\eta+\Delta v)d\zeta d\eta \right|}{\int_{-\infty}^{\infty}\int |E(\zeta,\eta)|^2 d\zeta d\eta} . \qquad (57)$$

For a circular aperture,

$$|\gamma(\ell_r\rho,\theta)| = \frac{\left| \int_{-\infty}^{\infty}\int E(\zeta,\eta)E^*(\zeta+ \frac{\ell_r\rho}{2} \cos\theta,\eta+ \frac{\ell_r\rho}{2} \sin\theta)d\zeta d\eta \right|}{\int_{-\infty}^{\infty}\int |E(\zeta,\eta)|^2 d\zeta d\eta} . \qquad (58)$$

By assuming a uniform field distribution at the transmitting aperture, a solution for K can now be obtained, for a uniformly illuminated aperture, as follows:

$$|\gamma(\ell_r\rho,\theta)| = \frac{2J_1(\frac{\pi\ell_r^2}{2\lambda R}\rho)}{\frac{\pi\ell_r^2}{2\lambda R}\rho} . \qquad (59)$$

Letting $b = \frac{\pi\ell_r^2}{2\lambda R}$,

$$|\gamma(\ell_r\rho,\theta)|^2 = 4\left[\frac{J_1(b\rho)}{b\rho}\right]^2 \tag{60}$$

and combining (60) with (53)

$$K = \pi\left(\frac{b}{8}\right)^2\left[\int_0^1 [\cos^{-1}\rho-\rho(1-\rho^2)^{1/2}]\,\frac{J_1^2(b\rho)}{\rho}\,d\rho\right]^{-1} \tag{61}$$

or

$$K = \pi\,\frac{b^2}{64}\left[\int_0^b J_1^2(x)\left(\frac{1}{x\cos(x/b)} - \frac{(1-(x/b)^2)^{1/2}}{b}\right)dx\right]. \tag{62}$$

Integral evaluation by numerical techniques results in the plot of K vs. $b(=\pi\ell_r^2/2\lambda R)$ shown in Figure 18. Appendix A lists the program used to arrive at these results.

Two assumptions made may shift the K vs. b curve in opposing directions. The first, that a uniform field distribution at the transmitting aperture exists, is not really true. A complex mode structure prevails in most cases for lasers used in laser radar. With increasing complexity the K vs. b curve shifts upward (i.e., a larger K value is observed for any particular b than indicated in Figure 18). The second assumption, the condition of total beam interception, is often not true. If the condition of partial beam interception prevails, the number of observed coherence cells should decrease with decreasing scattering volume size.

If these assumptions hold, the results differ markedly from those given by the coherence area relation. Born and Wolf[50] show the diameter of the circular area that is illuminated almost coherently (regarding a departure of 12 per cent in the degree of coherence from the ideal value unity as the maximum permissible departure) by a quasi-monochromatic, uniform source of angular radius $\alpha = \rho/R$ is

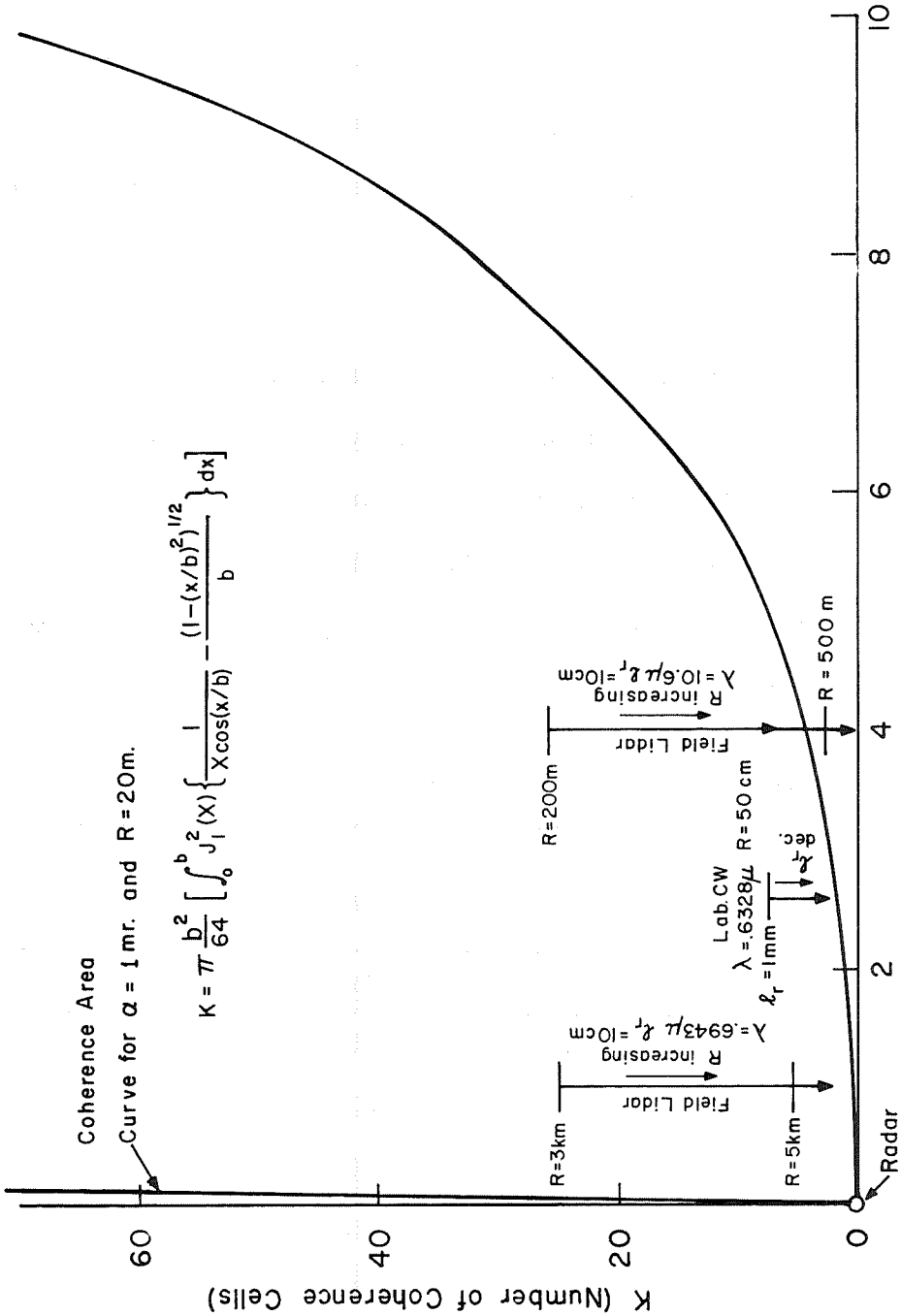

Figure 18. Number of observed coherence cells as a function of normalized range.

$$d_c = 0.16\ \bar{\lambda}/\alpha \qquad (63)$$

where $\bar{\lambda}$ is the mean wavelength of the source. The nearly vertical line on the left in Figure 18 is (63) plotted for an angular radius of one milliradian and a range of 20 meters. Any larger range will result in a curve shifted still further to the left and with a steeper slope. It is, thus, quite obvious that the results of (62) and (63) differ greatly. Many fewer coherence areas for a given aperture will be observed than "normally" expected.

As K in Figure 18 approaches one (i.e., one coherence area), wide fluctuations in the observed intensity will occur. Thus, any one signal signature will differ widely from others and correlation of signatures will no longer exist. Figure 18 shows the spectrum of coherence cell numbers to be expected with typical laser radar systems. Two example cases result in the data appearing in Table 2.

Table 2. Coherence Cells vs. Range.

$\lambda = .6943\mu$ $\ell_r = 10$ cm.		$\lambda = 10.6\mu$ $\ell_r = 10$cm	
R(m)	K	R(m)	K
$\leq$2000	$\geq$100	200	26
2000	100	400	4
3000	25	600	1.5
4000	10	800	0.8
6000	3.8	1000	0.5
6000	3.8	$\geq$2000	$\leq$0.2
8000	2.0		
$\geq$10000	$\leq$1.0		

At the .6943μ ruby laser operating wavelength, not until a range of 10 km is attained does the coherence cell number become one or less. Thus, for a ruby laser radar system, a sufficient number of coherence cells are present across the receiving aperture to spatially average signal returns. In the lower atmosphere a typical laser radar will, therefore, not experience wide fluctuations in signal returns. Note, however, that as the wavelength increases, the range at which the receiver aperture becomes equal to a single coherence cell decreases. As Table 2 indicates, when the wavelength is 10.6μ (the wavelength of the CO_2 laser) spatial detection effects due to coherence may become pronounced long before a one kilometer range is reached. As the wavelength increases, the range up to which spatial effects can be neglected decreases.

Two important conclusions can be drawn from this section's analysis of spatial detection effects:

1. No distortion of laser radar signal signatures should be expected for present typical operating conditions (i.e., λ=.6943μ and ℓ_r=10 cm).
2. With development of longer wavelength laser radars to monitor signal returns at pollutant gas absorption lines, concomitantly larger receiver apertures must be used or else widely varying signal signatures will result even though similar conditions prevail.

3.3 Partially Dependent Scattering

The initial assumption of section 3.2 was that a completely dependent scattering process prevails. It is obvious that this may not hold under all conditions. First, the longitudinal coherence of the source may be less than the scattering volume length. Second, the transverse coherence

of the source may be less than the scattering volume width. Third, there may be a substantial degradation in source (or, equivalently backscattered) coherence along the path. Fourth, if averaging over several pulse signatures (or time averaging of any sort) is undertaken, proper averaging of the coherent portion must be carried out--or spurious results must be accepted.

Longitudinal coherence is often quickly explained away by suggesting that there is a unique coherence length to light, $\Delta\ell$, given by

$$\Delta\ell = \frac{(\bar{\lambda})^2}{\Delta\lambda} \tag{64}$$

where $\bar{\lambda}$ is the center wavelength of the source spectral distribution and $\Delta\lambda$ is its spread at half-intensity. This, however, assumes a continuum in source output across the spectral distribution. Many sources discriminate for or against certain wavelengths within the spectral distribution. Specifically, the laser oscillates in several adjacent axial modes whose intensities are determined by the Doppler-broadened emission line.

The normally assumed spectral intensity distribution for a laser is (see Figure 19a)

$$j(x) = j_o e^{-\alpha^2 x^2} \sum_{n=N}^{M} \exp[-\beta^2 (x-x_n)^2] \tag{65}$$

where

$$x_n = (f+n)\Delta x$$

$$-1/2 \leq f \leq 1/2$$

$$\Delta x = \pi/L$$

$$\alpha = c(\ell n\ 2)^{1/2}/\pi\Delta\nu_D$$

$$\beta = c(\ell n\ 2)^{1/2}/\pi\Delta\nu_M$$

COHERENCE OF SOURCE

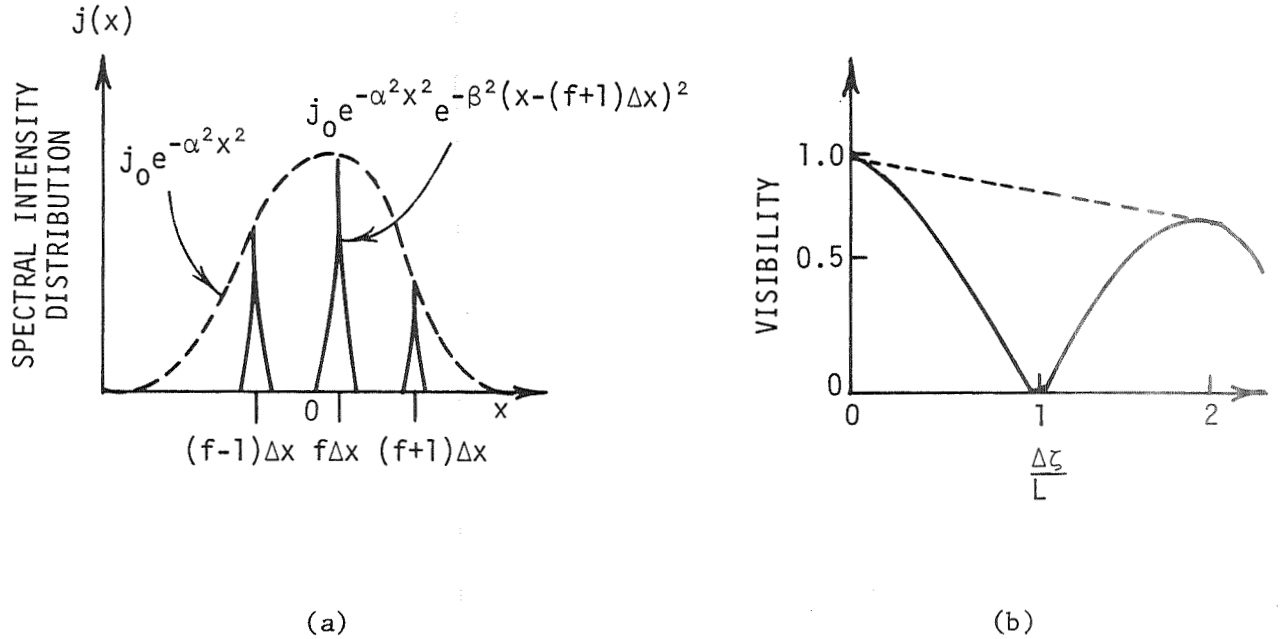

Figure 19. Relation of source spectral distribution to source coherence properties.

j_o is a normalizing constant, $e^{-\alpha x^2}$ represents the Doppler-broadened emission line of the laser, and the terms of the sum represent the oscillating axial modes allowed by the relation

$$q\lambda = 2L, \tag{66}$$

where q is a positive integer and L is the optical-cavity length of the laser. The summation is taken over the $p = |M-N|+1$ adjacent modes nearest the center of the Doppler line ($\bar{k}$). The parameter x_n is the number of wave numbers from $\bar{k}$ to the center of the nth axial mode; Δx is the axial-mode separation determined from (66); and f is the fraction of the n=0 mode from k, in terms of Δx. The parameters $\Delta\nu_D$ and $\Delta\nu_M$ are the full width at half-maximum intensity of the Doppler-broadened envelope and of an axial mode, respectively.

An experimental observation of the effect of such a spectral distribution can be achieved by measurement of the fringe visibility in a laser-illuminated two-beam interferometer. Erickson and Brown[51] have calculated the expected fringe visibility for a source of spectral distribution, as in Figure 19a. The result [Equation (6a) in their paper] is fairly complex. However, Figure 19b shows the result pictorially. The envelope is given by $\exp[-(\Delta\mathcal{L}/2\beta)2]$, where $\Delta\mathcal{L}=2mL$, and m is an integer. The important characteristics are: first, the periodicity in fringe visibility of twice the optical-cavity length; second, the vanishing of the periodicity for a continuum mode structure beneath the Doppler envelope with the concomitant V=1/2 point at

$$\Delta\mathcal{L} = 1.67 \times 10^8/\Delta\nu_D. \tag{67}$$

The laser radar problem can thus be categorized by slabs of dependent scattering adding independently, as against a completely dependent scattering process. (The dependent scattering between alternate slabs can be neglected since only a few slabs have to be considered for the problem at hand.)

Further, Chang and Kilcoyne[52] have carried out a detailed experimental analysis of the transverse coherence for a ruby laser and have found (as might be expected) a periodicity in the visibility. This suggests that, as in the longitudinal case, slabs of coherence in the transverse direction can be assumed.

The question of path dependent coherence degradation must be considered from two viewpoints. First, atmospheric turbulence may contribute markedly to the deterioration of coherence properties. However, as Consortini, et al.[53] indicate, as long as the characteristic periods of atmospheric turbulence are much greater than the pulse duration, no degradation in coherence will occur. This is obviously true for laser radar since pulse durations are 100 nanoseconds or less.

Second, multipath or time delay effects may cause degradation. Although nonscattered photons retain their coherence relationship (one to another), if photons undergo multiple scattering effects and in so doing return to the original source beam path, a loss of coherence may result. Kerr et al.[54] have, however, shown that unless multiple scattering effects are prevalent enough to cause distortion in the pulse shape, coherent degradation is negligible. To determine whether this occurs in laser radar is a complex problem and will be delayed to Chapter 4.

Since averaging of several signal signatures is the nearly universal approach to laser radar data acquisition, an analysis of the effect of

dependent scattering on the average power in the received signal is undertaken in ensuing paragraphs. Note that scattering particles in any instantaneous scattering volume are stationary with respect to the detection process, for particles move far less than $\lambda/10$ during the pulse time of 100 nanoseconds or less. For clarity, it should be pointed out that the theory of section 3.2 takes account of the fact that for a short time interval of the light pulse, the conditions of the experiment are essentially nonergodic; i.e., during the time length of the pulse, the point in configuration space representing the position of the scattering system passes through only a finite part of the whole (infinite) trajectory, so that the relation

$$\frac{1}{t}\int_0^{\tau} I[Z(t)]dt \overset{\sim}{\sim} \langle I(z)\rangle$$

did not hold. (Note: I is the instantaneous scattered intensity which depends on the coordinate Z of the system in configuration space, and the symbol < > means ensemble average.) In this section, since an average is taken over a substantial portion of the possible positions of the scattering system, the approximation is assumed valid.

Given the multimode output of the laser source, one is left with consideration of a scattering volume split into a number of dependently scattering regions adding independently. Consider the situation as illustrated in Figure 20. Divide the total number of scatterers N into m aggregates. Depending on the number of axial modes under the Doppler line, $\Delta\nu_D$, and the transverse coherence of the source, m could be 1 or a very large number.

Assume n_ℓ particles in the ℓth aggregate. Then

$$\sum_{\ell=1}^{m} n_\ell = N \qquad (68)$$

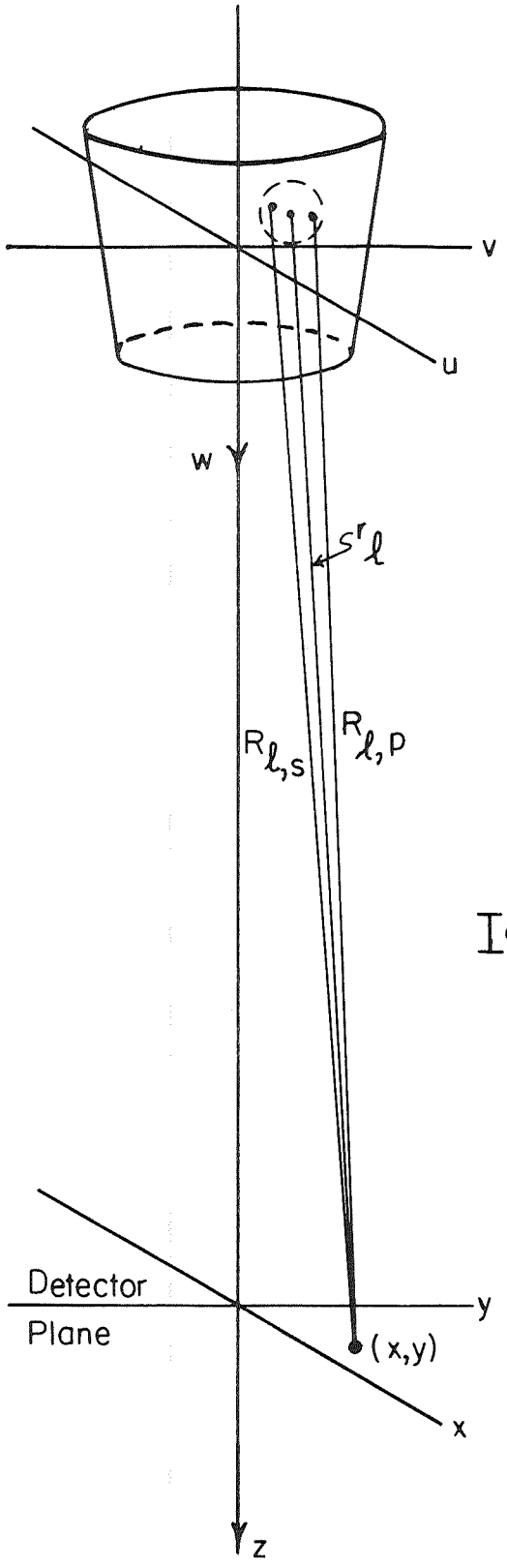

$$I \propto \sum_{\substack{s=1 \\ s \neq p}}^{n_\ell} \left\langle \frac{e^{-i2k(R_{\ell,p} - R_{\ell,s})}}{R_{\ell,p}\, R_{\ell,s}} \right\rangle$$

Figure 20. Configuration for partially dependent scattering analysis.

Scatterers within any one aggregate dependently scatter, while the m aggregates independently scatter and are randomly distributed within the bounds of the total scattering region. Further, scatterers within any one aggregate possess similar statistical properties and each aggregate will be assumed to have the same size distribution and the same mean radius scatterer. Also, all scatterers will, for simplicity, be assumed to have the same backscatter intensity. The variations of the coordinates of the scatterers form a stable, stochastic process.

The scattered field at the detector plane is

$$E(x,y;t) = \sum_{i=1}^{N} E_i$$

$$= \sum_{i=1}^{N} E_{oi}(t-R_i/v)\,\frac{e^{-i(kR_i-2\pi\nu_s t)}}{R_i} \quad . \quad (69)$$

The average power in the received signal may be represented by

$$\tilde{P}_r \propto EE^* = C\left[N + \sum_{\substack{i=1 \\ i\neq j}}^{N}\sum_{j=1}^{N} E_{oi}(t-R_i/v)\,\frac{e^{-i(kR_i-2\pi\nu_s t)}}{R_i}\,E^*_{oj}(t-R_j/v)\,\frac{e^{i(kR_j-2\pi\nu_s t)}}{R_j}\right]. \quad (70)$$

The first part represents the independent scattering contribution and the second represents the dependent contribution. The latter part becomes zero when the scatterers act independently for R_i-R_j assumes various values with equal probability.

A separation of the scatterers in one aggregate from those in others is the first order of business. Thus

$$\sum_{i=1}^{N}\sum_{\substack{j=1 \\ i\neq j}}^{N} E_{oi}(t-R_i/v)\,\frac{e^{-i2(kR_i-2\pi\nu_s t)}}{R_i}\,E^*_{oj}(t-R_j/v)\,\frac{e^{-i2(kR_j-2\pi\nu_s t)}}{R_j}$$

$$= \sum_{i=1}^{N} \sum_{\substack{j=1 \\ i\neq j}}^{N} E_{oi}(t-R_i/v)E^*_{oj}(t-R_j/v)\,\frac{e^{-i2k(R_i-R_j)}}{R_iR_j} \qquad (71)$$

$$= \sum_{\ell=1}^{m} \sum_{p=1}^{n_\ell} \left[\sum_{\substack{s=1 \\ s\neq p}}^{n_\ell} E_{\ell,p}(t-R_{\ell,p}/v)E^*_{\ell,s}(t-R_{\ell,s}/v)\,\frac{e^{-i2k(R_{\ell,p}-R_{\ell,s})}}{R_{\ell,p}R_{\ell,s}} \right.$$

$$\left. + \sum_{\substack{k=1 \\ k\neq \ell}}^{m} \sum_{s=1}^{n_\ell} E_{\ell,p}(t-R_{\ell,p}/v)E^*_{\ell,s}(t-R_{\ell,s}/v)\,\frac{e^{-i2k(R_{\ell,p}-R_{k,s})}}{R_{\ell,p}R_{k,s}} \right] \qquad (72)$$

where the first subscript of $R_{\ell,p}$, $R_{k,s}$, etc. denotes the aggregate number in running order and the second denotes the scatterer number in a particular order.

The second term in the brackets of (72) represents the contribution of scatterers from different aggregates. However, since we have assumed the individual aggregates act independently, this term is zero. Thus, the entire problem simplifies to the evaluation of

$$\sum_{\substack{s=1 \\ s\neq p}}^{n_\ell} E_{\ell,p}(t-R_{\ell,p}/v)E^*_{\ell,s}(t-R_{\ell,s}/v)\,\frac{e^{-i2k(R_{\ell,p}-R_{\ell,s})}}{R_{\ell,p}R_{\ell,s}}\,. \qquad (73)$$

Each scatterer causes the same backscatter field. Then

$$E_{\ell,p}(t-R_{\ell,p}/v)E^*_{\ell,s}(t-R_{\ell,s}/v) = E_{\ell,p}(t)E^*_{\ell,s}\left(t-\frac{R_{\ell,p}-R_{\ell,s}}{v}\right). \qquad (74)$$

The assumption that all scatterers within an aggregate scatter dependently allows the retardation $\frac{R_{\ell,p}-R_{\ell,s}}{v}$ in the argument of $E^*_{\ell,s}$ to be neglected (i.e., the path difference is small compared to the coherence length).

Now taking the ensemble average of (73), and letting $I_o = E_{\ell,p}E^*_{\ell,s}$ (the intensity due to any one scatterer) results in

$$\left\langle \sum_{\substack{s=1 \\ s\neq p}}^{n_\ell} I_o \frac{e^{-i2k(R_{\ell,p}-R_{\ell,s})}}{R_{\ell,p}R_{\ell,s}} \right\rangle \quad \text{or}$$

$$\left\langle I_o \sum_{\substack{s=1 \\ s\neq p}}^{n_\ell} \frac{e^{-i2k(R_{\ell,p}-R_{\ell,s})}}{R_{\ell,p}R_{\ell,s}} \right\rangle . \tag{75}$$

Initially, it was considered essential to incorporate spatial effects at the detector plane into the present analysis. Ivanov and Khairullina[55] describe a possible peaking of intensity in the back-scatter direction due to coherence. The question of angular effects in dependent scattering of coherent radiation has been treated by several authors[56,57,58] in which it was pointed out that this phenomenon occurs not only in the direction of the direct beam but also at angles close to it. However, Ivanov and Khairullina[55] describe a semiquantitative evaluation which indicates the phenomenon occurs in the back-scatter and near back-scatter direction as well. Incorporation of spatial effects in any forthcoming analysis appears, then, to be important. Thus, exact relations for $R_{\ell,p}$ and $R_{\ell,s}$ were written as

$$R_{\ell,p} = [(x-(u_\ell+u'_p))^2+(y-(v_\ell+v'_p))^2+(h-(w_\ell+w'_p))^2]^{1/2} \tag{76}$$

and

$$R_{\ell,s} = [(x-(u_\ell+u'_s))^2+(y-(v_\ell+v'_s))^2+(h-(w_\ell+w'_s))^2]^{1/2} \tag{77}$$

where h is the vertical distance from the detector plane to the uv plane passing through the center of the scattering region, (u_ℓ,v_ℓ,w_ℓ) is the location of the ℓth aggregate, and $(u'_\ell,v'_\ell,w'_\ell)$ is the location of the scatterer

under consideration within the ℓth aggregate. After several approximations and simplifying assumptions, an equation for the average power in the received signal was obtained which contained a triple integral over the spherical coordinate system. A closed-form solution of the triple integral could not be obtained. Integration was performed by numerical analysis using the Gaussian quadrature summation technique. Numerical computation times were horrendously large. As the radius of the coherent aggregate increases, the number of evaluation points increases proportionately. To evaluate fifty intensity values in the x dimension at the receiver plane required IBM 360/75 computation times of 85 seconds and 43 minutes for aggregate radii of 10^{-6} and 10^{-5}m, respectively. Realistic values for aggregate radii of 10^{-3} through 1 m would cause far too large computation times.

Can the questions raised about spatial effects in the average power of the received signal be resolved without a detailed analysis? Ivanov and Khairullina have overlooked an important paper which answers this question. Twomey and Howell[59] have studied the relative merit of broadband and monochromatic radiation for the determination of visibility by backscatter measurements (but without regard to variations in the number of scattering particles). For a monochromatic source incident upon a scattering medium heterogeneous in size, anomalies rather than a necessary enhancement seem to occur. However, the most important conclusion for the problem at hand is that no variation in backscattered radiation effects at near backscatter directions (to several tens of milliradians-measured from the scattering volume) was observed. Since laser radar experiments usually maintain the detector within a few milliradians of the source, it can be concluded that spatial effects need not be taken into consideration in the determination of an average power at the receiver.

Although of a secondary nature, it should be mentioned that diffraction effects caused by the assumed coherent aggregate edge need not be monitored. As the radius of the coherent aggregate increases toward that of the scattering medium, the diffraction pattern at the receiver plane approaches the pattern due to the entire scattering volume itself. However, the first diffraction minimum of any aggregate is always greater than that of the scattering volume, and similarly for the second, third, etc., minimum. Thus, the diffraction pattern of the aggregates only slightly perturbs that of the scattering volume.

Assume now that spatial effects can be neglected in determining the average power in the received signal. In this case, the stochastic variable $R_{\ell,p}-R_{\ell,s} = (\Delta_\ell R)_{p,s}$ is equal to $(\Delta_\ell w)_{p,s}$ (see Appendix B)

$$(\Delta_\ell R)_{p,s} = w'_s - w'_p = (\Delta_\ell w)_{p,s} \quad . \tag{76}$$

Then, the expected value (mean value) of

$$\sum_{\substack{s=1 \\ s\neq p}}^{n_\ell} e^{-i2k(R_{\ell,p}-R_{\ell,s})}$$

is

$$T\{\Sigma\} = (n_\ell - 1) \int_{-\infty}^{\infty} e^{-i2ky} W_\ell(y)\, dy \tag{77}$$

where $W_\ell(y)$ represents the distribution density of the stochastic variable

$$y = (\Delta_\ell R)_{p,s} = R_{\ell,p} - R_{\ell,s}.$$

$W_\ell(y)$ must be determined.

To obtain a solution for W amenable to further analysis, spherical aggregates are assumed. Within any one sphere (i.e., any one aggregate) the scatterers may be found at any point with equal probability. Then,

$n_\ell(R-\bar{R})$, the distribution density at point R (where $\bar{R}$ denotes the center of the aggregate) can be represented by

$$n_\ell(R-\bar{R}) = \frac{1}{\frac{4\pi a_\ell^3}{3}} \frac{dV(R)}{dR} = \begin{cases} \frac{3}{4a_\ell^3}\,(a_\ell^2-(R-\bar{R})^2) & R-\bar{R} \leq a_\ell \\ = 0 & R-\bar{R} > a_\ell \end{cases} \tag{78}$$

where a_ℓ is the radius of the ℓth spherical aggregate. As Papoulis[60] points out, the relationship between the distribution density of a difference in stochastic variable R and that of the stochastic variable R, $n(R-\bar{R})$, may be represented by a convolution formula as

$$W_\ell(y) = \int_{-\infty}^{\infty} n_\ell(\zeta) n_\ell(\zeta+y)\,d\zeta. \tag{79}$$

When $2a_\ell \geq y \geq 0$

$$n_\ell(\zeta) = \frac{3}{4a_\ell^3}\,[a^2-\zeta^2] \text{ and}$$

$$n_\ell(\zeta+y) = \frac{3}{4a_\ell^3}\,[a_\ell^2-(\zeta+y)^2]$$

$$W_\ell(y) = \int_{-a_\ell}^{a_\ell-y} \left(\frac{3}{4a_\ell^3}\right)^2 [a_\ell^2-\zeta^2]\,[a_\ell^2-(\zeta+y)^2]\,d\zeta \text{ , and} \tag{80}$$

when $-2a_\ell \geq y \geq 0$

$$W_\ell(y) = \left(\frac{3}{4a_\ell^3}\right)^2 \int_{-a_\ell}^{a_\ell-(-y)} [a_\ell^2-\zeta^2][a_\ell^2-(\zeta+(-y))^2]\,d\zeta. \tag{81}$$

Thus,

$$W(y) = \begin{cases} \left(\frac{3}{4a_\ell^3}\right)^2 \int_{-a}^{a_\ell-|y|} [a^2-\zeta^2][a^2-(\zeta+|y|)^2]d\zeta & \text{for } |y| \leq 2a_\ell \\ 0 & \text{for } |y| \geq 2a_\ell \end{cases} \tag{82}$$

If the function of the integrand is written as a power series, the integration in (82) gives

$$W_\ell(y) = \begin{cases} \left(\frac{3}{4}\right)^2 \frac{1}{a_\ell} \sum_{n=0}^{\infty} c_n |y/a_\ell|^n & |y| \leq 2a_\ell \\ 0 & |y| > 2a_\ell \end{cases} \tag{83}$$

where

$$c_0 = 16/15;\ c_1 = 0;\ c_2 = 4/3;\ c_3 = 2/3;\ c_4 = 0$$

$$c_5 = -1/30;\ c_6 = 0;\ c_7 = 0;\ \ldots$$

Figure 21 shows a plot of $a_\ell W_\ell(y)$ vs $|y/a_\ell|$. The linear approximation to $W_\ell(y)$ is given by

$$W_\ell(y) \approx \frac{0.675}{a}\left(1-\frac{1}{1.5}|y/a_\ell|\right) \qquad |y| \leq 1.5a_\ell \tag{84}$$

$$= 0 \qquad |y| > 1.5a_\ell$$

Substituting (83) in (77),

$$T = (n_\ell-1)\int_{-\infty}^{\infty} e^{-i2ky} W_\ell(y)dy =$$

$$= (n_\ell-1)\int_{-1.5a_\ell}^{1.5a_\ell} e^{-i2ky}\left(\frac{0.675}{a_\ell}\right)\left(1-\frac{1}{1.5}|y/a_\ell|\right)dy \tag{85}$$

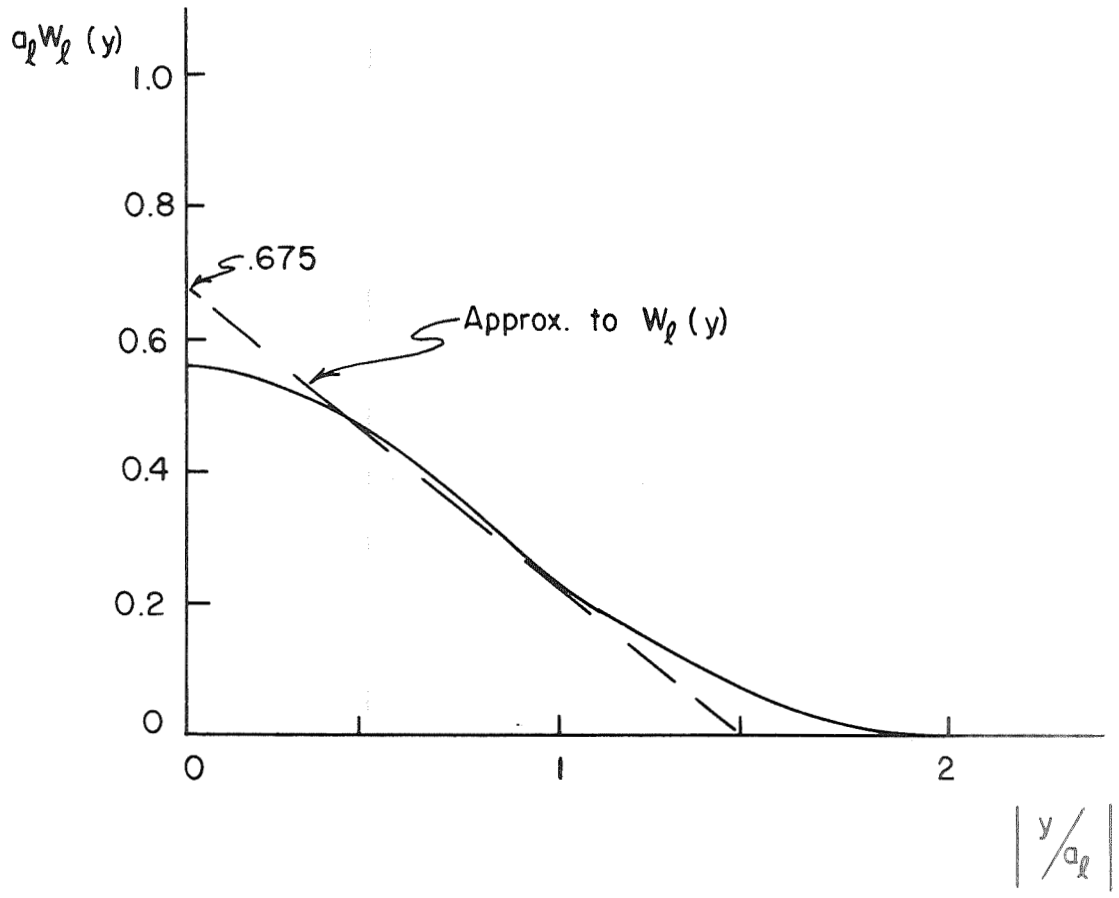

Figure 21. Approximating the distribution density of the stochastic variable $R_{\ell,p}-R_{\ell,s}=(\Delta_\ell R)_{p,s}$.

$$T = (n_\ell - 1)\left[\frac{0.90}{(2ka_\ell)^2}\,(1-\cos(1.5[2ka_\ell]))\right]. \tag{86}$$

Thus,

$$\sum_{\substack{i=1 \\ i\neq j}}^{N}\sum_{j=1}^{N} e^{-i2k(R_i-R_j)} = \sum_{\ell=1}^{m} n_\ell(n_\ell-1)f(2ka_\ell) \tag{87}$$

where

$$f(2ka_\ell) = \frac{0.90}{(2ka_\ell)^2}\,(1-\cos(1.5[2ka_\ell])).$$

Finally,

$$P = c\sigma\left[N + \sum_{\ell=1}^{m} n_\ell(n_\ell-1)f(2ka_\ell)\right]. \tag{88}$$

If one aggregate satisfies the conditions prevailing (i.e., laser coherence properties are such as to cause a totally dependent scattering process), then the ratio of dependent to independent scattering is

$$R = \frac{\sum_{\ell=1}^{m} n_\ell(n_\ell-1)f(2ka_\ell)}{N} = Nf(2ka_\ell). \tag{89}$$

If m aggregates prevail,

$$R = \frac{N}{m}\,f(2ka_\ell). \tag{90}$$

For simplicity assume the scattering volume to be a sphere of radius a. Crudely, then, $a_\ell = a/(m)^{1/3}$ and

$$R = \frac{N}{m}\,f(2k\ a/(m)^{1/3}). \tag{91}$$

For typical laser radar operating conditions a = 1m at a range of 1 km and λ = .6943μ Figure 22 shows a plot of R vs. m for N = $2\text{x}10^{25}$ (Figure 22a), the average atmospheric molecular constituent density, and N = 10^{10} (Figure 22b), which approximates the maximum pollutant particulate density to be expected. (For example, see Barrett.[17]) $R_{max.}$ is the maximum ratio possible. Since the $1-\cos(3ka_{\ell})$ term is present in (90), the actual ratio can fluctuate between zero and the calculated maximum value.

3.4 Conclusions

This chapter has shown that with a small enough aperture and appropriate coherence properties of the laser source, dependent scattering effects can be observed. In fact, discrimination of backscatter due to molecular constituents from backscatter due to pollutant particulates can be achieved by a coherent detection of dependent scattering. Two modes of operation are required. One mode consists of a multishot average of spatially coherent detection (i.e., small enough detector aperture) utilizing a single mode laser source so that the entire instantaneous scattering volume gives rise to dependent scattering (i.e., m=1, one dependently scattering spherical aggregate makes up the scattering volume). The second mode consists of a multishot average of incoherent detection utilizing the more normal multimode laser source giving rise to many dependently scattering aggregates adding independently. The first mode of operation gives an N^2 return from molecular atmospheric constituents (since Figure 22 shows that both the N^2 return from pollutant particulates and the N return from molecular constituents are negligible compared to the N^2 return from molecular constituents). Since the other parameters in (88) are known, an equivalent N return--due only

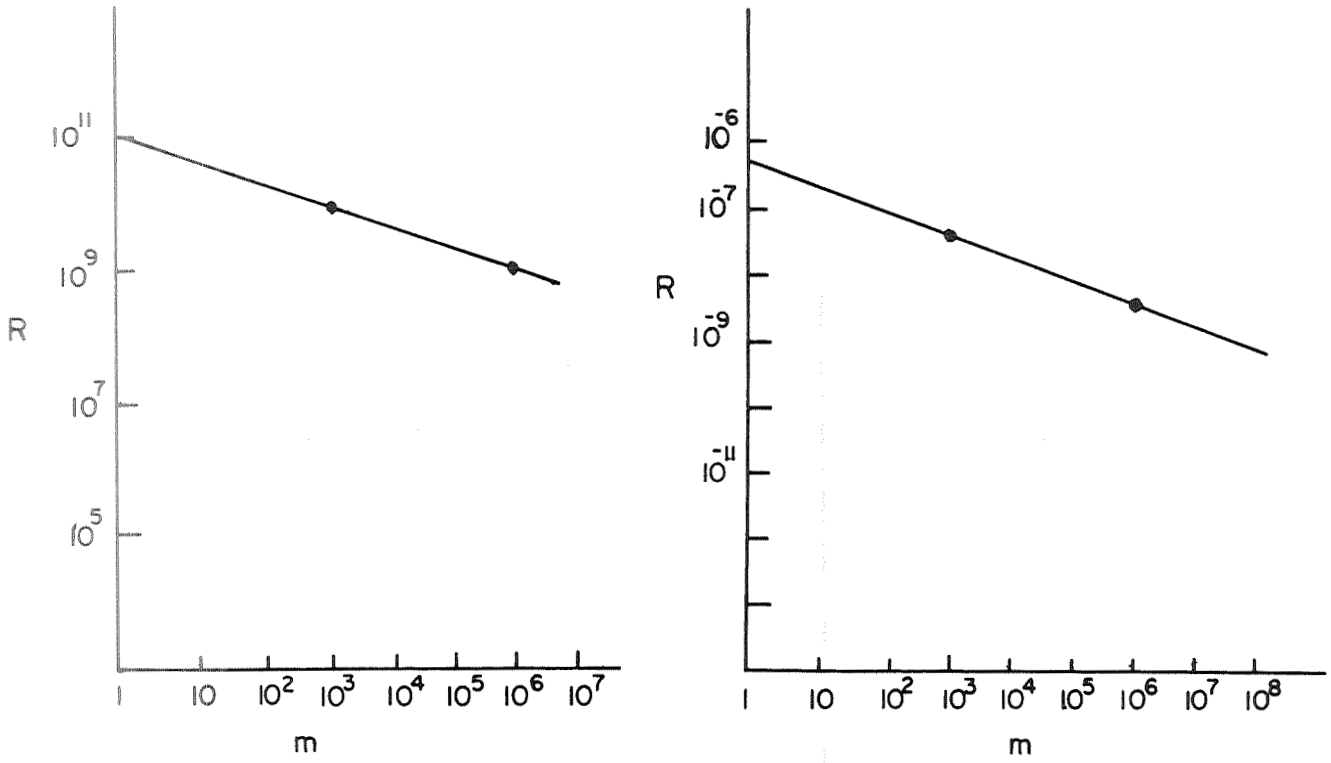

Figure 22. The maximum ratio of dependent to independent scattering vs. the number of coherently scattering aggregates.

to molecular constituents--can thus be plotted. This can then be subtracted from the N return from both molecular constituents and pollutant particulates obtained through the second mode of operation to give a profile of the pollutant particulate concentration alone.

Additionally, the N return plot of molecular constituents allows for the determination of temperature profiles by utilizing (16) of Chapter 2.

4. MULTIPLE SCATTERING EFFECTS

We don't know where we're going, but we're on our way.
--Stephen Vincent Benét

As alluded to in section 3.3, multipath or time delay effects give rise to very difficult analysis considerations. A number of theoreticians have long grappled with the concepts essential to a discussion of multiple scattering. Prominent among the elegant analyses is the work of Twersky.[61,62,63] In particular, the determination[64] of multiple scattering equations for a plane wave normally incident on a slab region of randomly distributed particles is relatively simple if the dimensions of the particles are large compared to wavelength and if their physical parameters are close to those of the embedding medium. For any such large tenuous scatterer, the backscattered amplitude is very small compared to the forward-scattered amplitude, and the scattered-radiation pattern is peaked sharply around the forward-scattering direction. The model of Twerksy, described above, is applicable to the laser radar scattering problem. However, scattering particles in the laser radar case have diameters on the order of the wavelength and indices of refraction significantly larger than one. Twersky assumes particles to be much larger than the wavelength and to have indices of refraction close to one. In fact, no analytical, closed form solution for the effects of multiple scattering under conditions applicable to laser radar air pollution backscatter measurements has yet been achieved.

A second important reason for consideration of the time delay due to multiple scattering effects has become apparent after completing the analysis of section 3.3. Once arriving at the equation for the average

power in the received signal, scrutiny of it ((88), section 3.3) indicates that a saturation term is not present. That is, as the number of scattering particles increases, no leveling of the dependent scattering (N^2) effect is present. Since such a saturation must eventually occur, something has been neglected. Following (74) in section 3.3, the assumption was made that the retardation time $\frac{R_{\ell,p}-R_{\ell,s}}{v}$ in the argument of $E^*_{\ell,s}$ can be neglected. If the path difference caused by multiple scattering becomes comparable to or greater than the coherence length of the scattering system source, this assumption is no longer valid. Once the time delay due to multiple scattering effects is greater than the coherence time ($\Delta t_m > t_c$), distortions appear in the coherence properties of radiation incident upon the scattering volume. To monitor this effect quantitatively, one must determine what portion of the incident radiation is delayed or otherwise diverted from the initial pulse. The problem description of sections 4.1 and 4.2 parallels that of Kerr.[54]

4.1 Single Scattering

First, a consideration of single scattering will give perspective. If some of the photons comprising a pulse are scattered, the resultant delay in their arrival at a receiver can be easily calculated. In Figure 23, if 2θ is the angular beam divergence at the source, 2ϕ is the receiver field of view (f.o.v.), and L is the distance that separates the receiver and source, then the maximum path length for single scattered photons will be ACB. The time delay relative to AB is easily found as

$$\Delta t = \Delta L/C = L\theta\phi/2C. \tag{92}$$

For a typical laser radar system used in lower atmosphere studies

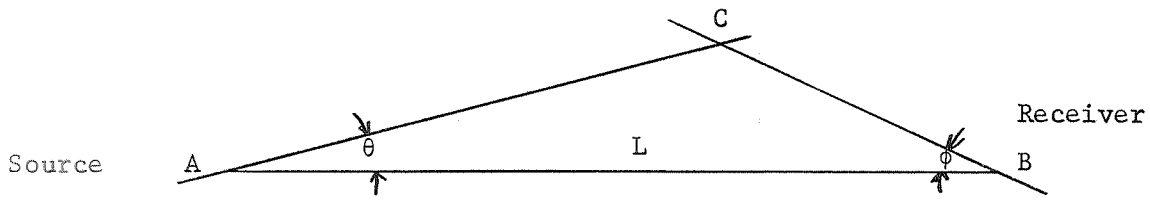

Figure 23. Single scattering configuration.

L = 2-10000 meters

θ = 1-4 mr

ϕ = 2-10 mr

and thus

$$\Delta t \leq .66 \text{ nanosec.} \tag{93}$$

This value of Δt may well be on the order of typical coherence times of a laser radar system. It is of interest to determine how many photons are delayed by amounts comparable to the maximum delay of Equation (92). To estimate this (neglecting multiple scattering), consider Rayleigh scattering, for which the radiation at the receiver is[64]

$$I = I_o \frac{4\pi^2}{\lambda^4} \frac{(\mu-1)^2}{r^2 n} V\left[\frac{1+\cos^2\beta}{2}\right] \tag{94}$$

where I_o is the irradiance of light incident on the scattering volume V, λ is the wavelength, r is the distance from the scattering volume to the receiver, n is the scattering density, μ is the index of refraction, and β is the angle between the initial direction of the light and its final direction. If we take the source power to be I' and assume the beam to be uniformly spread, the irradiance at the scattering volume, I_o is

$$I_o = \frac{I'a}{\pi r^2 \sin^2\phi} \tag{95}$$

for the scattering volume at C in Figure 23. The volume at C is

$$V = 2\pi r \sin\phi \ (15.67)(14.58) \ m^3$$

and

$$n = 2.55 \times 10^{25}/m^3, \ \mu - 1 = 3 \times 10^{-4}.$$

The result is

$$\frac{I}{I'} = 5 \times 10^{-12}. \tag{96}$$

This is the single-scattered Rayleigh condition. For the worst possible case of particles of exactly the right particle size distribution, an increase of up to 10^6 may be expected.[65] However, such an increase would seldom occur in conjunction with single scattering only and a more reasonable number is 10^3. In either case, the fraction of optical power so scattered is negligible.

4.2 Multiple Scattering

It should be evident that if noticeable pulse distortion effects are to be observed, the mechanism of multiple scattering in a relatively dense aerosol medium must be involved. As Kerr[54] points out, a literature search for analyses of distortion of short pulses uncovers very little. A number of investigators have predicted the size of the multiple scattering effect using analytical[66,67] and Monte-Carlo methods.[68,69,70] A summary of these predictions follows in the next five paragraphs. Important parameters are path length Z, extinction coefficient σ, the

mean path L = 1/6, the optical thickness R = Z/L, and the receiver field of view. Multiple scattering is important for $R \geq 0.1$. Note that even under similar circumstances, there is no great agreement.

Chatterton[66] used an approximate ray-tracing analysis to predict time dispersions for R = 7 on the order of

$$\Delta t \sim 2\alpha^2(L/c) \tag{97}$$

where 2α is the half-power angular divergence owing to scattering. Chatterton estimated an α of 2°, and, thus, source divergence was not a factor. The resultant estimates of time dispersion for L = 3.52 km and R = 7 ranged from 1 nsec to 30 nsec. Some experimental evidence of a 5 nsec. smearing was given.

Heggestad[67] employed an analytical technique to estimate the time dispersion for large optical thickness and predominantly forward scattering (assumption is made that any light which is scattered through an accumulated total angle of about 2 radians is so attenuated as to be negligible compared to the forward scattered light) as

$$\Delta t = \frac{Z}{c\sqrt{R}} [2+1/\sqrt{R}] \tag{98}$$

assuming the receiver field of view is much smaller than the angular spread due to scattering. Using the conditions of the previous paragraph, the prediction of time dispersion is on the order of 1μ sec.

The above predictions for optical propagation through clouds do not apply to ground-based experiments. In addition, they substantially disagree.

Turning thus to Monte-Carlo analyses, reference is made to a preliminary Monte-Carlo result of Kattawar[69] in which more typical characteristics were utilized:

Beam divergence = 5 mrad

Receiver field-of-view = 3 mrad

Optical thickness = 10

Range = 1 km

Maximum disp. = 1/3 nsec at 1 km

Kattawar[69] indicates that values of 1 mrad for beam divergence and optical thickness of one or less, more typical of laser radar experiments, will further increase the maximum dispersion. Danielson[70] carried out Monte-Carlo analyses but with little interest in determination of path lengths.

Given the above results (or lack of results) a Monte-Carlo simulation using parameters pertinent to laser radar was performed. The following paragraphs describe the model and results.

4.3 Monte-Carlo Simulation

Figure 24 shows the problem modeled with the orientation of the spherical coordinate system at any scatterer.

For the purpose at hand, it will be more revealing to observe photons which traverse the scattering medium and fall within a predetermined area (the aperture determined by the receiver field of view) rather than include the scattering process and then use a receiver field of view at the detector plane (at $z = 0$). An obvious reason for this is the very small backscatter coefficient requiring far too many case histories (photon paths) to obtain statistically significant results at the detector plane. Further, we

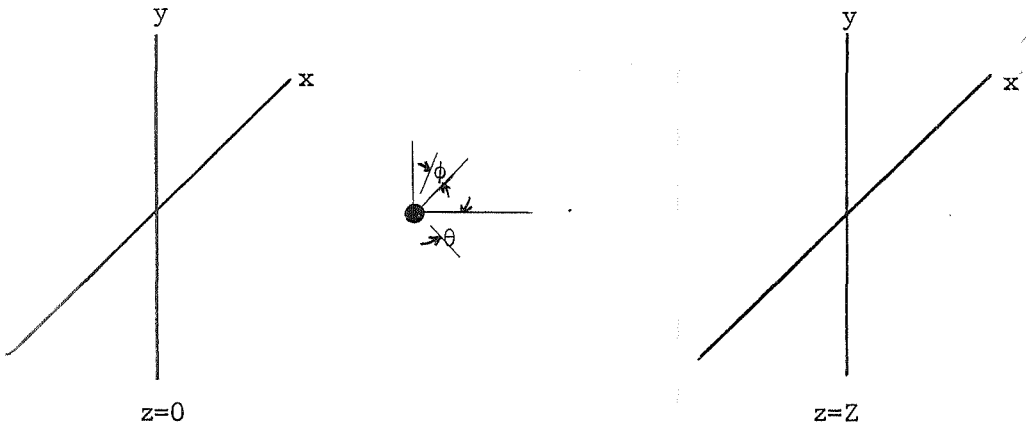

Figure 24. The Monte-Carlo model.

are interested in the spatial smearing effect due to multiple scattering at the assumed scattering volume. This can better be monitored by recording the (x,y) coordinates of photons on arrival at the z = Z plane. Radiation returning to the detector plane will undergo the same process as that being modeled with the additional constraint of a smaller aperture. Again, by monitoring the (x,y) coordinates of photons, this constraint can be taken into account.

Assume each case history to begin with a photon entering the scattering medium at (x,y,z,t) = (0,0,0,0) and at vertical incidence (ie., $\perp$ to xy plane). The existence of a finite aperture at the source and the divergence of the source can be neglected. The source aperture being 10 cm in diameter or less is (for Z > 100 m) a factor of 10 or more smaller than the scattering-volume diameter. The beam divergence, being only a milliradian or two under most conditions, is far less than the increment in scattering angle to be considered later. Thus, the divergence is far too small to be resolved.

The path length traversed in the medium before the first scattering is

$$L = L_o \, \ell n(1/R_i) \tag{99}$$

where L_o is the mean distance between scatterings and R_i is a random number between zero and one generated by the computer.

Now,

$$L_o = \frac{1}{N\pi r_{eff.}^2} \tag{100}$$

since $r_{photon} \tilde{\gtrsim} 0$.

N is the particle number density and

$r_{eff.}$ is the effective scatterer radius.

For Mie scatterers, the assumption is made that pollutant particulates form an ensemble. Thus equating this ensemble to the same number of spherical scatterers, a distribution in scatterer size from approximately .01 to 20μ is to be considered. Since the distribution in size exists, L_o cannot be theoretically determined. By turning to experimental data, a value for L_{OM} (mean distance between scatterers for Mie scatterers) can, however, be obtained.

L_{OM} is equal to the atmospheric visibility in a single-scattering medium. The visibility is defined as that distance at which the intensity has dropped to 1/e of its value upon entering the atmospheric medium. This is precisely L_{OM}. Barrett[17] has experimentally determined the particulate load density Q which is related to the visibility as

$$V = 1212 \, (Q/4.96 + 3.82). \tag{101}$$

Using this equation and the data in Barrett's paper, the visibility is found to be

$$50 \text{ km} < V < 100 \text{ km} \quad \text{for a clear atmosphere}$$

and

$$10 \text{ km} < V < 50 \text{ km} \quad \text{for a polluted atmosphere.}$$

Under extremely polluted conditions, V as low as .5 km may be observed.

For Rayleigh scatterers, Collis[71] indicates N_R to be $2.55 \times 10^{25}/m^3$ at 0.0 km and $1.52 \times 10^{25}/m^3$ at 5 km. For our purposes, $N_R = 2 \times 10^{25}$ is sufficient. The radius of Rayleigh atmospheric scatterers can be calculated. At first thought, this radius may be approximated by the radius of a nitrogen or oxygen molecule--both approximately 2 Å. Second, one might think it to be the radius of an electron $r_o = e^2/mc^2$. Of course, an effective radius must be calculated. Collis[71] shows the elementary (one scatterer) total cross section to be

$$C_{Ray.} = \frac{8\pi}{3} \left(\frac{2\pi}{\lambda} \right)^4 \alpha^2 \frac{6+3\delta}{6-7\delta} \tag{102}$$

λ = wavelength

δ = depolarization factor = 0.035 due to anisotropy of the atmosphere

α = molecular polarizability = $2 \times 10^{-30} (m^2)$ of scatterer

and

$$C_{Ray.} \tilde{\approx} 1.71 \times 10^{-31} m^2$$

Thus,

$$L_{OR} = \frac{1}{N_R \, C_{Ray}}$$

or

$$L_{OR} \tilde{\approx} 2.92 \times 10^5 m \tag{103}$$

Note that L_{OR} is, in fact, the limiting value for L_{OM} and the value of 292 km for L_{OR} agrees well with the values of L_{OM} obtained above. That L_{OM} and L_{OR} are both much greater than λ allows use of far field results for Mie and Rayleigh single scattering. Further, since the minimum L_{OM} is much greater than the wavelength, Mie scattering applies from another standpoint. The Mie theory does not apply to incident radiation other than a uniform plane wave. Although a spherical wave emanates from the scatterers, since $(L_{OM})\min/\lambda \tilde{\gg} 10^{10}$, the plane wave assumption is quite good.

Now at the scatterer a new vector (θ,ϕ) relative to the incident vector is chosen as

$\emptyset = 2\pi R_i$ where R_i is a new random number not related to any previous R_i.

$$R_i = \frac{\int_o^{\theta} p(\cos\theta')d\theta'}{\int_0^{\pi} p(\cos\theta')d\theta'} \qquad (104)$$

where $p(\cos\theta')$ is the scattering phase function.

Although one might be able to calculate the functional relationship on θ for the Rayleigh case, it is far easier to use the tables of Mie scattering and calculate a corresponding Rayleigh table.

van de Hulst[72] has shown that for a relative index of refraction (m) of 1.33 (approximating pollutants, although Barrett assumes m = 1.5) fluctuations in the intensity of scattering vs. angle are small in number. An increment in angle of 10°, except near the forward scattering direction, is sufficient for calculations. Gumprecht[73] has calculated the Mie scattering intensities for m = 1.33, $x = 2\pi r/\lambda = 6,8,10(5)40$, where r is the radius of the scattering particle. To properly model the atmosphere,

a number of scattering functions, corresponding to several scatterer sizes found in the atmosphere and given proper weighting to fit the logarithmic Junge curve for the size distribution of atmospheric particles, must be chosen. V. Holl[74] has calculated the Mie scattering intensities for m=1.33 and x=.3, .6, 1.0, 2.1, and 3.6. Combining these x parameter values with those of Gumprecht for x=6 and 20, atmospheric particle size distribution curves can easily be approximated. Four size distributions have been chosen:

a. Long and Rensch[13]--experimental polluted atmosphere data;

b. Junge[75]--Zugspitze, Germany--experimental high altitude clear-air aerosol atmosphere data;

c. Junge[75]--Frankfurt, Germany--high pollution experimental atmosphere data;

d. Long and Rensch[13]--continental clear-air aerosol atmosphere model.

The probability of any one x parameter scatterer being present in each of the four cases (a-d) (so that the distribution curve can be approximated) is to be found in Table 3.

Table 3. Probability of x Parameter Scatterer to Simulate Several Atmospheric Distributions.

x	r(microns)	$L_o(x)$	Case a. Prob. $P_a(x)$	Case b. Prob. $P_b(x)$	Case c. Prob. $P_c(x)$	Case d. Prob. $P_d(x)$
0.3	0.033	10^5	0.3500	0.8583	0.4000	0.3700
0.6	0.066	2.5×10^4	0.330	0.1073	0.3900	0.3700
1.0	0.1105	9.0×10^3	0.2400	0.0322	0.1900	0.2300
2.1	0.232	2.04×10^3	0.0400	0.0016	0.0160	0.0200
3.6	0.398	6.94×10^2	0.0180	0.0003	0.0024	0.0080
6.0	0.663	2.50×10^2	0.0115	0.0002	0.0011	0.0015
20.0	2.210	0.225×10^2	0.0105	0.0001	0.0050	0.0050

Columns two and three show the radius corresponding to various x values and the mean distance between scatterings if the scattering medium consisted of only one particular x parameter particles. The earlier calculated values

of $5x10^4<L_o<2x10^5$ m for a clear-air atmosphere and $5x10^3<L_o<5x10^4$ for a polluted atmosphere are thus consistent with the probability distributions calculated here.

Tables of the calculated relative probability that scattered photons will be found within indicated angular scattering ranges are found on the following seven pages. Note that a uniformly polarized source has been assumed; equal weight is given to the Mie scattering intensities i_1 and i_2 in determining the total relative intensity in any one angular scattering range. A table corresponding to the Mie scattering tables can easily be tabulated using the equation $I = I_o(1+\cos^2\theta)$, the characteristic Rayleigh pattern. This table is found on page 103.

Once the relative probabilities for x parameter and angle of scattering have been determined, the simulation is ready for computation. The random number generator is called and the size of scatterer (from among the seven tabulated values) is randomly determined with the predetermined weighting. Similarly, the angle of scattering (from among the 28 ranges tabulated) is randomly determined. The new path length is then found using (99) and the process is repeated until the photon passes the plane z = Z. Before describing the results of the analysis, a number of assumptions should be scrutinized.

First, the assumption has been made that the scattering medium is free of absorption. That is, it had been assumed that a medium is optically thick and, thus, has multiple scattering effects present if R, the optical thickness, is greater than 0.1. However, if absorption is strong, multiple scattering may be insignificant; yet R>0.1.

Table 4. Angular Distribution of Light Intensity Scattered by a Spherical Particle for m=1.33, x=0.3, and $i_1=i_2$.

θ	i_1	i_2	I(weighted)	Prob.=$\frac{I(\#\text{of degrees})}{\Sigma I(\#\text{ of degrees})}$
0	.320x10-4	.320x10-4	.320x10^{-4}	.0089
1	.320	.319	.319	.0089
2	.320	.318	.319	.0089
3	.320	.317	.318	.0088
4	.320	.316	.318	.0088
5	.320	.315	.318	.0088
6	.320	.314	.317	.0088
7	.320	.313	.316	.0088
8	.319	.312	.316	.0088
9	.319	.311	.315	.0088
10	.319	.310	.788	.0200
20	.319	.283	3.010	.0728
30	.318	.239	2.785	.0674
40	.318	.186	2.520	.0611
50	.315	.130	2.225	.0541
60	.314	.078	1.960	.0478
70	.311	.036	1.735	.0425
80	.309	.009	1.590	.0390
90	.307	.000	1.535	.0377
100	.305	.009	1.570	.0386
110	.303	.035	1.690	.0414
120	.300	.075	1.875	.0458
130	.299	.123	2.110	.0514
140	.296	.174	2.350	.0571
150	.296	.222	2.590	.0628
160	.295	.260	2.775	.0672
170	.295	.286	2.905	.0702
180	.294	.294	2.940	.0349

Table 5. Angular Distribution of Light Intensity Scattered by a Spherical Particle for m=1.33, x=0.6, and $i_1=i_2$.

θ	i_1	i_2	I(weighted)	Prob.$=\frac{I(\#\text{ of degrees})}{\Sigma I(\#\text{ of degrees})}$
	$.22\times10^{-2}$	$.22\times10^{-2}$	.22x10	.0086
0	.222	.222	.222	.0086
1	.222	.221	.222	.0086
2	.222	.221	.222	.0086
3	.222	.220	.221	.0086
4	.222	.220	.221	.0086
5	.221	.219	.220	.0085
6	.221	.218	.220	.0085
7	.221	.217	.219	.0085
8	.221	.216	.219	.0085
9	.221	.215	1.090	.0423
10	.220	.195	2.075	.0804
20	.217	.164	1.905	.0738
30	.214	.127	1.705	.0661
40	.210	.089	1.495	.0580
50	.205	.053	1.290	.0500
60	.200	.025	1.125	.0436
70	.195	.007	1.010	.0392
80	.190	.001	0.955	.0370
90	.185	.005	0.950	.0368
100	.180	.020	1.000	.0388
110	.175	.042	1.085	.0421
120	.171	.069	1.200	.0465
130	.168	.097	1.325	.0514
140	.165	.123	1.440	.0558
150	.163	.144	1.535	.0595
160	.162	.158	1.600	.0620
170	.161	.161	0.805	.0312
180				

Table 6. Angular Distribution of Light Intensity Scattered by a Spherical Particle for m=1.33, x=1.0, and $i_1=i_2$.

θ	i_1	i_2	I(weighted)	Prob.$=\frac{I(\#\text{of degrees})}{\Sigma I(\#\text{of degrees})}$
0	.0537	.0537	.0537	.0109
1	.0537	.0536	.0537	.0109
2	.0537	.0534	.0536	.0109
3	.0536	.0532	.0534	.0108
4	.0536	.0530	.0533	.0108
5	.0535	.0528	.0532	.0108
6	.0535	.0526	.0531	.0108
7	.0534	.0524	.0529	.0107
8	.0534	.0522	.0528	.0107
9	.0533	.0520	.0527	.0107
10	.0533	.0518	.2628	.0534
20	.0523	.0466	.4945	.1004
30	.0507	.0388	.4475	.0909
40	.0486	.0295	.3905	.0793
50	.0461	.0202	.3315	.0673
60	.0433	.0120	.2765	.0562
70	.0404	.0056	.2300	.0467
80	.0375	.0016	.1955	.0397
90	.0346	.0001	.1735	.0352
100	.0320	.0006	.1630	.0331
110	.0296	.0028	.1620	.0329
120	.0275	.0061	.1680	.0341
130	.0257	.0098	.1775	.0360
140	.0242	.0136	.1890	.0384
150	.0231	.0169	.2000	.0406
160	.0222	.0194	.2080	.0422
170	.0218	.0210	.2140	.0435
180	.0216	.0216	.1080	.0219

Table 7. Angular Distribution of Light Intensity Scattered by a Spherical Particle for m=1.33, x=2.1, and $i_1=i_2$.

θ	i_1	i_2	I(weighted)	Prob.$=\frac{I(\#\text{ of degrees})}{\Sigma I(\#\text{ of degrees})}$
0	5.4108	5.4108	5.4108	.0222
1	5.4028	5.948	5.3988	.0221
2	5.3928	5.3768	5.3848	.0221
3	5.3808	5.3568	5.3688	.0220
4	5.3068	5.3348	5.3508	.0219
5	5.3508	5.3108	5.3308	.0218
6	5.3328	5.2868	5.3098	.0217
7	5.3128	5.2608	5.2868	.0217
8	5.2908	5.2328	5.2618	.0216
9	5.2668	5.2028	5.2348	.0214
10	5.2461	5.1443	25.976	.1064
20	4.7805	4.4191	45.998	.1884
30	4.0909	3.4271	37.590	.1540
40	3.2831	2.3974	28.403	.1163
50	2.4655	1.5144	19.899	.0815
60	1.7224	0.8675	12.950	.0530
70	1.1131	0.4586	7.859	.0322
80	0.6551	0.2328	4.439	.0182
90	0.3406	0.1216	2.311	.0095
100	0.1490	0.0698	1.094	.0045
110	0.0492	0.0455	0.474	.0019
120	0.0120	0.0356	0.238	.0010
130	0.0125	0.0367	0.246	.0010
140	0.0321	0.0474	0.398	.0016
150	0.0578	0.0649	0.614	.0025
160	0.0812	0.0830	0.821	.0034
170	0.0968	0.0972	0.970	.0040
180	0.1024	0.1024	4.512	.0021

Table 8. Angular Distribution of Light Intensity Scattered by a Spherical Particle for m=1.33, x=3.6, $i_1=i_2$.

θ	i_1	i_2	I(weighted)	Prob.$=\frac{I(\#\text{ of degrees})}{\Sigma I(\#\text{ of degrees})}$
0	112.702	112.702	112.702	.0364
1	111.692	111.502	111.597	.0360
2	110.672	110.302	110.487	.0356
3	109.642	109.102	109.372	.0353
4	108.607	107.902	108.252	.0349
5	107.542	106.702	107.122	.0346
6	106.462	105.502	105.982	.0342
7	105.362	104.302	104.832	.0338
8	104.242	103.102	103.682	.0335
9	103.102	101.902	102.502	.0331
10	102.022	100.760	506.957	.1636
20	76.247	71.689	739.690	.2387
30	43.894	40.117	420.059	.1355
40	19.240	17.490	183.652	.0593
50	5.6204	6.2615	59.409	.0192
60	1.0271	2.4742	17.507	.0056
70	0.8346	1.4725	11.534	.0037
80	1.4236	0.9222	11.729	.0038
90	1.4383	0.4556	9.469	.0030
100	1.0093	0.2615	6.354	.0021
110	0.5715	0.3378	4.548	.0015
120	0.3108	0.5160	4.134	.0013
130	0.2084	0.6738	4.411	.0014
140	0.2576	0.8093	5.335	.0017
150	0.4957	0.9745	7.351	.0024
160	0.8908	1.1798	10.353	.0033
170	1.2732	1.3643	13.213	.0043
180	1.4398	1.4398	7.199	.0023

Table 9. Angular Distribution of Light Intensity Scattered by a Spherical Particle for m=1.33, x=6.0, and $i_1=i_2$.

θ	i_1	i_2	I(weighted)	Prob.$=\frac{I(\#\text{of degrees})}{\Sigma I(\#\text{of degrees})}$
0	1254.	1254.	1254.	0.05898
1	1250.	1250.	1250.	0.05879
2	1239.	1239.	1239.	0.05828
3	1221.	1221.	1221.	0.05743
4	1195.	1195.	1195.	0,05621
5	1164.	1164.	1164.	0.05475
6	1126.	1126.	1126.	0.05296
7	1083.	1083.	1083.	0.05094
8	1034.	1035.	1034.5	0.04866
9	981.9	983.4	982.7	0.04622
10	926.1	928.2	4636.0	0.21805
20	340.1	357.9	3490.0	0.1641
30	43.11	70.05	565.8	0.0266
40	23.86	31.37	276.2	0.0130
50	30.04	26.27	2811.6	0.0132
60	7.044	11.76	94.0	0.0044
70	2.184	5.543	38.64	0.0018
80	7.692	4.136	59.14	0.0028
90	3.453	3.694	35.74	0.0017
100	0.218	2.884	15.51	0.0007
110	4.303	1.801	30.52	0.0014
120	4.104	1.356	27.30	0.0013
130	0.415	1.310	8.63	0.0004
140	3.098	2.013	25.56	0.0012
150	5.973	3.320	46.47	0.0022
160	3.011	3.899	34.55	0.0016
170	2.082	3.677	28.79	0.0014
180	3.506	3.506	17.53	0.0084

Table 10. Angular Distribution of Light Intensity Scattered by a Spherical Particle for m=1.33, x=20.0, and $i_1=i_2$.

θ	i_1	i_2	I(weighted)	Prob.$=\frac{I(\#\text{ of degrees})}{\Sigma I(\#\text{ of degrees})}$
0	48010.	48010.	48010.	.20014
1	46130.	45920.	46025.	.19186
2	40830.	40080.	40455.	.16864
3	33070.	31670.	32370.	.13494
4	24160.	22300.	23230.	.09684
5	15510.	13570.	14540.	.06061
6	8310	6721.	4515.5	.03133
7	3283.	2384.	2833.5	.01181
8	624.4	510.2	567.3	.00236
9	25.42	527.5	276.5	.00155
10	832.8	1596.0	6072.0	.02531
20	405.3	742.9	5471.0	.02393
30	111.1	267.0	1890.5	.07788
40	44.60	265.5	1550.5	.00646
50	24.09	212.6	1183.5	.00494
60	15.69	104.5	601.0	.00250
70	6.469	34.81	206.4	.00086
80	1.437	44.63	230.3	.00096
90	3.575	72.05	378.1	.00158
100	2.714	49.34	260.3	.00109
110	3.964	5.37	46.7	.00019
120	29.00	16.56	227.8	.00095
130	52.25	72.45	623.5	.00260
140	39.79	51.26	455.3	.00189
150	67.71	0.061	338.8	.00141
160	19.23	85.81	525.2	.00219
170	23.14	483.30	2532.2	.01056
180	239.9	239.9	1199.5	.00500

Table 11. Angular Distribution of Intensity Scattered by a Rayleigh Particle, for Which $I=I_o(1+\cos^2\theta)$.

θ		I	R_i	θ		I	R_i	θ		I	R_i
1	180	2.0000	0.0148	31	150	1.7500	0.0130	61	120	1.2500	0.0092
2	179	1.9997	0.0148	32	149	1.7347	0.0128	62	119	1.2350	0.0091
3	178	1.9988	0.0148	33	148	1.7192	0.0127	63	118	1.2204	0.0090
4	177	1.9973	0.0147	34	147	1.7034	0.0126	64	117	1.2061	0.0089
5	176	1.9951	0.0147	35	146	1.6873	0.0125	65	116	1.1922	0.0088
6	175	1.9924	0.0147	36	145	1.6710	0.0123	66	115	1.1786	0.0087
7	174	1.9891	0.0147	37	144	1.6545	0.0122	67	114	1.1654	0.0086
8	173	1.9852	0.0147	38	143	1.6378	0.0121	68	113	1.1527	0.0085
9	172	1.9806	0.0146	39	142	1.6209	0.0120	69	112	1.1404	0.0084
10	171	1.9755	0.0146	40	141	1.6039	0.9118	70	111	1.1284	0.0083
11	170	1.9699	0.0146	41	140	1.5868	0.0117	71	110	1.1170	0.0082
12	169	1.9636	0.0145	42	139	1.5696	0.0116	72	109	1.1060	0.0081
13	168	1.9568	0.0144	43	138	1.5523	0.0115	73	108	1.0955	0.0080
14	167	1.9494	0.0144	44	137	1.5349	0.0113	74	107	1.0855	0.0080
15	166	1.9415	0.0143	45	136	1.5175	0.0112	75	106	1.0760	0.0079
16	165	1.9330	0.0143	46	135	1.5000	0.0111	76	105	1.0670	0.0079
17	164	1.9240	0.0142	47	134	1.4826	0.0110	77	104	1.0585	0.0078
18	163	1.9145	0.0141	48	133	1.4651	0.0108	78	103	1.0506	0.0077
19	162	1.9045	0.0140	49	132	1.4477	0.0107	79	102	1.0432	0.0077
20	161	1.8940	0.0140	50	131	1.4304	0.0106	80	101	1.0364	0.0076
21	160	1.8830	0.0139	51	130	1.4132	0.0104	81	100	1.0302	0.0076
22	159	1.8716	0.0138	52	129	1.3960	0.0103	82	99	1.0245	0.0076
23	158	1.8597	0.0137	53	128	1.3790	0.0102	83	98	1.0194	0.0075
24	157	1.8473	0.0136	54	127	1.3622	0.0101	84	97	1.0149	0.0075
25	156	1.8346	0.0135	55	126	1.3455	0.0099	85	96	1.0109	0.0075
26	155	1.8214	0.0134	56	125	1.3290	0.0098	86	95	1.0080	0.0074
27	154	1.8078	0.0133	57	124	1.3127	0.0097	87	94	1.0049	0.0074
28	153	1.7939	0.0133	58	123	1.2966	0.0096	88	93	1.0027	0.0074
29	152	1.7796	0.0131	59	122	1.2808	0.0095	89	92	1.0012	0.0074
30	151	1.7650	0.0130	60	121	1.2653	0.0094	90	91	1.0003	0.0074

To monitor this effect, define

$$\gamma = \frac{\sigma}{K+\sigma} \tag{105}$$

where

σ = scattering/unit length

K = absorption/unit length.

Thus $0 < \gamma < 1$. For multiple scattering to dominate over absorption effects, γ must be close to one.

Using the continental aerosol distribution model of Long & Rensch[13] results in a value of $\gamma = .98$. This value can also be expected for other size distributions. Thus, if the operating wavelength is not within an atmospheric or pollutant gas absorption line, absorption effects can, in fact, be neglected.

Second, can one assume the index of 1.33 and circular polarization to model the laser radar problem sufficiently closely? Using the data of Engelhard,[76] several runs (a run is defined as following the paths of 2000 simulated photons) with an index of refraction of 1.44 at x=6 were performed. Runs with $i_1 = 4i_2$ comparing the effect of highly polarized light with the $i_1 = i_2$ case were also carried out with x = 6. Other parameters were specifically chosen to place results in a region in which both delay paths and loss of recorded photons by multiple scattering from the recording region were significant. That is--in addition to large particles--a mean distance between scattering less than the range is required before an appreciable number of photons are substantially delayed and yet recorded. Results are shown in Table 13 for the number of delayed photons in various delay length (d_r in m) ranges. For all cases in the Table, a range of 1000 m and recording aperture of 10 x 10m was assumed.

Table 12. Number of Delayed Photons vs. Delay Range for Refractive Index and Polarization Variations.

Delay Range (Meters)	m=1.33 $i_1=i_2$ $L_o=2.5\times10^2$	m=1.33 $i_1=4i_2$ $L_o=2.5\times10^2$	m=1.44 $i_1=i_2$ $L_o=2.5\times10^2$	m=1.33 $i_1=i_2$ $L_o=2.0\times10^3$	m=1.44 $i_1=i_2$ $L_o=2.0\times10^3$	m=1.44 $i_1=i_2$ $L_o=1.0\times10^3$
$0<d_r<.01$	49	44	46	909	888	908
$.01<d_r<.05$	5	3	0	21	3	2
$.05<d_r<0.1$	5	1	0	24	2	6
$0.1<d_r<0.5$	11	1	1	19	5	8
$0.5<d_r<1.0$	9	1	1	31	4	2
$1.0<d_r<10.$	24	3	2	8	8	9
$10.<d_r<\infty$	15	2	4	2	1	1

Note that polarized radiation as well as larger index of refraction affects the number of delayed photons by decreasing their number. Also, approximately the same number of photons was recorded without undergoing scattering (the first delay range). The data from Table 12 are almost identically repeated for other runs initiated with differing random numbers. Thus, the effect of polarization and index larger than 1.33 (at least to 1.5) is negligible on the per cent of photons undergoing no multiple scattering and decreased the number of delayed and subsequently recorded photons.

Using the G-20 for most computations (each run of 2000 photons took from 3 to 75 minutes depending on the per cent of multiple scattering) it was soon discovered that multiple scattering effects in laser radar atmospheric applications cause many more photons to be scattered and lost to the initial pulse than are recorded at the receiving aperture with a substantial delay time. The immediate conclusion is that energy is lost from the beam, but little effect upon coherence is to be expected. One might expect this result, for atmospheric size distributions are heavily weighted toward smaller particles (on the order of λ) with a much smaller

forward scattering contribution. All other Monte-Carlo atmospheric analyses have been concerned with optical propagation through clouds for which the predominance of particles is quite large with a concomitantly large forward scattering component. Thus, of interest in cloud studies is the delay time whereas here the percentage of photons lost from a pulse vs. range is the important parameter.

Several curves of the per cent of photons recorded with a detector aperture equivalent to three different receiver fields-of-view (2, 5, and 25 milliradians) for both polluted and clear-air size distributions are shown in Figures 25 through 29. It should first be noted that altering the size distributions (a through d) has little effect upon the outcome of Figures 25 through 29. Thus, only two distributions were utilized (a and d).

Figure 25 shows that a negligible difference in the number of photons lost to the beam is observed for a wide variation in receiver f.o.v. Given that normal laser radar f.o.v.'s are usually 2 to 5 mr , it is clear that receiver f.o.v. differences will have a negligible effect upon the number of photons lost to the receiver. However, a small effect on the number of photons multiply scattered and subsequently recorded is observed. The numbers just to the right of data points indicate the photons delayed and recorded during any one run (i.e., out of 2000 photons). Only for ranges on the order of the path length does this become appreciable and then only for large receiver f.o.v.'s.

The shorter the wavelength, the more photons delayed and subsequently recorded. In Raman scattering analyses using laser radar, it was earlier pointed out that frequency doubling is utilized to enhance the return. The minimum wavelength one might thus expect in laser radar

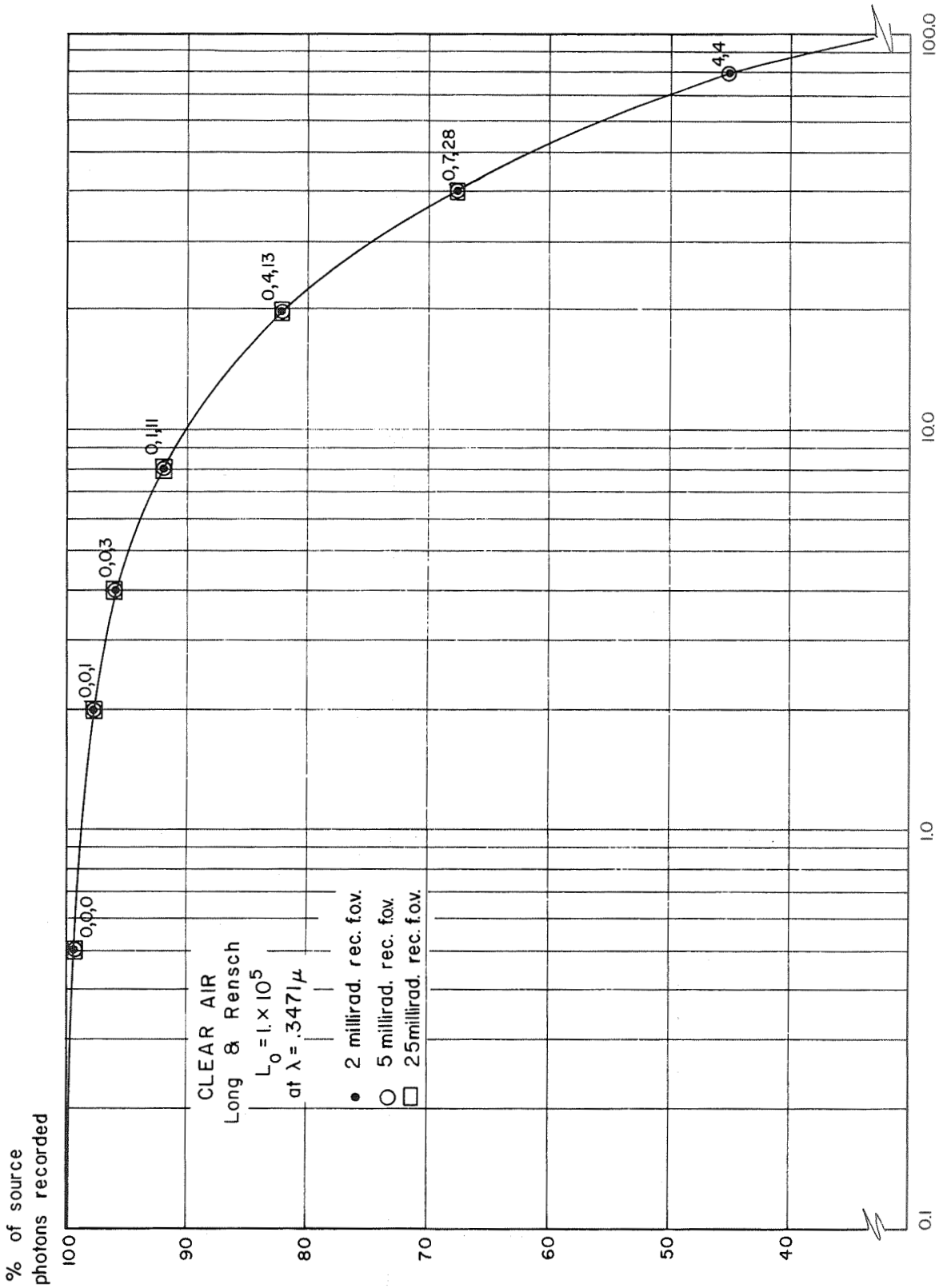

Figure 25. Comparison of per cent photons recorded for a clear air atmosphere (Long and Rensch (d); $L_o = 10^5$ m) at $\lambda = .3471\mu$ for varying receiver f.o.v.

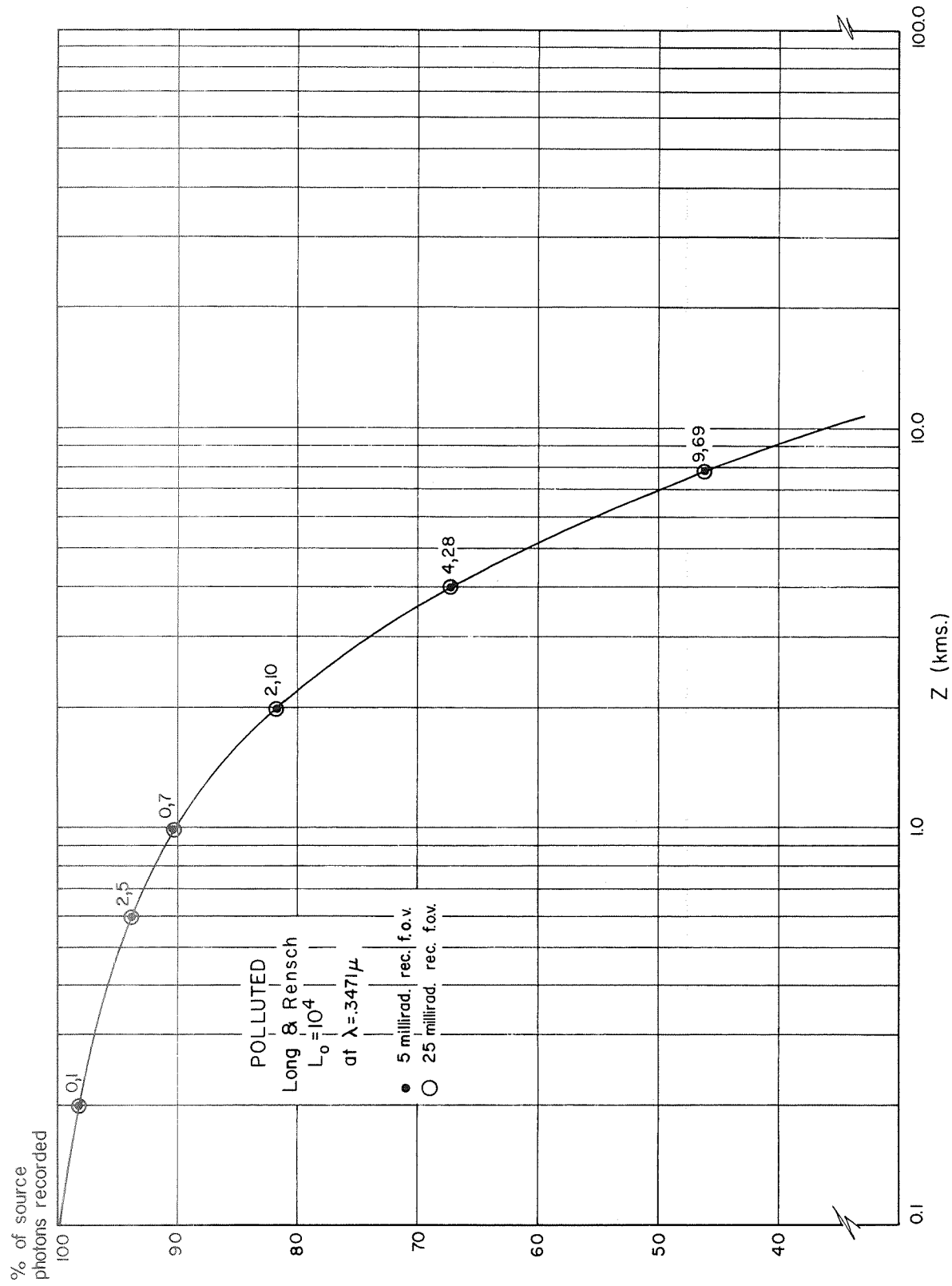

Figure 26. Comparison of per cent photons recorded for a polluted atmosphere (Long and Rensch (a); $L_o = 10^4$) at $\lambda = .3471\mu$ with 5 and 25 mr. receiver f.o.v.

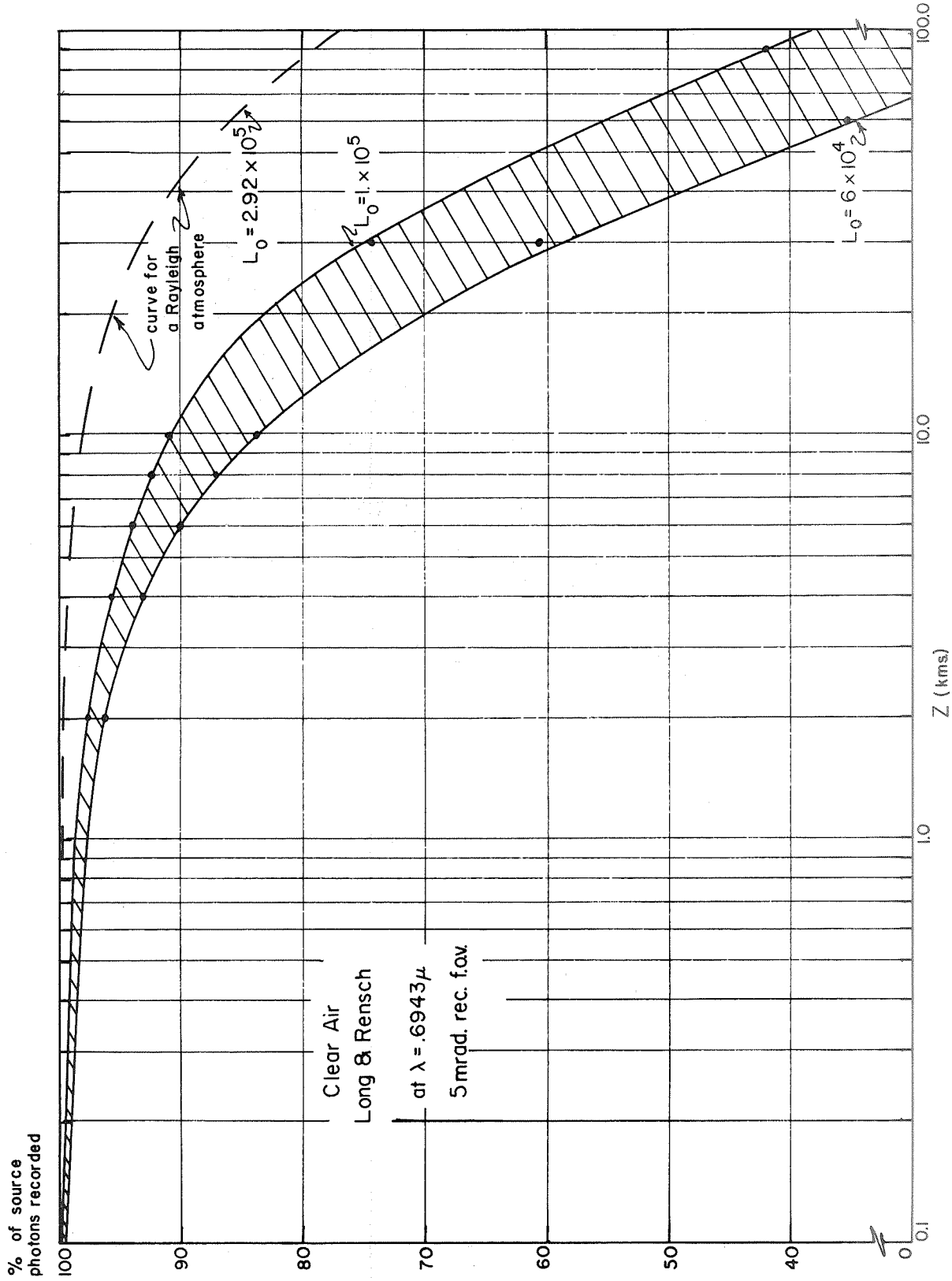

Figure 27. Range of per cent photons recorded for a clear air atmosphere (Long and Rensch (d)) at $\lambda = .6943\mu$ and 5 mr. receiver f.o.v.

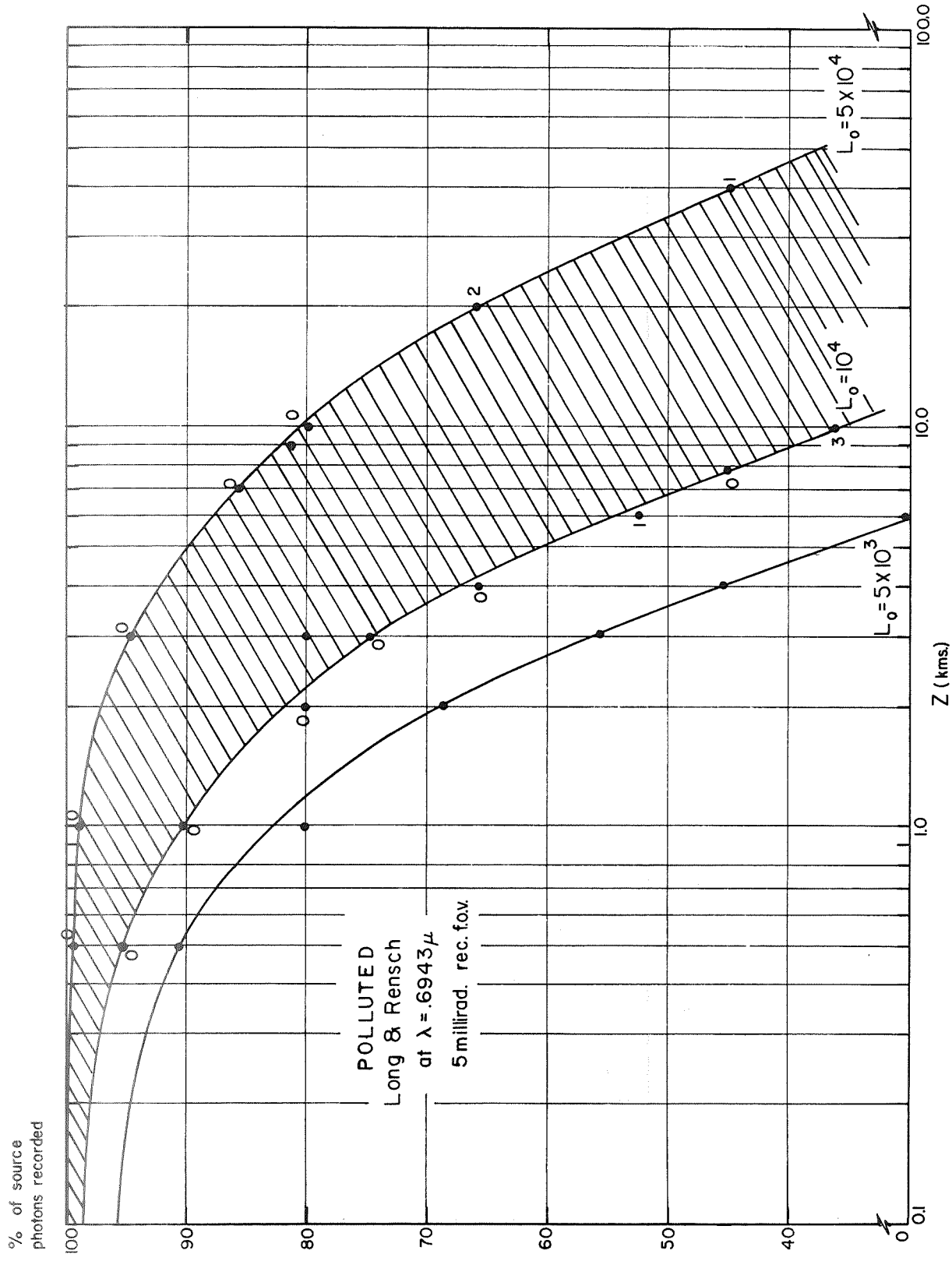

Figure 28. Range of per cent photons recorded for a polluted atmosphere (Long and Rensch (a)) at λ=.6943μ and 5 mr. receiver f.o.v.

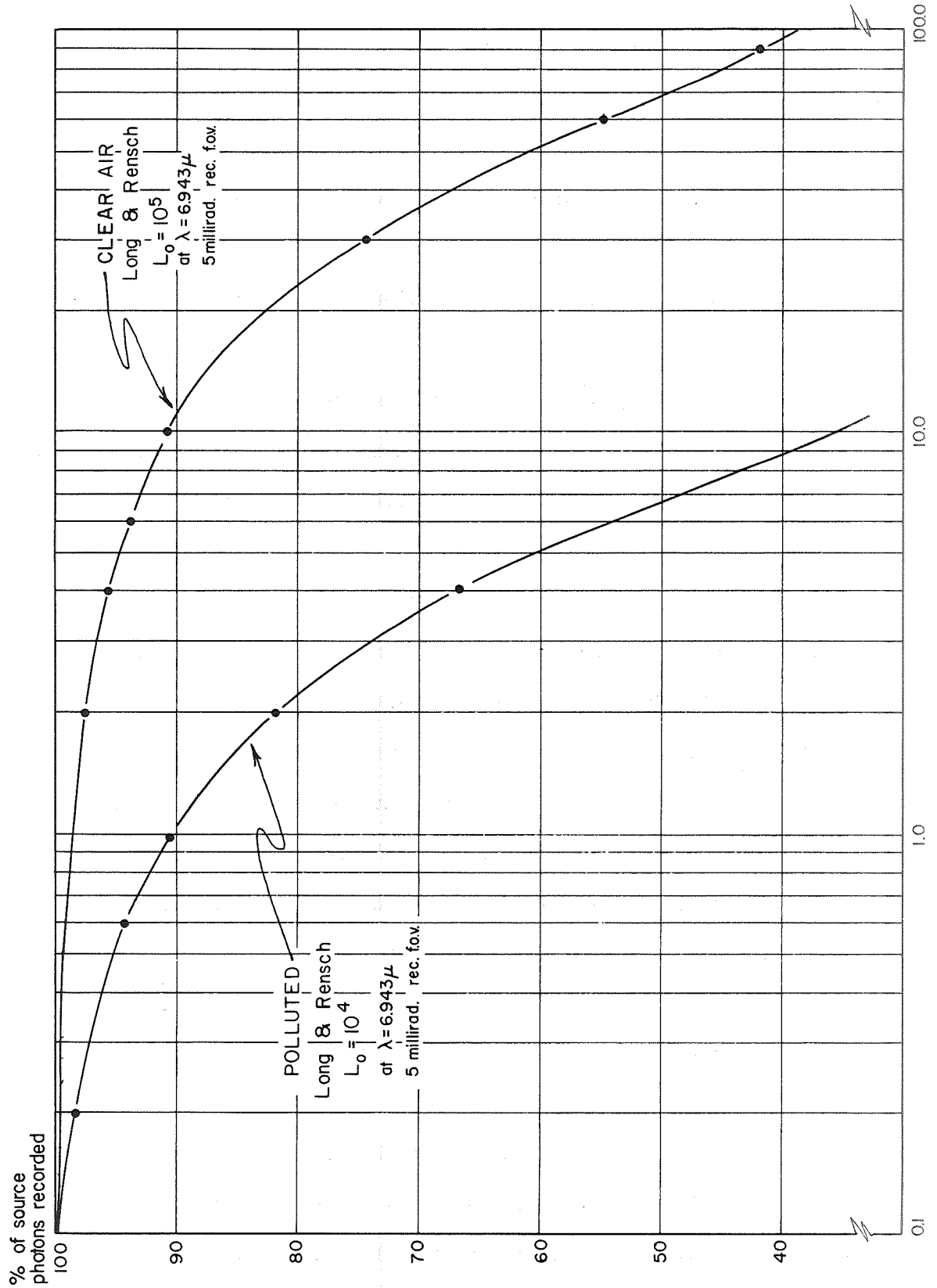

Figure 29. Per cent photons recorded for a polluted atmosphere (Long and Rensch (a)) at $\lambda = .6943\mu$ with a 5 mr. receiver f.o.v.

is .3471μ. The curves in Figures 25 and 26 are at λ=.3471μ. At longer wavelengths (Figures 27, 28, and 29) the number of photons delayed and recorded is never more than .2 per cent of the total number of trials in any one run. Thus, the important conclusion alluded to above, that the per cent of photons lost from a pulse vs. range, is the important effect of multiple scattering.

The data of Figures 25 through 29 also clearly show that across the range of wavelengths .3471 to 6.943 no change in the curves of per cent of photons recorded vs. range can be observed due to source wavelength differences. Thus, for any wavelength used in laser radar (even for pollutant gas absorption measurements) the effects of multiple scattering will be substantially the same.

On the return path (from scattering volume to receiver plane) the same effect on per cent of photons lost to the beam can be expected. As was shown in Figure 25, the small receiver aperture will have a negligible effect on results. Even fewer delayed and subsequently recorded photons will be observed on the return path because of the small receiver aperture. Thus, results for the return path will look almost identical to Figures 25 through 29. In using Figures 25 through 29, if scattering from a range of Z km is being observed, the total path is 2Z and the per cent of photons lost due to multiple scattering is found by subtracting the value on the vertical scale of Figure 27 or 28 at 2Z from 100 per cent.

The cross-hatched areas of Figures 27 and 28 entail most of the important conclusions of multiple scattering effects. Figure 27 indicates that for the mean distance between scatterings varying from 6×10^4 to 1×10^5 meters, the per cent of photons recorded falls within the cross-hatched

area shown. Thus, in a clear atmosphere multiple scattering effects might be neglected to a range of as much as five km. The cross-hatched area of Figure 28 indicates that multiple scattering effects can thus be neglected in a polluted atmosphere only to heights of 1 to 2 km. The curve for $L_o = 5x10^3$ m is for an unusually high pollution atmosphere. For such a case, multiple scattering effects become important for ranges as small as 400 to 600 meters.

Multiple scattering under the conditions of a Rayleigh atmosphere (using Table 12) with $L_o = 2.92x10^5$, a 2 mr receiver f.o.v., and a wavelength of .6943 is shown in Figure 30. The number of photons lost to the beam does not become significant until a range of $2.4x10^4$ m.

Three further points should be noted. First, multiple scattering effects within the scattering volume are, of course, negligible since the longest paths within a typical laser radar scattering volume can be no more than a few meters. Second, the mean distance between scatterings is, of course, not a constant across the entire path. However, by concentrating on the cross-hatched area (variations in L_o lie in the range $6x10^4$ to $1x10^5$ m for a clear atmosphere and 10^4 to $5x10^4$ m for a polluted atmosphere) any variation in L_o is included. For the Rayleigh atmosphere, densities do fall off rapidly with height ($1.85x10^{24}/m^3$ at 20 km vs. $2.55x10^{25}/m^3$ at 0 km). Thus, the falloff of the curve in Figure 30 is more rapid than it should in reality be. However, at ranges greater than 20 km, laser radar, signal levels are several powers of ten below the source power level and are analyzed on a statistical basis and the factor of two or less difference caused by multiple scattering is negligible. Third, the Monte Carlo program is permanently stored on the system B tape of the Electrical Engineering G-20 computer, and thus is available for further computation. Appendix C lists the program and how to call it.

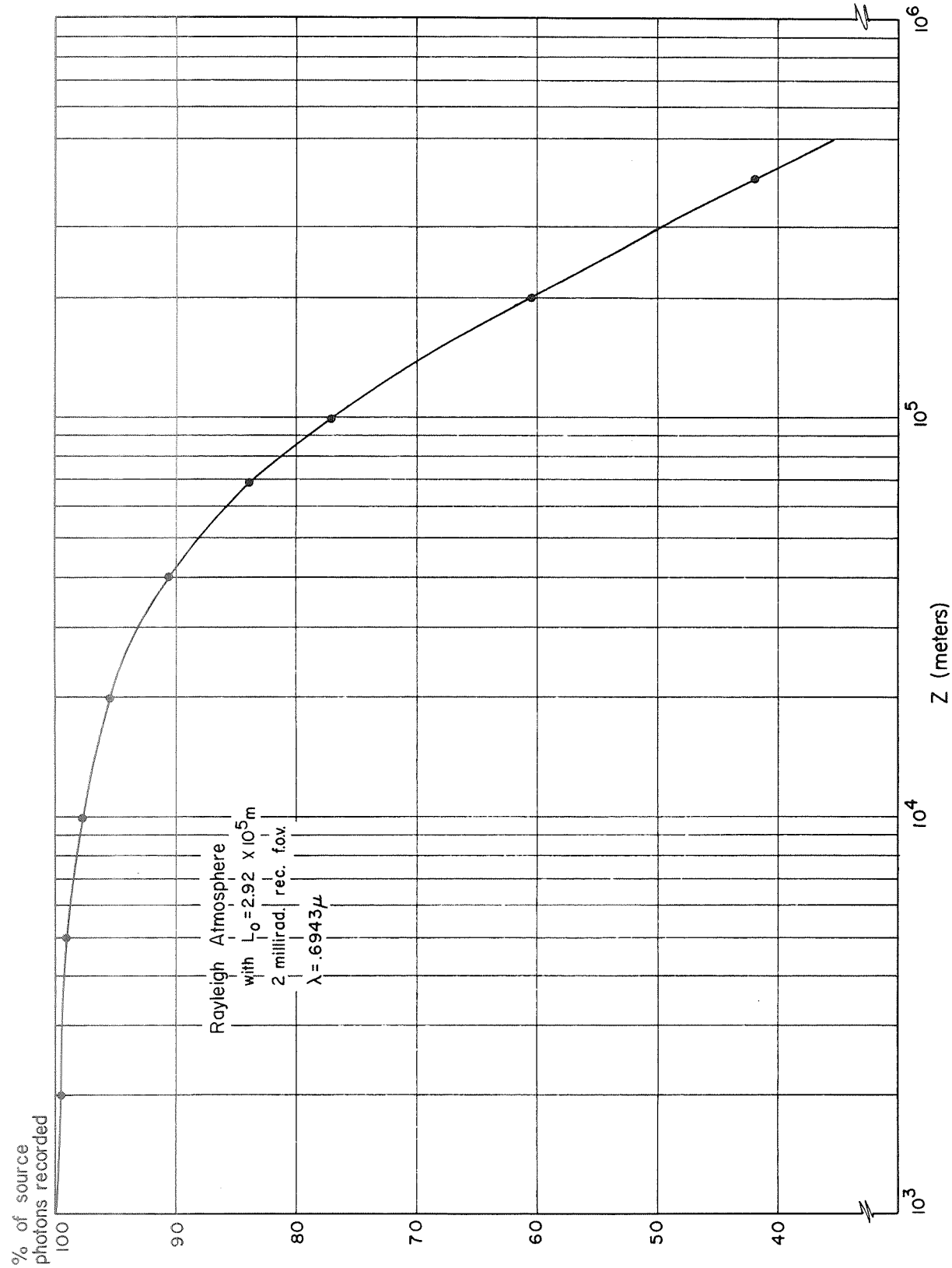

Figure 30. Per cent photons recorded for a Rayleigh atmosphere at λ=.6943μ with a 2 mr. receiver f.o.v.

4.4 Conclusions

What are the implications of these results for the coherence properties? Since pulses are not distorted by multiple scattering to the extent that $\Delta t_M > t_C$ for any significant portion of photons, coherence properties can be expected not to degrade. The saturation term need not be present in (88) for it is now obvious that the laser radar problem is far from any saturation by multiple scattering--either by large numbers of photons being entirely lost to the pulse or by large numbers of photons being delayed and subsequently recorded with time delays greater than the coherence time. Additionally, it has been determined that unless ranges of greater than 2 km in polluted atmospheres and 5 km in clear atmospheres are of interest, multiple scattering effects may be neglected. An important limitation in the use of laser radar results. The use of bistatic laser radar for polarization measurements (alluded to in Chapter 1) may be limited to the lowest (2 to 5 km) atmospheric range. Since multiple scattering may wipe out polarization (at least for short operating wavelengths) in the scattered radiation above this height, polarization properties cannot be used to discriminate Rayleigh scattering by the molecular atmospheric constituents from Mie scattering by aerosols and pollutant particulates.

5. EXPERIMENTAL RESULTS

> A curiosity like mine is decidedly the most pleasurable of vices.--I beg your pardon! I meant to say: the love of truth has its reward in Heaven, and already upon earth.
>
> --Frederick Nietzsche

Discussions with a number of laser radar experimental researchers[77] made it clear early in the investigatory process that field experiments could not be controlled to allow for an assessment of the theory of Chapters 3 and 4. This assessment was, thus, undertaken by means of laboratory experiments.

5.1 Apparatus

The experimental arrangement, shown in Figure 31, consists of the light source, the scattering cell with collecting optics, and the detecting electronics for the experimental analysis to be performed. The light sources used were a 6328 Å HeNe gas laser delivering 5 mW when operating in the TEM_{00} mode, a 6943 Å ruby laser delivering 5 MW in the Q-switched mode, and a Xenon lamp delivering 1 mW after being filtered with a 100 Å filter at 6328 Å.

The polarization of all three sources is or was made vertically polarized (polarization vector perpendicular to the plane of Figure 31). For both lasers, manufacturers claim highly polarized output; the HeNe vertical ($\pm 3°$ off vertical) to one part in 10^3, and the ruby vertical ($\pm 5°$ off vertical) to one part in 10^2. A polarizer was used in conjunction with the Xenon lamp to give a vertically polarized output. In all cases, the beam diameter is reduced to 3 mm at the scattering cell by utilizing a lens with a long focal length.

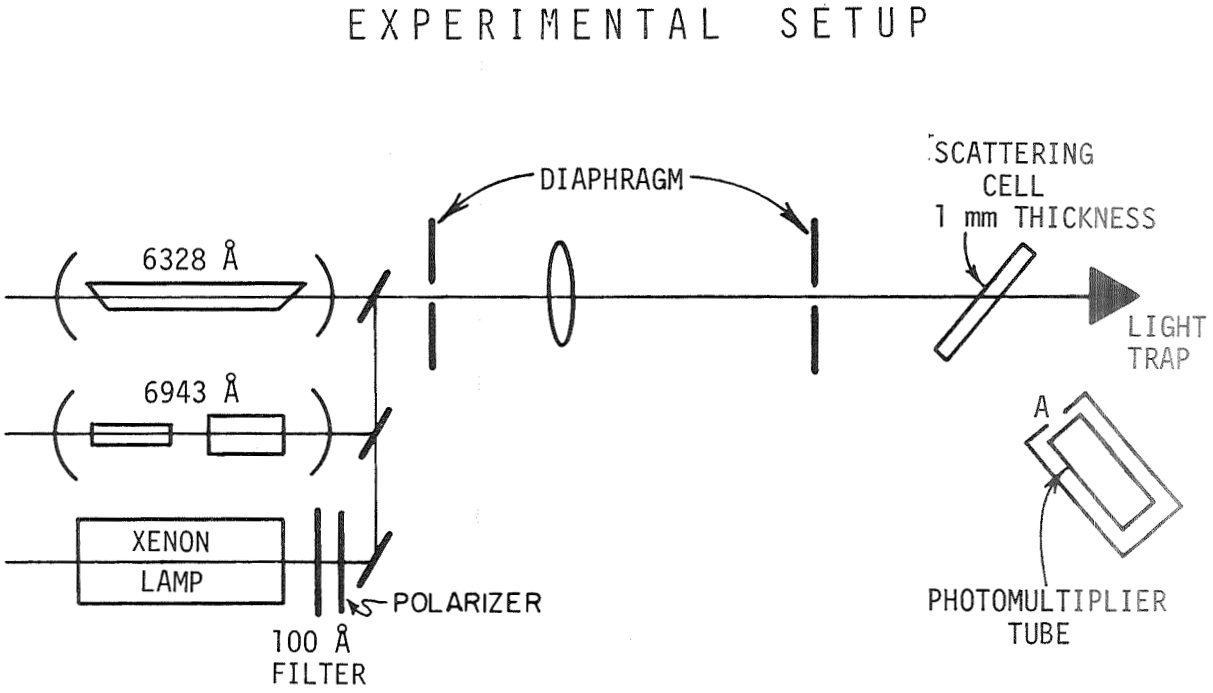

Figure 31. Experimental arrangement for laboratory analysis of theory.

A very thin (1 mm) scattering cell is introduced into the laser beam at the Brewster angle. The cells are made of 2"x2" microscope slides epoxied together with a precision cut 1 mm (accurate to .05 mm) glass wafer. Measurements are performed on dilute solutions of monodisperse polystyrene spherical particles with diameters of .79 and 1.09μ, and index of refraction of 1.592. Each sample is composed of almost equal size particles for the standard deviation is .0054 (Dow Company polystyrene spheres--purchase density, 10 per cent solids by weight). Knowing the scattering cross section and cell depth, the average mutual distance between the polystyrene spheres can be evaluated. Although this turns out to be always larger than a wavelength, as obtained from the manufacturer the sphere concentration is quite high, with an average distance between spheres of $\sim 2.1\lambda$ at a wavelength of .65μ. Unless diluted, multiple scattering will dominate.

The purchased sphere solution was diluted by various factors in order to monitor multiple scattering effects. Factors of 500, 1000, 5000, 10000, 15000, 20000, 30000, 40000, and 60000 were chosen. These dilution factors are equivalent to densities of 18.8, 9.4, 1.88, 0.94, 0.63, 0.47, 0.31, 0.23, 0.16×10^{8} particles/cm^{3}, respectively. The first three were expected to be of low enough dilution to still have multiple scattering present. The dilution medium is deionized water filtered of impurities which might allow Mie scattering. The distilled, deionized water was first filtered with Millipore .22μ filters. Then several filterings with .025μ Millipore filters were undertaken. Thus, only particles of .025μ size or less remain as impurities. Once prepared, the scattering medium within the cell remains uniformly distributed for at least one to two weeks at which time coagulation begins to set in. This is easily

a long enough period for any measurements needed. Of course, several different sets of the 500 to 60000 dilution cells were made and the results correlated.

The intensity of light scattered vs. angle is measured in the plane of incidence (the plane of Figure 31). To evaluate the real scattering angle inside the cell, correction for refraction effects must be taken into account. That is, the observation angle is not the proper scattering angle, since we have an enclosed cell with an air path between cell and detector. Thus,

$$\sin \theta_A = \frac{\sin \theta_o}{n_E} \tag{106}$$

where θ_A is the actual scattering angle, θ_o is the observed scattering angle, and n_E is essentially the index of pure water (1.333).

Minor corrections needed for variations in the solid angle of collection and reflectivity of the cell boundaries at different scattering angles have been considered. These corrections become important only for large emergence angles. The experimental work will be confined to forward and near forward scattering angles, since for large particle diameters, the back reflection of the forward scattered lobe masks the backscattered lobe. Variations in the solid angle of collection can easily be calculated and compensated for. However, cell boundary reflectivity can not. If particular care is not taken, stray light from the edges of the cell and light due to internal reflections could constitute a major contribution to the collected light, particularly at the larger off-axis angles. These spurious contributions are eliminated by an efficient light trap selecting a very narrow solid angle of collection centered on the interaction volume.

The location and arrangement of the diaphragms in Figure 31 was determined so as to eliminate the spurious scattering of light emanating from the source at large angles (important in the ruby laser source case) and yet allow for maximum coupling of light energy to the scattering region (particularly important in the Xenon lamp source case). The design principle is shown in Figure 32.

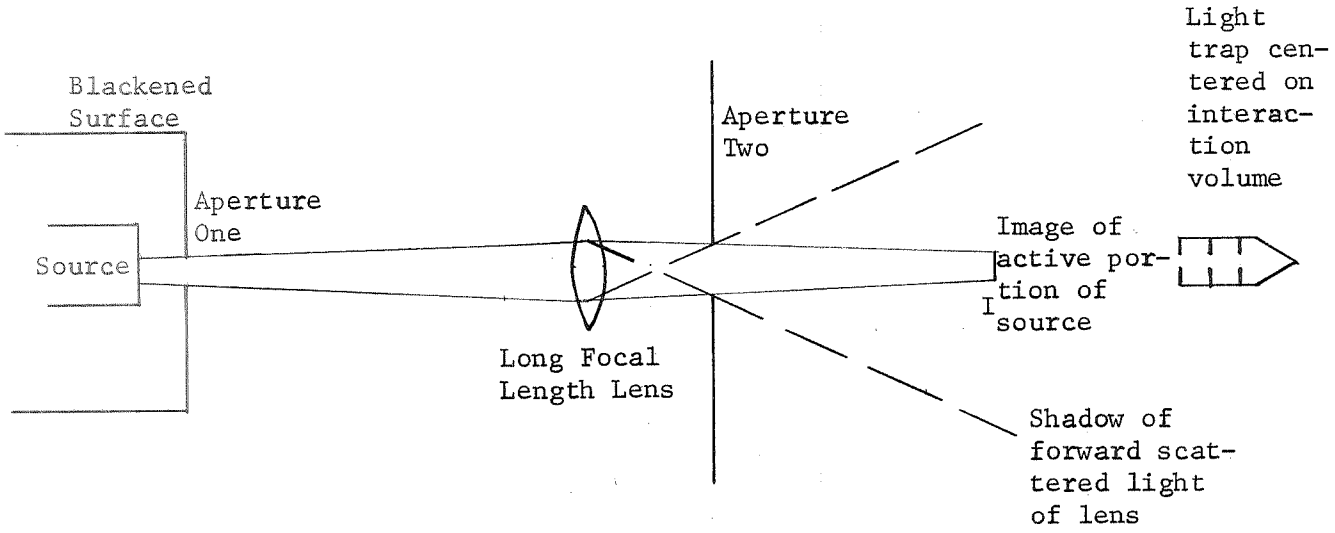

Figure 32. Diagram showing configuration of lens and diaphragms.

Aperture one, placed in front of the source, is used to produce a well-defined beam of light. The beam is incident on a lens having a long focal length, thereby emerging as a slowly converging beam to form a real image of the source at I, the observation region (at which point the scattering cell is placed). This, of course, is the point at which the beam attains its smallest diameter and thereafter diverges. An aperture is placed between the lens and I so that the region of observation is shadowed from forward scattering by the lens. The slowly divergent beam passes on to the narrow angle of collection light trap. Aperture one is really part of a larger blackened surface which encloses the entire source.

Thus no side-light or otherwise reflected light will give rise to light at the observation region.

The detector assembly has been constructed so that an interchangeable aperture located one cm in front of the detector face remains 50 cm from the center of the scattering medium. The detector is enclosed in a light tight blackened container (with described aperture interchangeability) and mounted on a rotating arm with its axis at the center of the scattering region. The entire detector assembly can thus be rotated in the plane of incidence and machined with a tolerance of $\pm$ 1°.

Three different detectors were utilized: a special S-20 surface photodiode (courtesy of Professor J. T. Verdeyen of the Gaseous Electronics Laboratory, who received it from the ITT Corporation of Fort Wayne, Indiana); an S-I surface RCA 7120 10-stage, head-on photomultiplier (P.M.) tube; an S-20 surface RCA 7265 14-stage, head-on photomultiplier tube. Although each was found sufficient for certain of the measurements, the 7265 P.M. proved most versatile and useful. All data shown in the following pages were taken with the 7265 P.M. as detector. A well-regulated power supply with a peak voltage of 10 kV and ripple voltage of 0.1 V was built and used to operate this photomultiplier. The circuit used with the 7265 P.M. tube is shown in Figure 33a. An additional detector, used to monitor the direct output of the sources as well as to trigger the scattered light detection oscilloscope, was utilized. This detector consists of an SGO-100 photodiode with appropriate circuitry as shown in Figure 33b. Compensation for variations in source power as monitored by the photodiode can thus be afforded.

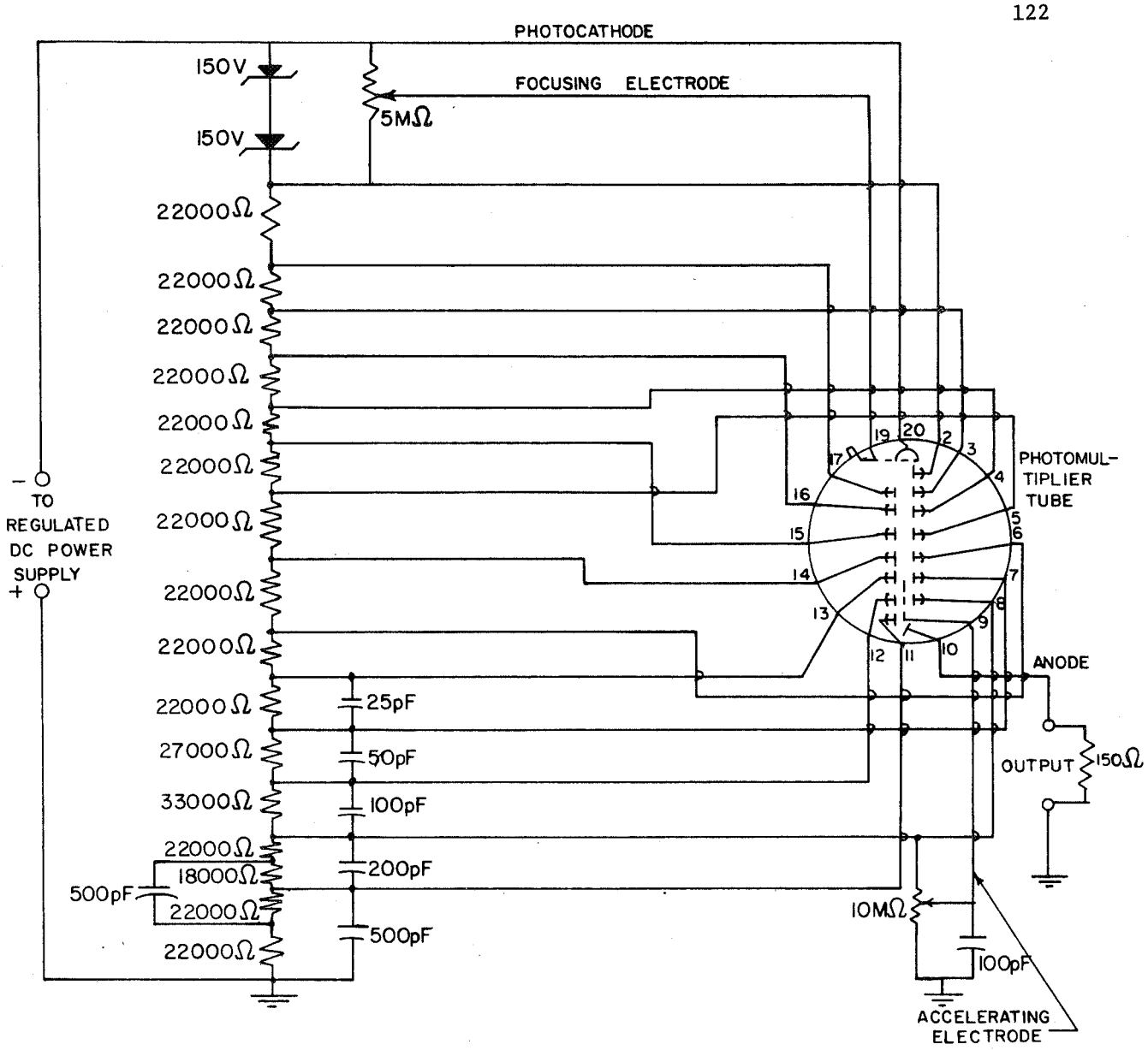

a. Photomultiplier tube circuitry.

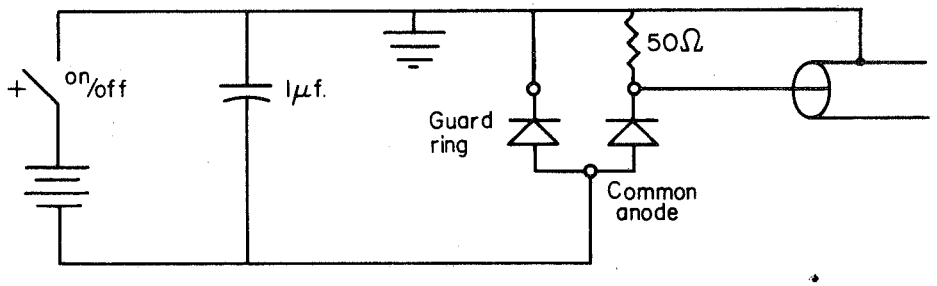

b. SGD-100 photodiode circuitry.

Figure 33. Detector circuitry.

5.2 Measurements

Several different kinds of measurements might be expected using this apparatus. Among them are

(a) angular intensity distributions,

(b) intensity fluctuations as a function of detector aperture size to correlate with results of the coherence cell analysis,

(c) effect of CW HeNe and pulsed ruby laser coherence properties on dependent scattering intensity vs. independent scattering of incoherent Xenon lamp,

(d) possible multiple scattering effects on ruby laser pulse spreading and multiple scattering data to correlate with the results of the Monte-Carlo analysis.

Fluctuations in the signal detected will arise due to Brownian motion of the dispersed particles. In the theory of Brownian motion the velocity $\bar{v}$ of the center-of-mass of the particle obeys a Langevin equation

$$\frac{d\bar{v}}{dt} + \beta\bar{v} = \bar{F}(t) \tag{107}$$

where $\bar{F}(t)$ is the viscous force per unit mass,

β is the friction constant divided by the mass m of the particle, given by the Stokes formula $\beta = 6\,a\eta/m$ where a is the radius of the particle and η the viscosity coefficient of the water.

For a sphere whose radius, a, is much greater than the mean free path of particles in the medium (i.e., the path traveled before the particle collides with a molecule of the medium) the distance traveled by a particle under Brownian motion in time t is

$$\overline{x^2} = \frac{kT}{3\pi a\eta}\, t \qquad (108)$$

where k is the Boltzmann constant and T is the ambient temperature. For a distance of travel on the order of 10 wavelengths, t is on the order of .1 ms. Thus, an entirely new ensemble configuration is present within the scattering volume approximately every .1 ms. If the detector aperture is small enough to accommodate only a few or less coherence cells, fluctuations in the output signal versus time should be recorded. This assumes a dependent scattering process and negligible fluctuation in source light intensity.

Variations in source intensity were monitored by the SGD-100 photodiode. As might be expected, negligible variations in the HeNe laser and Xenon lamp were observed. However, five per cent variations in the Q-switched ruby signal level were regularly observed. Thus, in all measurements, the ruby laser output was monitored by the SGD-100 photodiode and compensation made for signal variations. An initial experiment to carefully monitor the power output of the Q-switched ruby was performed using a Korad calorimeter followed by a microvolt ammeter and XY recorder. During this early experimentation the delay time (between laser flashlamp firing and Q-switching) to obtain an optimal pulse was also determined. With a 1.43 ms delay a clean 200 ns Q-switched pulse was obtained as shown in Figure 34. This pulse was used throughout the experimental

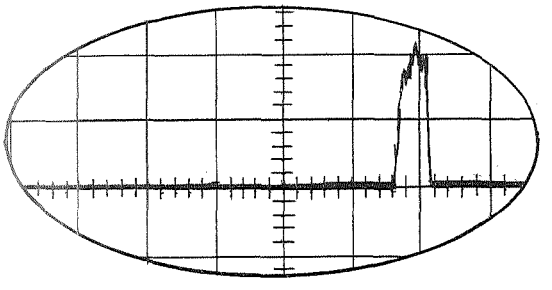

vertical scale = 2 v/div
horiz. scale = .5 μs/div
flashlamp voltage = 1.3 Kv
1.43 ms Q-delay

Figure 34. Ruby laser Q-switched output.

period. Figure 35 shows results of calorimeter power measurements on 200 ns pulses and the fluctuation therein. Depending on the flashlamp voltage, energies from .1 to .6 joules can be achieved. Fluctuations in power level (shown by the bars in Figure 35) vary from two per cent to 11 per cent. For most cases a five per cent fluctuation can be expected. It should be mentioned that a careful timing procedure was required to maintain fluctuations at five per cent or less. Because the ruby laser was air cooled, a ten-minute down time between pulses was adhered to; otherwise, the threshold voltage rises (normally at 1.05 Kv) and wide fluctuations in power levels result.

A study of the coherence properties of the HeNe and pulsed ruby laser sources was performed using a standard Michelson setup (being careful to maintain spatial coherence as the light progresses through the optical system). Since the Michelson interferometer is itself a cavity, coupling between the Michelson and laser cavities must be avoided or an erroneous coherence measurement may result. As described by Erickson and Brown[51] and alluded to on page 68, the fringe visibility in the Michelson experiment should have a periodicity of twice the laser cavity length. Note that this is the effective cavity length taking into account the $n \neq 1$ media within the cavity such as the ruby rod and Q-switching medium in the case of the ruby laser. This was, in fact, observed for both the HeNe and Q-switched ruby cases. The source beam was also spread with a diverging lens and split off to the separate arms of the interferometer with no fringe visibility degradation. Thus, on a qualitative level, transverse coherence across the source beam for both the HeNe and Q-switched ruby cases is quite good. However, for the non-Q ruby no periodicity was observed. This is due to the non-stationarity

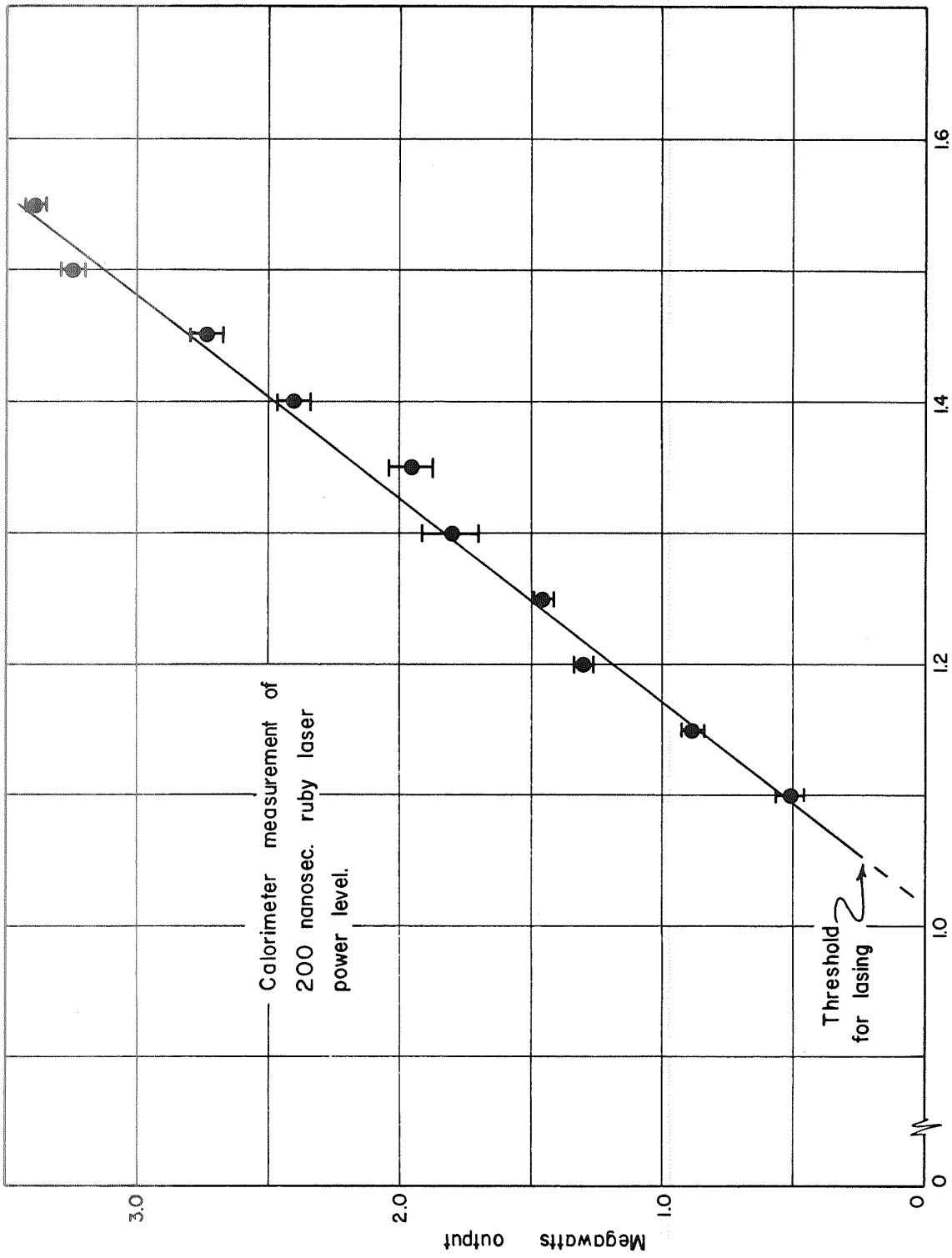

Figure 35. Ruby laser Q-switched power measurement vs. flashlamp voltage.

of mode lines in the frequency spectra output of the non-Q ruby laser. With the much longer time length of the non-Q vs. Q-switched case, mode hopping occurs with a resultant smearing of the periodicity in fringe visibility.

Results of the fringe visibility measurement are only qualitative. Improvements in the experiment might be made such as the use of a faster film (Polaroid Type 47 with A.S.A. 3000 was used). However, the essential point has been made. For the small experimental scattering volume (3 mm diameter and 1 mm depth) phase-angle relationships prevail among individual particles due to the coherence properties of the HeNe and Q-switched ruby laser sources. Thus, dependent scattering can be assumed and its effect measured in the scattered light.

A further point should be made regarding the small scattering volume size. Discrepancies between experimental results and the plane-wave approach to the scattering can be expected when the escape time of the particles from the scattering volume is smaller than the characteristic relaxation time for the momentum of the particles, defined as the average time interval which elapses before collisions make a particle forget its initial velocity. Does the plane-wave approach apply to the small scattering volume described in the previous paragraph? The escape time of a particle from the scattering volume can be determined from (108). Since the escape distance is on the order of 1 mm, the escape time

$$t_e = \frac{3\pi a \eta}{kT} \overline{x_v^2} \tag{109}$$

is on the order of .5 sec for a scatterer in water of diameter 1 micron.

The average time interval which elapses before collisions with molecules of water make a particle forget its initial velocity is given by[78]

$$t_c = 1/\beta = m/6a\eta. \qquad (110)$$

t_c, for the problem at hand, is on the order of 10^{-10} sec. Since the escape time of particles from the scattering volume is much greater than the characteristic relaxation time for the momentum of the particles, the plane-wave theory applies in spite of the small diameter of the incident beam.

Minor problems with electronic noise of various sorts and sources were experienced early in the experimentation but were overcome one by one.

5.2.1 Angular Distributions

Using a slow detector response time (i.e., a response time greater than the time it takes particles to form a new ensemble through Brownian motion, approximately .1 ms) and a detector aperture of 2000 microns radius (equivalent to 40 to 45 coherence cells for the range and wavelength of operation), a time average on and incoherent detection of the scattered intensity can be achieved. An angular intensity distribution for the scattered light with the HeNe laser as source can thus be obtained. As long as densities are kept low enough so that multiple scattering effects are not important, the angular distribution is expressed in terms of the single-particle Mie scattering theory. For a given angle, θ, the intensity of the scattered light depends on two parameters, x and n_e, where $x = 2\pi a/\lambda$, the characteristic Mie parameter used earlier, and n_e is the relative index of refraction (1.199 for polystyrene in water).

The output photocurrent was fed to an X-Y recorder through a low-pass filter. The results are shown in Figures 36 and 37 for .79 and 1.09μ particles, respectively. The experimental points agree quite well with the theoretical curves[79] (solid lines) for Mie scattering of vertically polarized light (thus referencing the i_2 table values) with x=4.0 and 5.5 and n_e=1.2. The actual x and n_e parameters being x=3.93 and 5.42 and n_e=1.199, there should be expected a very close fit of theoretical and experimental data. The dispersion of the experimental data is less than five per cent for all measurements. The size of the error bar associated with each experimental point corresponds to the maximum dispersion during four runs.

In the ruby laser case, with a 200 ns pulse length, particles will undergo Brownian motion of no more than 5 to 10 Å during the pulse. Thus, no time averaging takes place but rather a new ensemble configuration of fixed particles presents itself to each Q-pulse. Dependent scattering should then be present. However, as long as the spatial averaging of the large detector aperture (equivalent to many coherence cells) is maintained, dependent scattering effects should not be detected. The results shown in Figures 38 and 39, again for .79 and 1.09μ diameter particles, show that no dependent effects are present. Indeed, the data points closely follow theoretical curves[79] for x=3.5 and 5.0 and n_e=1.2. Since the actual x and n_e parameters are x=3.58 and 4.93 and n_e=1.199, the close fit is to be expected. Note that the theoretical curves in Figures 36 through 39 are all plots of the vertically polarized (i_2) Mie theory intensity since the sources are vertically polarized.

Data for the Xenon lamp with a polarizer and 100 Å filter centered at the HeNe laser wavelength are shown as dotted curves in Figures 36

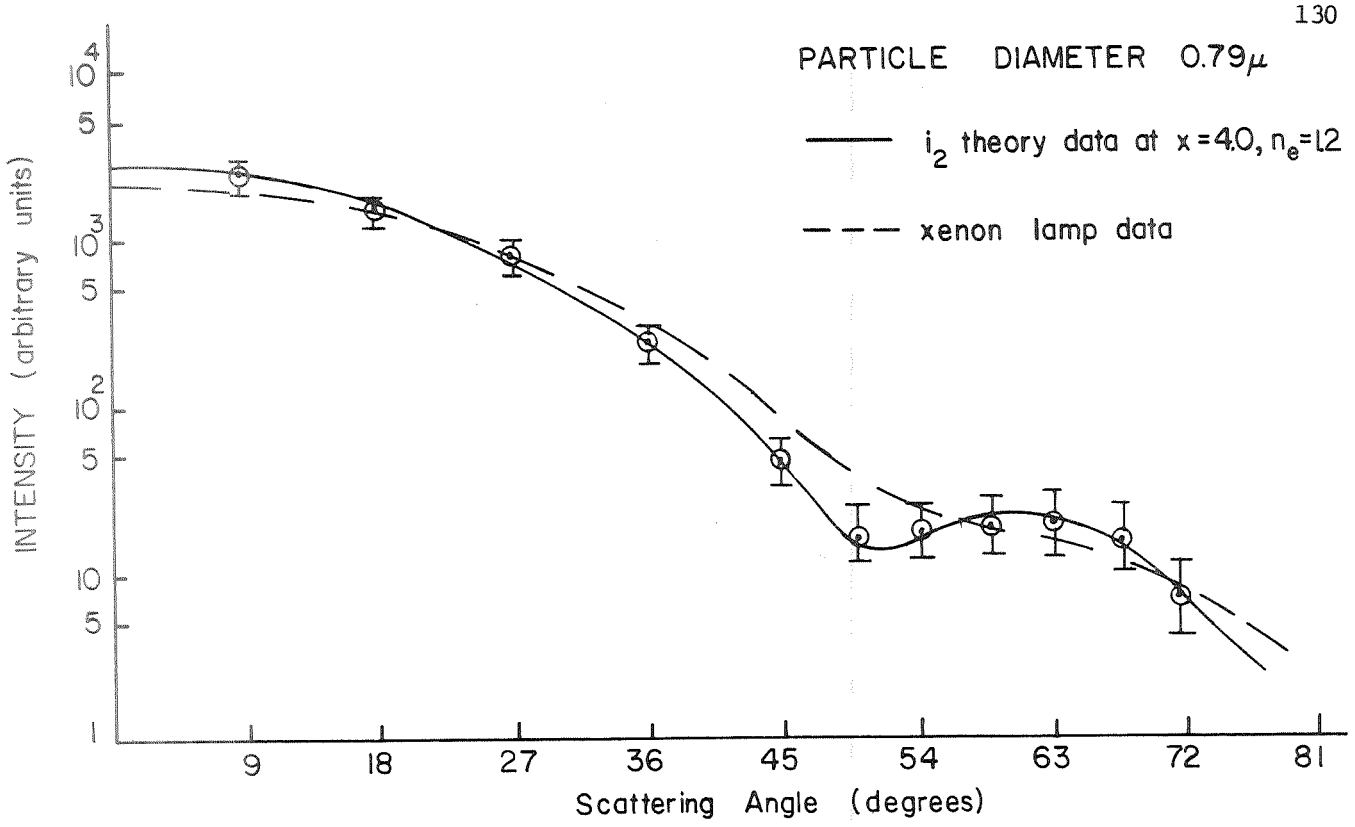

Figure 36. Angular scattering for 0.79μ diameter particles, HeNe laser and Xenon lamp as sources.

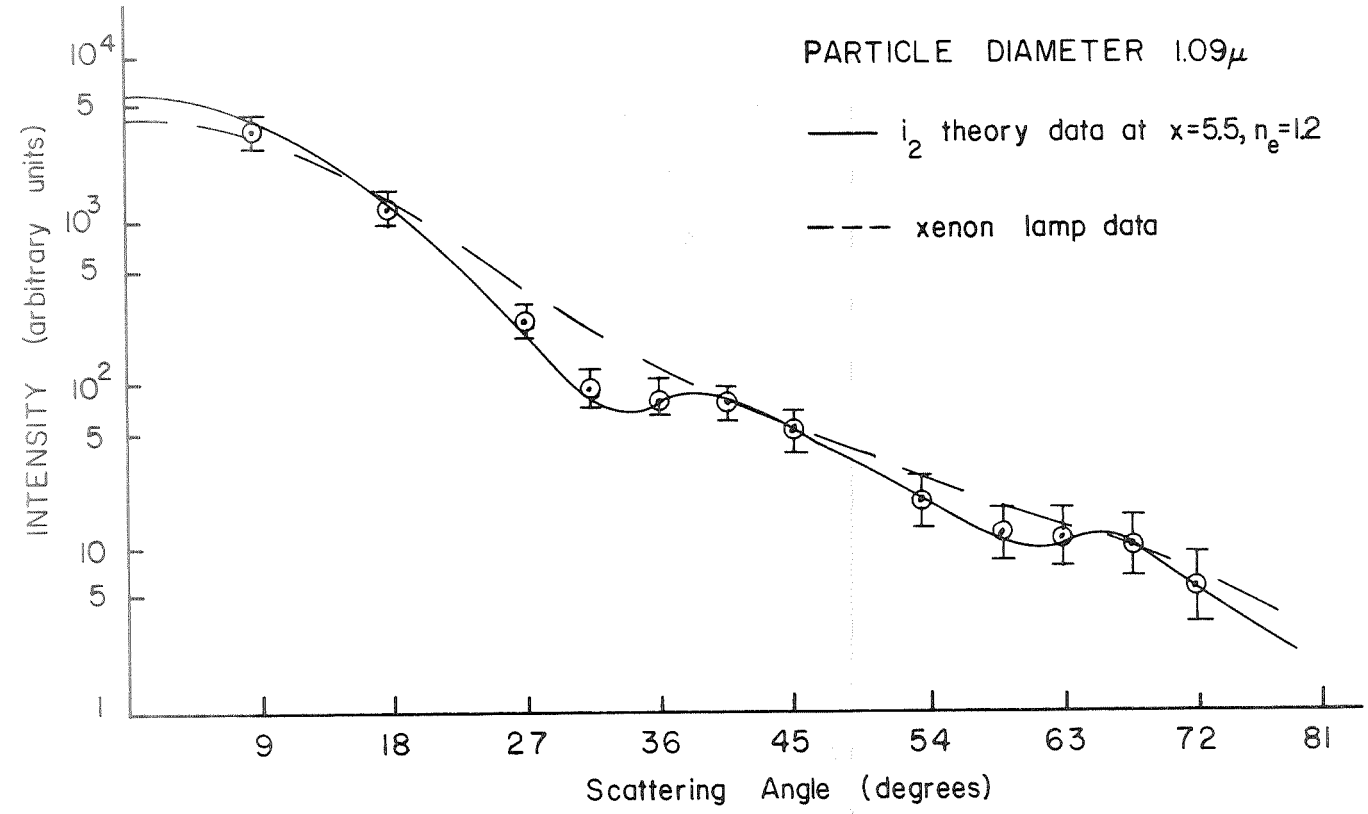

Figure 37. Angular scattering for 1.09μ diameter particles, HeNe laser and Xenon lamp as sources.

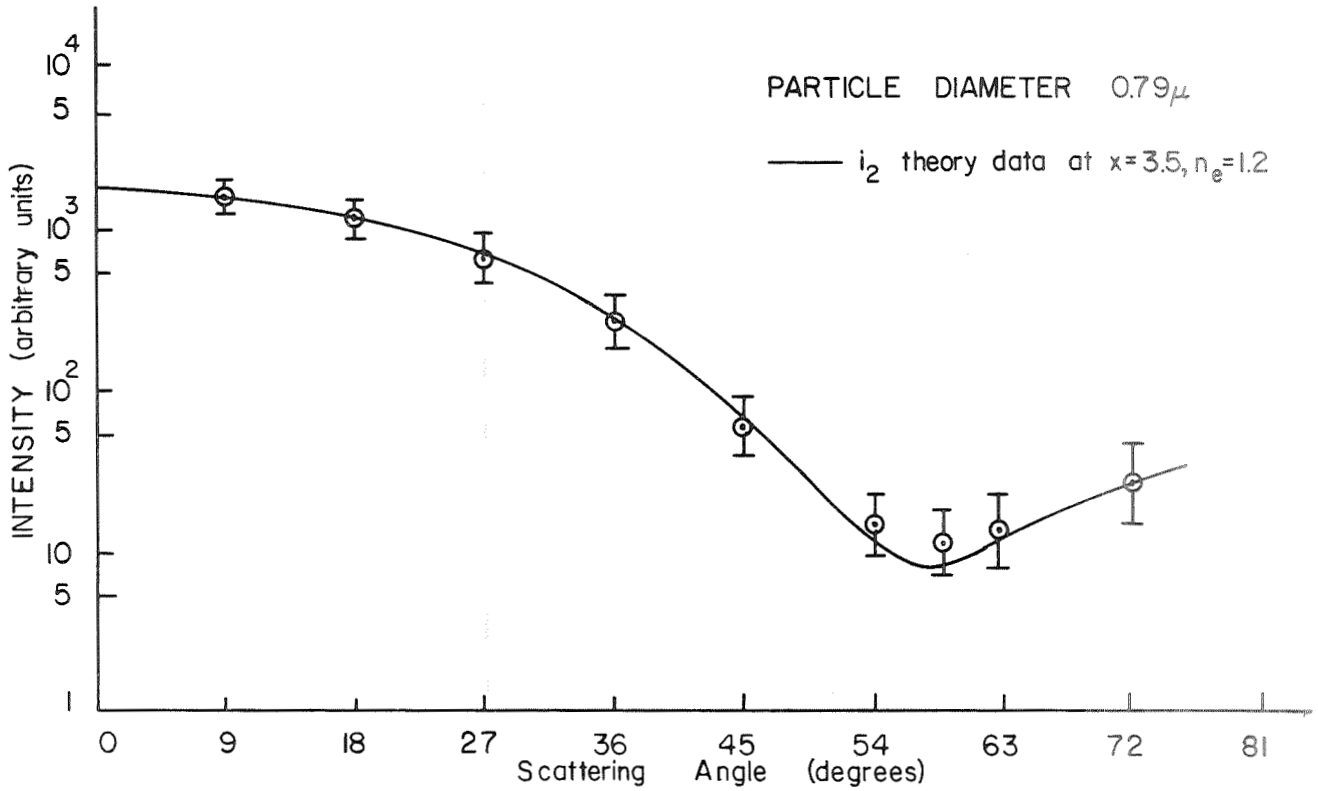

Figure 38. Angular scattering for 0.79μ diameter particles, ruby laser as source.

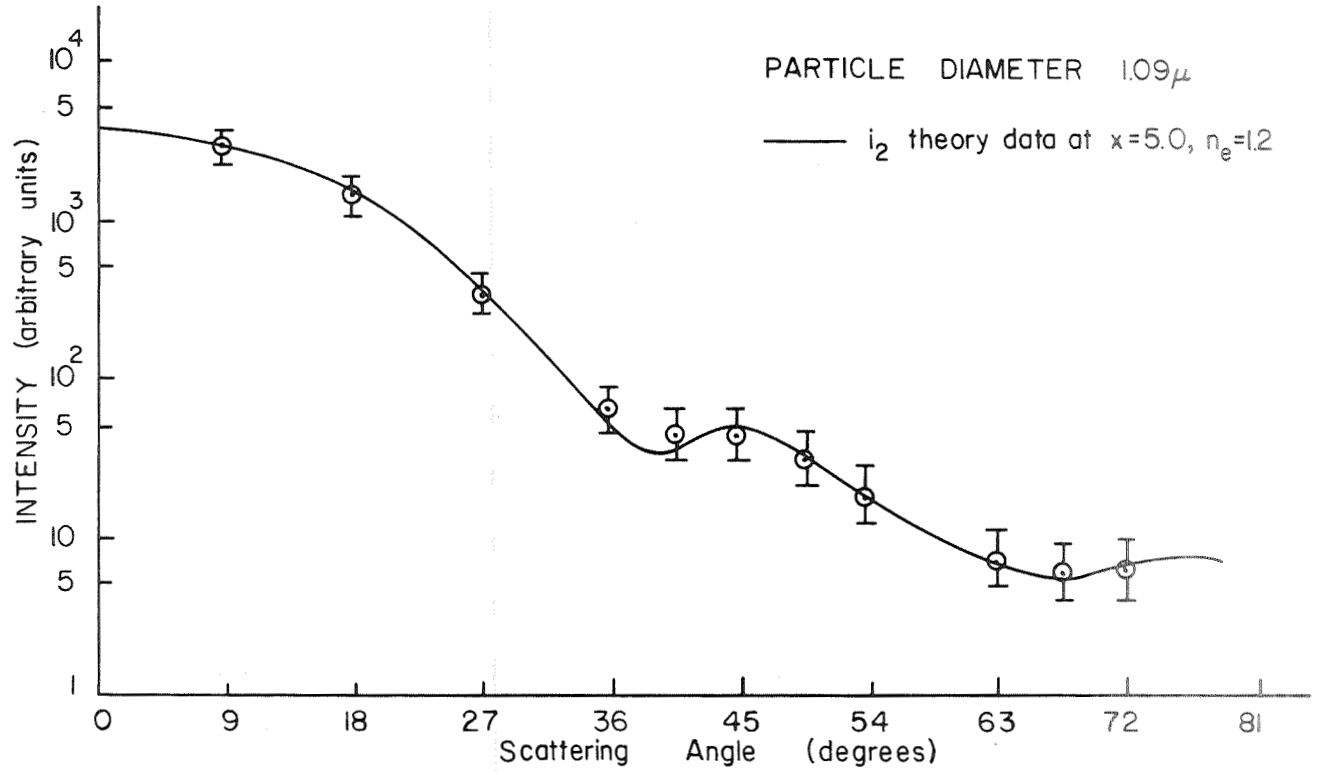

Figure 39. Angular scattering for 1.09μ diameter particles, ruby laser as source.

and 37. Because a broad spectrum source is used, the peaks and valleys do not show as for the much narrower spectrum data of the HeNe laser.

Given that the sources are not completely polarized, that a flattening of the fluctuations due to the variance in size of the scattering particles was expected, and the normal error and noise contributions of the experimental apparatus, the results of Figures 36 through 39 are exceptionally good. Indeed, it shows the measurement scheme to be operating very well, thus allowing confidence as the more interesting coherence property measurements are undertaken.

5.2.2 Spatial Detection and Dependent Scattering Effects

Consider an experimental setup in which a fast detector response time (i.e., a response time less than the time it takes particles to form a new ensemble through Brownian motion) and a detector aperture which varies from that equivalent to many coherence cells to that equivalent to less than one coherence cell utilized. Spatial detection effects as described in section 3.2 ought then to become more dominant the smaller the detector aperture. Further, with an aperture smaller than one coherence cell the dependent scattering effects described in section 3.3 can be monitored by varying the scatterer density.

Experimental evidence to verify the spatial detection effects theory was obtained with both the HeNe laser and Q-switched ruby laser as the source using an overall detector/electronics response time of 7 ns. Figure 40 shows the data obtained. In the case of the HeNe laser, fluctuations were monitored by plotting the detector signal level vs. time on a strip-chart recorder. For the Q-switched ruby laser 20 sample signal levels were recorded to determine an appropriate fluctuation percentage. In no case was the per cent of fluctuation a function of

angle of scattering or density of scatterers. Results for the Xenon lamp case show that no matter what the aperture, the per cent of fluctuation in signal level is never more than the background system noise fluctuations.

The curves of Figure 40 for both the HeNe and Q-switched ruby laser cases are very similar with 100 per cent fluctuation observed to apertures of 100μ diameter and a decrease in the fluctuation percentage to the noise level at aperture diameters of 6000 to 8000 μ. These curves are in qualitative agreement with the results of section 3.2 as expressed in Figure 18. The upper scale of Figure 40 indicates the number of calculated coherence cells at $\lambda = .66\mu$, a range of 50 cm and an aperture corresponding to the lower scale. Quantitatively, the experimental curves seem to experience signal fluctuations less than 100 per cent at too small an aperture diameter and yet also experience too large fluctuations at aperture diameters equal to or greater than 1000 μ. The dashed curve of Figure 40 would more closely match the theoretical curve of Figure 18. Since the experimental data mismatch the theoretical data in a dichotomous way, the error cannot be labeled as a consistent system error. No explanation for this discrepancy has been forthcoming. Suffice it to say, then, a qualitative verification of the spatial detection effects theory has been garnered from the data of Figure 40.

What of the N^2 dependent scattering effects? Using (91), and noting the experimental scattering volume to consist of but one spherical aggregate (i.e., entirely dependent scattering), the maximum ratio of dependent to independent scattering for a=1mm and m=1 is

$$R_{max.} = 0.275 \times 10^{-8} N. \qquad (112)$$

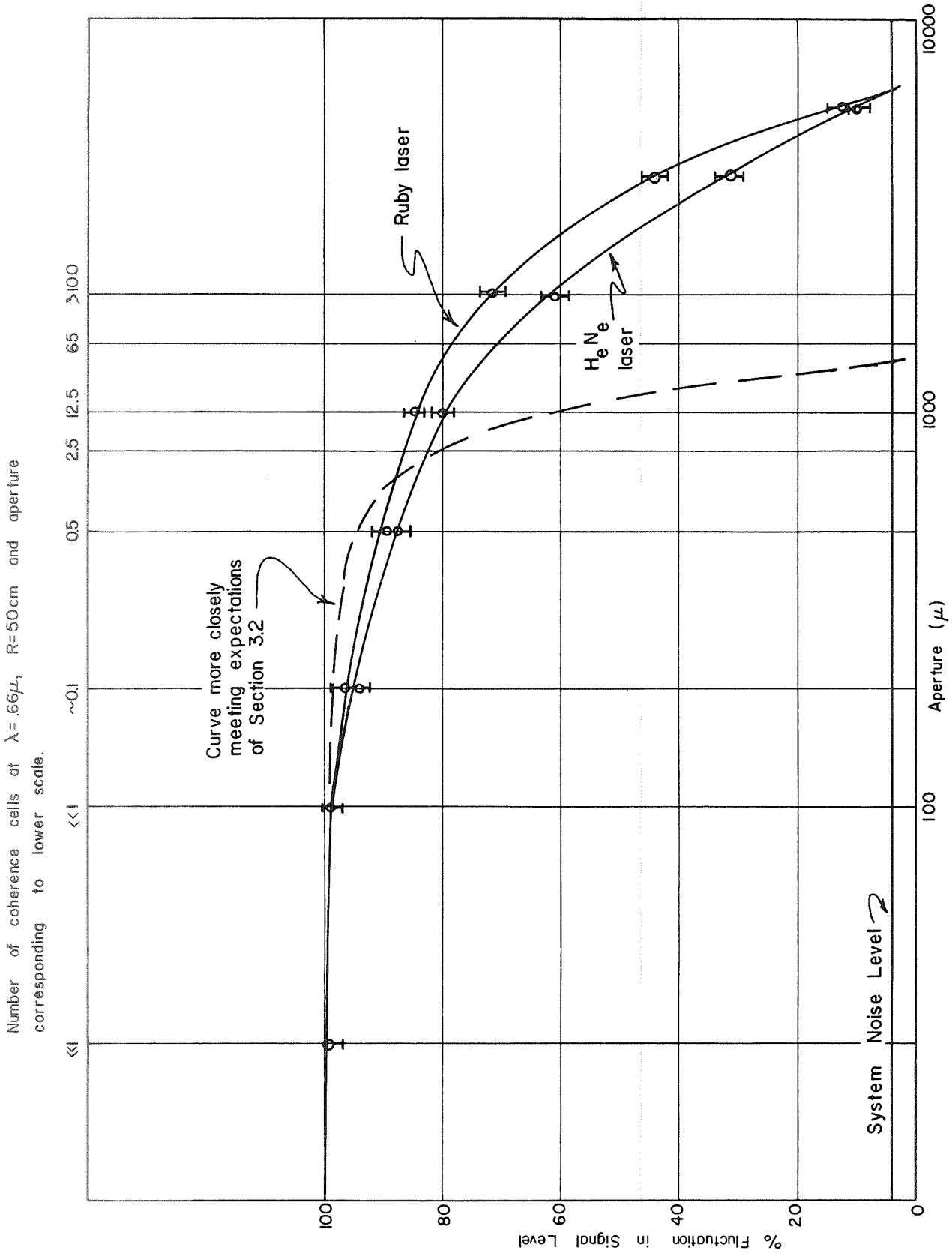

Figure 40. Detector intensity fluctuation due to spatial detection effects.

For the experimental densities used (described in section 5.1) the number of scatterers in the scattering volume of approximately 4 mm^3 varies from 6.4×10^4 for the lowest density (dilution factor of 60000) to 7.5×10^6 for the highest density (dilution factor of 500). Thus, the maximum ratio of dependent to independent scattering for the experimental setup is

$$1.76\ 10^{-4} < R_{max.} < 2.06 \times 10^{-2}. \qquad (113)$$

Because of the conditions imposed by the experiment, the dependent scattering contribution should in all instances be negligible in comparison to the independent scattering contribution. This was, in fact, observed. As the scattering cell density was increased (from 0.16×10^8 to 1.88×10^8) a linear increase (i.e., an N or independent scattering intensity) in detected signal is recorded. However, upon utilizing the two highest density cells a leveling off in signal intensity is recorded.

Figure 41 shows this effect pictorially. Almost identical curves were obtained regardless of the scattering angle of observation; that is, a linearity in the increase of scattered intensity vs. density of scatterers with a saturation effect at the two highest densities was observed in every case. Thus, the multiple scattering effect explored in Chapter 4 manifests itself rather than the dependent scattering effect of section 3.3. The linearity of low scatterer density data verifies that independent scattering predominates over dependent scattering as indicated in (113).

Figure 41, along with observation of no pulse spreading at the highest scatterer density, provides verification of the multiple scattering

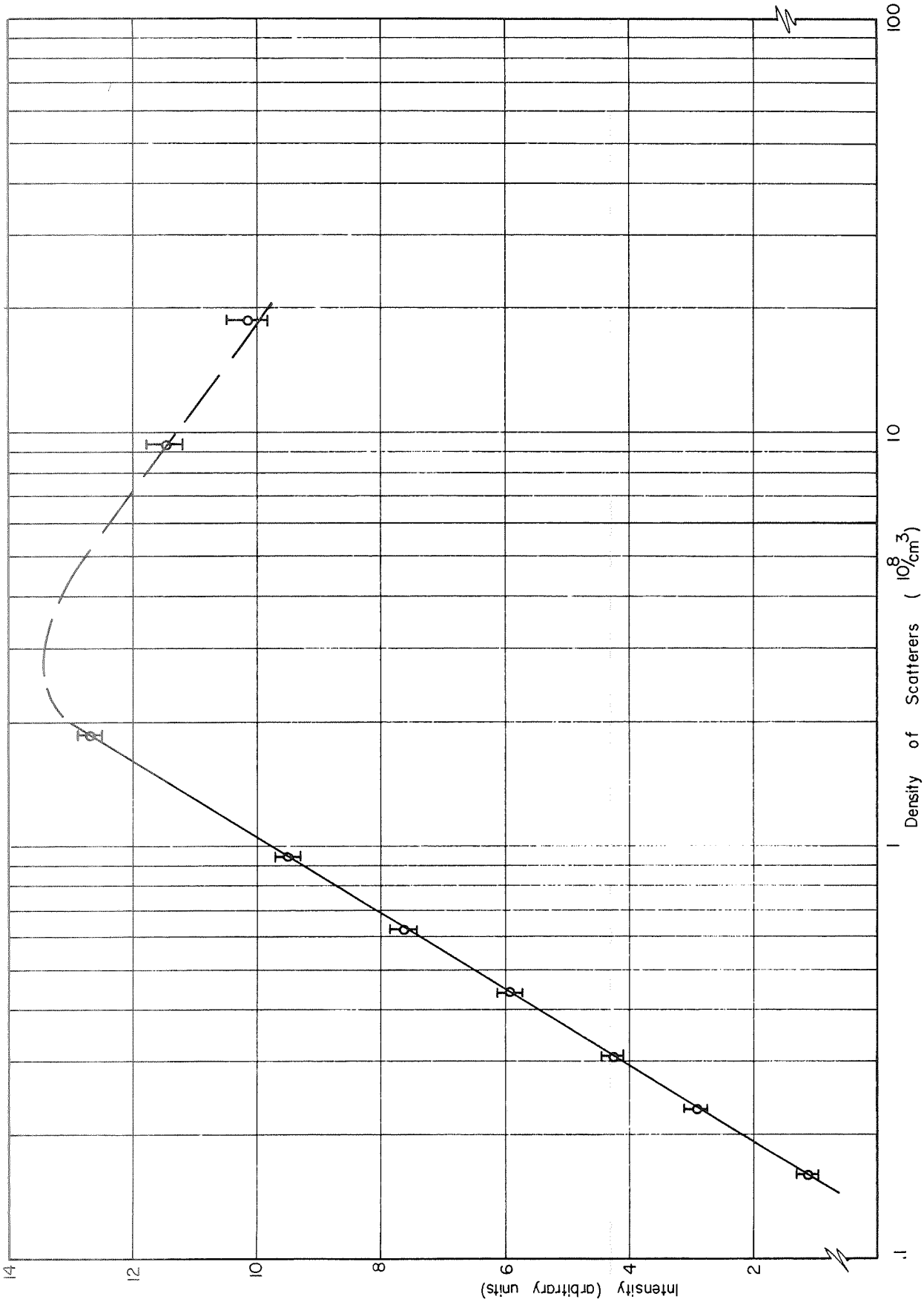

Figure 41. Experimental scattering intensity vs. density of scatterers.

phenomenon. Because the scattering particles are not much greater than the wavelength in size, multiple scattering effects can be expected to cause a decrease in the intensity detected rather than degrading coherence properties of the source light pulse and/or dependent scattering effects (just as was observed for the laser radar computer model in section 4.3). Although the latter point (degradation of dependent scattering effect) can not be verified, the decrease in scattered intensity detected due to photons scattered out of the detection range manifests itself in the last two data points of Figure 41. No smearing or spreading of the Q-pulse on traversing the scattering medium is observed for any density (using the 7 ns fast response time mode of the photomultiplier detector electronics). Thus, the number of photons which undergo multiple scattering and are subsequently recorded is, indeed, insignificant. Further, at these high scatterer densities the Mie scattering patterns of Figures 36 through 39 are lost. Instead, a Gaussian falloff with scattering angle is observed. Experimental data thus lead to qualitative agreement with the multiple scattering theory of section 4.3.

An attempt to achieve quantitative verification by applying the Monte-Carlo simulation program (see Appendix C) failed. To obtain a significant number of singly or multiply scattered photons at any scattering angle requires so many case histories (photon paths) that G-20 computation times of several days or even weeks would be entailed. Thus theoretical model results applicable to the specific experimental configuration are not available.

5.3 Other Scattering Experiments

A number of experimenters[80-85] have either compared laser light scattering to that from conventional sources or compared the scattering

of laser light with light scattering theory. In most cases, a HeNe laser and a Xenon lamp have been the sources and latex spheres or a fog of water droplets the scattering medium. Harris[80] has compared the light scattered by latex spheres (in a water-carrying medium) ranging in diameters from 0.088 to 3.49μ for both a HeNe laser and a Xenon lamp utilizing a 100 Å filter centered at 6328 Å. Using a detector aperture equivalent to one or less coherence cells but with a detector response time much too slow to follow signal fluctuations due to scatterer medium ensemble configuration changes, Harris observed no significant difference between scattering of coherent and incoherent light. This, of course, agrees with the results of section 5.2.1. Harris has simply verified Mie scattering for the independent scattering case. The only additional contribution beyond the results of section 5.2.1 is that many more scatterer sizes were observed and vertical and horizontal polarization data were obtained.

Carrier[81] and Reisman[82] have made comparisons of fog-scattered coherent and incoherent light using HeNe lasers and a tungsten and Xenon lamp, respectively, as their sources. Although the characteristic time for ensemble configuration changes is longer for a water droplet fog than for latex spheres in a water medium, both Carrier and Reisman used detector response times of one to four seconds thus wiping out fluctuations due to dependent scattering. Additionally, they used detector apertures much larger than that equivalent to one coherence cell, thus further averaging any dependent scattering effects. That their results agree with the Mie theory is not at all surprising. Carrier did observe an anomalous peaking in the forward scatter direction. This can easily be attributed to the well-known dependent scattering effect in the direction

of propagation of the primary wave for a medium consisting of a single kind of particle.

Note that in all three of the above described experiments, multiple scattering effects were avoided by maintaining a low density of scatterers. Thus, just as was discovered in section 5.2.2, the dependent (N^2) scattering effect can not be observed, for scatterer densities are far too low. To attempt observation of the N^2 effect, three changes in the experimental arrangement suggest themselves. First, the effective scattering volume can be increased up to the point at which loss of phase relationships between extremities of the scattering volume set in (i.e., scattering volume equal to or less than one dependent scattering aggregate). Second, the source wavelength might be increased to allow a larger detector aperture (still equal to one coherence cell) to be utilized. Third, the scattering particle size might be greatly reduced, resulting in much longer path lengths between scatterings and thus allowing the scatterer density to be greatly increased. Of the three changes (and other suggested changes) only the last may allow for the orders of magnitude increase in scatterer density necessary for the N^2 effect to be observable. However, as one goes to smaller scatterers (Rayleigh scatterers) the cross section for scattering by each particle decreases as the square of the particle diameter. It becomes increasingly difficult to maintain a signal-to-noise ratio above one as spurious scattering effects become more dominant.

George[83,84] and Watson[85] have been able to observe Rayleigh scattering with elaborate experimental apparatus. Both have used a ruby laser as the light source. George used a laser operating in a non-Q-switched manner, which resulted in a large number of random pulses, each of approximately 250 ns time duration with random amplitude distribution and overall

pulse-train time duration of 150 μsec. Electronic integrators to average the photomultiplier detector outputs over the entire duration of laser action were utilized. Watson used a laser operating in a Q-switched manner producing a single pulse of 20 ns duration. George's experimental scatterers were neon, argon, xenon, oxygen, nitrogen, air, carbon dioxide, sulfur hexaflouride, and propane while nitrogen alone was used by Watson. Further description of the apparatus can be found in the literature.[84,85]

Given the much higher scatterer densities allowable with small Rayleigh scatterers (i.e., without multiple scattering effects becoming dominant) should one expect to observe dependent scattering? George used a scattering volume of

$$4 \text{ mm diam. circle} \times \frac{\text{one cm depth}}{\sin\ (\theta/2)} \qquad (114)$$

where θ is the angle of observation. Berkley and Wolga[86] have studied the coherence properties of a non-Q-switched ruby laser with the result that the small scattering volume used by George is easily within one dependently scattering aggregate. Similarly, Watson has utilized an experimental setup resulting in a scattering volume approximately the same as that of George which is easily within a dependently scattering aggregate for the Q-switched laser case (as described in section 5.2). Thus, again referring to (91), the maximum ratio of dependent to independent scattering for a=2mm and m=1 is

$$R_{max.} = 6.87 \times 10^{-10} N. \qquad (115)$$

The experimental densities used are at or just below atmospheric ($\sim 10^{25}$). Thus, the maximum ratio of dependent to independent scattering is

$$R_{max.} \gtrsim 10^{15}. \qquad (116)$$

Note that the mean distance between scatterings, L_o (determined by using (100) and (102)), is many orders of magnitude greater than the wavelength and photon path within the scattering medium ($L_o > 10^3$m). Multiple scattering effects should then be insignificant and dependent scattering highly dominant.

The results of George's experiment are shown in Figures 42 and 43. According to Rayleigh's theory, if the observation is made in the horizontal plane and if the incident light beam is vertically polarized, then the same intensity value ought to be observed at all angles of scattering. The data of Figure 42 do not adhere to theory. Rather, they appear to have a linear falloff vs. angle with a wide intensity fluctuation about each data point. The 95 per cent confidence margins with each averaged value are shown in Figure 42. The linear falloff with angle and random fluctuation was observed both for Argon at 760 mm Hg pressure and Xenon at 140 mm pressure.

If the incident beam is horizontally polarized, the Rayleigh theory suggests that a $\sin^2\theta$ relation for the scattered intensity can be expected. Figure 43a shows that, in the case of Argon at atmospheric pressure, the experimental data closely fit the theoretical curve. This was true also for Xenon at 140 mm Hg. Random fluctuations at each data point were, however, still observed. The observed intensity at 90° (Figure 43a) can be fully attributed to the vertically polarized component present in the incident beam.

Watson,[85] using nitrogen at atmospheric pressure, matched his experimental data to Rayleigh's theory. Although somewhat less, random

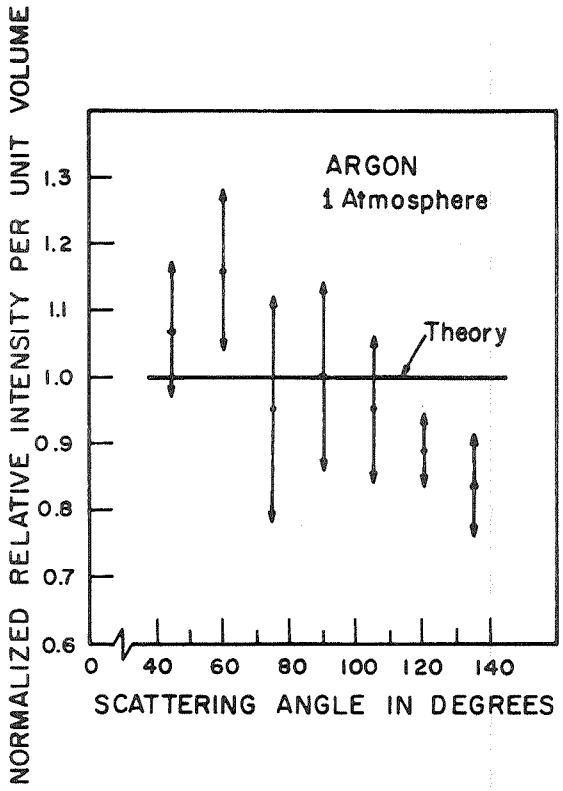

a. Argon at one atmosphere.

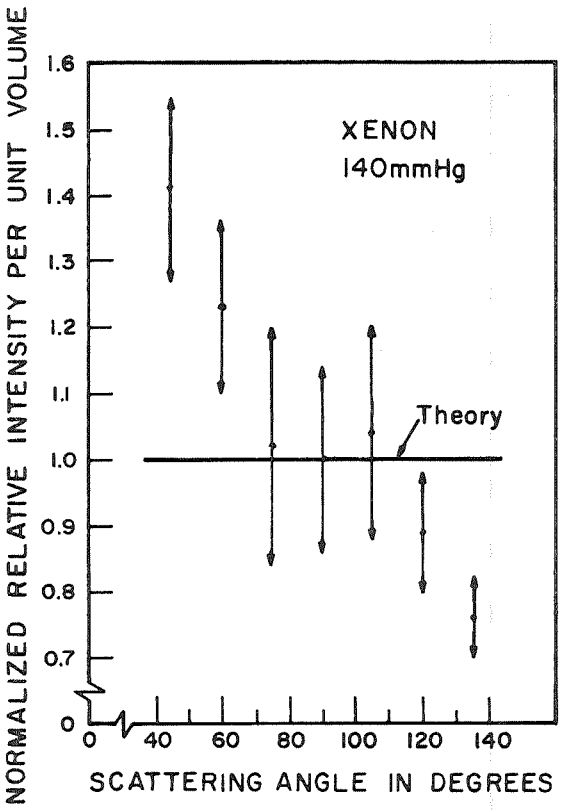

b. Xenon at 144 mm Hg.

Figure 42. Angular distribution of scattered light intensity for vertically polarized incident beam.

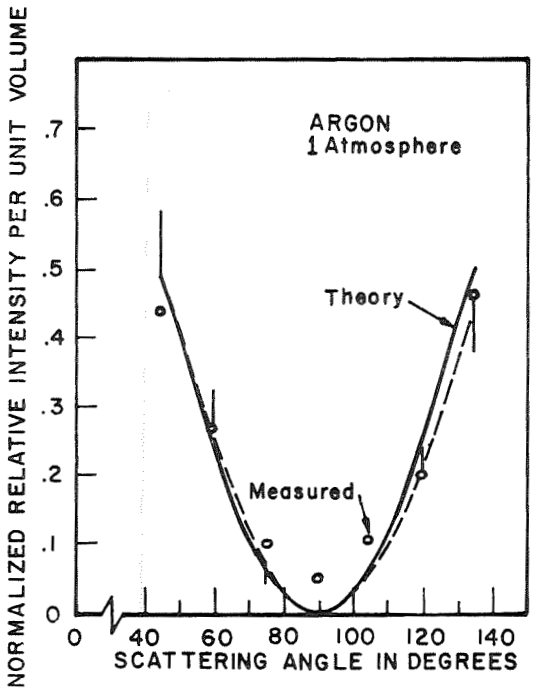

a. Argon at one atmosphere.

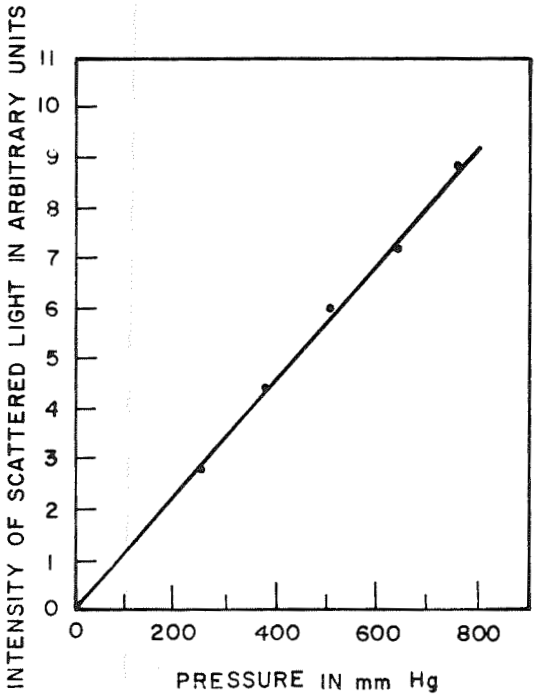

b. Pressure dependence.

Figure 43. Angular distribution of scattered light intensity for horizontally polarized beam in argon at one atm. and pressure dependence of scattered light intensity at 135° with the incident beam in argon at room temperature.

fluctuations were still present. George's[84] data for nitrogen are almost exactly the same as those shown in Figures 42 and 43a for argon and xenon. Thus, differences between experimenter's data cannot be attributed to differences in scattering media. In fact, for all the media George used--neon, argon, xenon, oxygen, nitrogen, and air--the same results as in Figures 42 and 43a were obtained. The question then arises: can these rather peculiar data be attributed to dependent scattering effects?

First, the fluctuations in scattered intensity can be attributed to spatial detection effects. Just as was described in section 5.2.2, the effective aperture at the detector is equivalent to several coherence cells. As seen in section 5.2.2, a quantitative figure for the number of coherence cells used by George and Watson cannot be determined. However, based on the percentage fluctuation in the data, it can be said that the equivalent aperture in the George experiment is equal to 5 to 25 coherence cells (the actual aperture was of 400μ diameter at a range of five cm). Since the per cent of fluctuations is less in the Watson experiment, the equivalent aperture here is equal to a greater number of coherence cells. (The actual aperture here is one mm at a range of 10 cm.)

Second, the greatly enhanced signal due to dependent (N^2) scattering as indicated by (116) did not seem to materialize. In fact, the data of Figure 43b (taken from George[84]) show that an ultralinear intensity vs. scatterer number density relationship persists in the George experiment. This would seem to indicate that no dependent scattering is present in the George data. Yet, other data from this same experiment contradict that of Figure 43b. The differential scattering cross section for various gases at a scattering angle of 60° was theoretically calculated and experimentally observed. The measured values were found to be approximately twice as large as those predicted by the classical theory. George

and his coworkers never explained this descrepancy, although they point out that errors involved in the cross section measurements would not allow for experimental results which deviate more than 35 per cent from the true values. Measured cross sections twice as large as theoretical can easily be explained on the basis of nonlinear, dependent scattering theory. Further, comparison of the relative scattering intensity for various gases shows a consistent discrepancy between theory and experiment. Table 13 shows data for scattering by gases at 60°, atmospheric pressure, and room temperature.

Table 13. Relative Scattering Intensity for Various Gases at 60°, Atmospheric Pressure, and Room Temperature.

Scatt. Medium	Ne	A	Xe	O_2	N_2	Air	CO_2	SF_6	C_3H_8
Exp. Values by George	0.36	6.35	43.0	6.79	7.83	7.72	20.8	45.8	147.8
Calc. Values by George	0.047	0.82	5.57	0.88	1.01	1.0	2.69	5.93	19.1
Exp./ Cal.	7.66	7.74	7.72	7.72	7.75	7.72	7.73	7.72	7.73

The combination of Table 13 data along with the contradictory data indicated earlier in this paragraph make it impossible to say whether dependent scattering effects are being observed.

5.4 Conclusions

Although several of the theoretical aspects described in Chapters 3 and 4 are verified by experiment, the N^2 dependent scattering effect could not be observed. By greatly increasing the scatterer density and

utilizing Rayleigh small particle scatterers instead of large Mie scatterers, N^2 effects might be observed. The experiments of George and Watson have achieved the high density scattering necessary. However, Watson did not observe N^2 scattering and it is impossible to conclude that George observed this scattering. Thus, verification of the dependent scattering theory of section 3.3 has not yet been realized.

LIST OF REFERENCES

1. D. Atlas, J. Metcalf, J. Richter, and E. Gossard, J. Atmos. Sciences, 27, 903 (1970).

2. R. M. Schotland, J. Bradley, and A. M. Nathan, Technical Report 67-2, ECOM-02207-F (1967).

3. C. G. Little, "On the Potential of Acoustic Echo Sounding Techniques for the Study of the Atmosphere," Session IV Paper at the Sixth Symposium on Remote Sensing of Environment, Ann Arbor, Michigan (1969).

4. L. G. McAllister and J. R. Pollard, "Acoustic Sounding of the Lower Atmosphere," Session IV Paper at the Sixth Symposium on Remote Sensing of Environment, Ann Arbor, Michigan (1969).

5. R. K. Cook, "Subsonic Atmospheric Oscillations," Reports of the Sixth International Congress on Acoustics, Tokyo, Japan (1968).

6. D. L. Fried, Jour. Opt. Soc. of Amer., 57, 175 (1967).

7. R. W. Lee and A. T. Waterman, Proc. IEEE , 54, 454 (1966).

8. W. L. Smith, Appl. Optics, 9, 1993 (1970).

9. Sessions I, V, VI, VII, IX of the Sixth Symposium on Remote Sensing of Environment, Ann Arbor, Michigan (1969).

10. D. Q. Wark, "Atmospheric Temperature Determinations from the Nimbus III Satellite," Session IV Paper at the Sixth Symposium on Remote Sensing of Environment, Ann Arbor, Michigan (1969).

11. S. Twomey, Jour. of Atmos. Sciences, 27, 515 (1970).

12. C. E. Junge, Jour. of Meteorology, 11, 323 (1954).

13. R. K. Long and D. B. Rensch, Appl. Optics, 9, 1563 (1970).

14. H. C. van de Hulst, Light Scattering by Small Particles, J. Wiley & Sons, Inc., New York, 1957.

15. K. Bullrich, "Scattered Radiation in the Atmosphere and the Natural Aerosol," in Advances in Geophysics, V. 10, Academic Press, New York, 1964.

16. J. D. Lawrence, M. P. McCormick, and S. H. Melfi, "Optical Radar Studies of the Atmosphere," Session II, Session IV Paper at the Sixth Symposium on Remote Sensing of Environment, Ann Arbor, Michigan (1969).

17. E. W. Barrett and O. Ben-Dov, Jour. of Appl. Meteor., 6, 500 (1967).

18. W. B. Johnson, "Lidar Applications in Air Pollution Studies," Stanford Research Institute Report Series, Menlo Park, California (1968).

19. D. Deirmendjian, Appl. Optics, 3, 187 (1964).

20. R. Penndorf, Jour. Opt. Soc. Amer., 52, 402 (1962).

21. B. Herman, "Determination of Aerosol Size Distribution from Lidar Measurements," Session II Paper at the Third Laser Radar Conference, Ocho Rios, Jamaica (1970).

22. E. Palmer, "Aerosol-Particle Parameters from Light Scattering Data," Session II Paper at the Third Laser Radar Conference, Ocho Rios, Jamaica (1970).

23. J. A. Reagan, "A Bistatic Lidar for Measuring Atmospheric Aerosol Distributions," Session II Paper at the Third Laser Radar Conference, Ocho Rios, Jamaica (1970)1

24. J. T. Beard, "The Quantitative Determination of Gaseous Air Pollutants by Long Path Infrared Transmission Spectroscopy," at Air Pollution Control Association's 61st Annual Meeting, St. Paul, Minnesota (1969).

25. C. B. Ludwig, R. Bartle, and M. Griggs, NASA CR-1380, General Dynamics Corporation Report, San Diego, California (1969).

26. R. K. Long, Ohio State Eng. Exp. Sta. Bull. No. 199, 1965.

27. P. L. Hanst and W. J. Henson, "Air Pollutant Infrared Spectra and Absorption Coefficients at Laser Wavelengths," NASA Electronics Res. Center, Cambridge, Mass. (1969).

28. G. Herzberg, Molecular Spectra and Molecular Structure, vol. 2, Infrared and Raman Spectra of Polyatomic Molecules, van Nostrand, Princeton, N. J., 1960.

29. P. L. Hanst, Laser Focus, 6, 19 (1970).

30. W. B. Tiffany, Applied Optics, 7, 67 (1968).

31. A. Lempicki and H. Samuelson, Appl Phys. Lett., 4, 133 (1963).

32. P. Sorokin, Scientific American, 220, 30 (1969).

33. J. Cooney, Jour. of Appl. Meteor., 9, 182 (1970).

34. T. Kobayasi and H. Inaba, Appl. Phys. Lett., 17, 139 (1970).

35. W. M. Elsasser, Atmospheric Radiation Tables, Meteorological Monographs, 4, 4 (1960).

36. C. I. Beard, T. H. Kays, and V. Twersky, IEEE Trans. on Antennas and Propagation, AP-15, 99 (1967).

37. V. I. Tatarski, Propagation of Waves in a Turbulent Atmosphere, IZD-VO Akad. Nauka, Moscow, 1967.

38. O. A. Germogenova and A. Siegel, Appl. Optics, 8, 1849 (1969).

39. A. T. Young, Appl. Optics, 8, 2431 (1969).

40. J. W. Goodman, Stanford University Electronics Laboratory, Stanford, California, several private communications, 1970.

41. G. Biernson and R. F. Lucy, Proc. of the IEEE, 51, 202 (1963).

42. R. F. Lucy, Sylvania Electronics, Inc., Waltham, Mass., private communication, 1970.

43. J. A. Ratcliffe, Reports on Progress in Physics, 19, 222 (1956).

44. L. Mandel, Proc. Physical Society, 74, 233 (1959).

45. S. O. Rice, Noise and Stoch. Proc., N. Wax (ed.), Dover Press, New York, 1954, p. 98.

46. R. B. Crane, Jour. Opt. Soc. of Amer., 60, 1658 (1970).

47. J. W. Goodman, Introduction to Fourier Optics, McGraw-Hill, New York, 1968, p. 119.

48. T. Hagfors, Radar Astronomy, J. V. Evans and T. Hagfors (eds.), McGraw-Hill, New York, 1968.

49. J. W. Goodman, Introduction to Fourier Optics, McGraw-Hill, New York, 1968, p. 86.

50. M. Born and E. Wolf, Principles of Optics, The MacMillan Company, New York, 1964, p. 511.

51. E. F. Erickson and R. M. Brown, Jour. Opt. Soc. Amer., 57, 367 (1967).

52. W. S. Chang and N. R. Kilcoyne, Appl. Optics, 4, 1404 (1965).

53. A. Consortini, L. Ronchi, and A. M. Scheggi, Radio Science, 1, 523 (1966).

54. J. R. Kerr, P. J. Titterton, and C. M. Brown, Appl. Optics, 8, 2233 (1969).

55. A. P. Ivanov and A. Khairullina, Optics and Spectroscopy, 23, 83 (1967).

56. K. S. Shifrin, The Scattering of Light in a Turbid Medium, IZD-VO Akad. Nauka, Moscow, 1951.

57. O. A. Germogenova, Izv. Akad. Nauk SSSR Fiz. Atmos. i Okeana, 227, 1 (1965).

58. H. C. van de Hulst, Light Scattering by Small Particles, John Wiley & Sons, Inc., New York, 1957, p. 4.

59. S. Twomey and H. B. Howell, Appl. Optics, 4, 501 (1965).

60. A. Papoulis, Probability, Random Variables, and Stochastic Processes, McGraw-Hill, New York, 1965.

61. V. Twersky, Jour. Opt. Soc. Amer., 52, 145 (1962).

62. V. Twersky, Jour. Mathematical Physics, 8, 589 (1967).

63. V. Twerksy, Jour. Opt. Soc. Amer., 60, 908 (1970).

64. H. C. van de Hulst, Light Scattering by Small Particles, John Wiley & Sons, Inc., New York, 1957, p. 65.

65. E. J. McCartney, Navigation, 11, 218 (1967).

66. E. J. Chatterton, "Optical Communications Employing Semiconductor Lasers," Lincoln Laboratory Technical Report 392, Boston, Mass. (1965).

67. H. M. Heggestad, "Optical Communications through Multiple-Scattering Media," Dissertation, Department of Electrical Engineering, Mass. Inst. of Tech., Cambridge, Mass. (1969).

68. G. W. Kattawar and G. N. Plass, Appl. Optics, 7, 869 (1968).

69. G. W. Kattawar, North Texas State Univ., Denton, Texas, private communication, 1971.

70. R. E. Danielson, D. Moore and H. C. van de Hulst, Jour. of Atmos. Sciences, 26, 1078 (1969).

71. R. T. H. Collis, "Lidar," Proceedings of the Scientific Meetings of the Panel on Remote Atmospheric Probing, Report to National Research Council, Washington, D. C. (1969).

72. H. C. van de Hulst, Light Scattering by Small Particles, John Wiley & Sons, Inc., New York, 1957, p. 152.

73. R. O. Gumprecht, Jour. Opt. Soc. Amer., 42, 226-231 (1952).

74. V. H. Holl, Optik, 1-2, 219 (1946).

75. W. E. Clark, Jour. Atmos. Sciences, 24, 678 (1967).

76. H. Engelhard and H. Friess, Kolloid-Zeitschrift, 81, 129 (1937).

77. Private communications at the Second Laser Radar Conference, Brookhaven National Laboratory, Stony Brook, New York (1969).

78. E. H. Kennard, Kinetic Theory of Gases, McGraw-Hill, New York (1938).

79. H. H. Denman and W. Heller, Angular Scattering Functions for Spheres, Wayne State University Press, Detroit, Michigan (1966).

80. F. S. Harris, G. Sherman, and F. Morse, IEEE Trans. on Antennas and Propagation, AP-15, 141(1967).

81. L. W. Carrier and L. Nugent, Appl. Optics, 4, 1457(1965).

82. E. Reisman, G. Cumming, and C. Bartky, Appl. Optics, 6, 1969(1967).

83. T. V. George, L. Slama, M. Yokoyama, and L. Goldstein, Phys. Rev. Letters, 11, 403(1963).

84. T. V. George, L. Goldstein, L. Slama, and M. Yokoyama, Phys. Rev., 137, A369(1965).

85. R. D. Watson and M. K. Clark, Phys. Rev. Letters, 14, 1057(1965).

86. D. A. Berkley and G. Wolga, Phys. Rev. Letters, 9, 479(1962).

APPENDIX A.
NUMERICAL ANALYSIS FOR COHERENCE CELL DETERMINATION

The program used to calculate the number of spatial coherence cells vs. normalized range for a circular aperture is listed below.

MAIN

```
      COMMON U
      REAL*8 XL,U,H,ANS
      EXTERNAL AUX
      XL=0.0
      U=0.0
      H=3.0
      DO 20 L=1,10
      U=U+1.
      WRITE(6,21)
21    FORMAT(/// 15H INTEGRAL VALUE /)
      CALL GQU37(XL,U,AUX,H,ANS)
      WRITE(6,22)ANS
22    FORMAT(E14.7)
      AM=3.14159*((U/8.)**2)/ANS
      WRITE(6,23)
23    FORMAT(// 28H NUMBER OF CORRELATION CELLS /)
      WRITE(6,24) AM
24    FORMAT(E14.7)
20    CONTINUE
      END
```

```
      SUBROUTINE GQU3Z(XL,U,AUX,H,ANS)
      REAL*8 X(96),W(96),ANS,C,S,Z,D,A,F,Y,XL,U,H
      REAL*8 X2(40),X3(16),W2(40),W3(16)
      EQUIVALENCE (X(41),X2(1)),(X(81),X3(1)),(W(41),W2(1)),
     1           (W(81),W3(1))
      DATA X/       0.0162767448496O2,      -0.0162767448496O2,
     2              0.0488129851360O9,      -0.0488129851360O9,
     C              0.0812974957644O5,      -0.0812974957644O5,
     2              0.1136958501106O5,      -0.1136958501106O5,
     C              0.1459737146548O6,      -0.1459737146548O6,
     2              0.1780968823676I8,      -0.1780968823676I8,
     C              0.2100313104605O7,      -0.2100313104605O7,
     2              0.2417431561638O0,      -0.2417431561638O0,
     C              0.2731988125910O9,      -0.2731988125910O9,
     2              0.3043649443544O6,      -0.3043649443544O6,
     C              0.3352085228926O5,      -0.3352085228926O5,
     2              0.3656968614723I3,      -0.3656968614723I3,
     C              0.3957976498289O8,      -0.3957976498289O8,
     2              0.4254789834073O0,      -0.4254789834073O0,
     C              0.4547094221677I3,      -0.4547094221677I3,
     2              0.4834579739205O6,      -0.4834579739205O6,
     C              0.5116941771546I7,      -0.5116941771546I7,
     2              0.5393881083243I7,      -0.5393881083243I7,
     C              0.5665104185613I7,      -0.5665104185613I7,
     2              0.5930323647775I2/
      DATA X2/      0.6189258401254I8,      -0.6189258401254I8,
     2              0.6441634037849I7,      -0.6441634037849I7,
     C              0.6687183100439I6,      -0.6687183100439I6,
     2              0.6925645366421I1,      -0.6925645366421I1,
     C              0.7156768123489I7,      -0.7156768123489I7,
     2              0.7380306437444O0,      -0.7380306437444O0,
     C              0.7596023411766I7,      -0.7596023411766I7,
     2              0.7803690438674I3,      -0.7803690438674I3,
     C              0.8003087441391I0,      -0.8003087441391I0,
     2              0.8194003107379I1,      -0.8194003107379I1,
     C              0.8376235112281I7,      -0.8376235112281I7,
     2              0.8549590334346O1,      -0.8549590334346O1,
     C              0.8713885059092I6,      -0.8713885059092I6,
     2              0.8868945174024I0,      -0.8868945174024I0,
     C              0.9014606353158I2,      -0.9014606353158I2,
     2              0.9150714231208I8,      -0.9150714231208I8,
     C              0.9277124567223O8,      -0.9277124567223O8,
     2              0.9393703397527I5,      -0.9393703397527I5,
     C              0.9500327177844I7,      -0.9500327177844I7,
     2              0.9596882914487I2/
      DATA X3/      0.9683268284632I4,      -0.9683268284632I4,
     2              0.9759391745851I6,      -0.9759391745851I6,
     C              0.9825172635630I4,      -0.9825172635630I4,
     2              0.9880541263296I3,      -0.9880541263296I3,
     C              0.9925439003237I2,      -0.9925439003237I2,
     2              0.9959818429872O9,      -0.9959818429872O9,
     C              0.9983643758631I1,      -0.9983643758631I1,
     2              0.9996895038832I0/
```

```
      DATA W/     0.0225506144692353,     0.0325506144692353,
     C            0.0325161197133958,     0.0325161197133958,
     C            0.0324471637140534,     0.0324471637140534,
     C            0.0323438225685575,     0.0323438225685575,
     C            0.0322062947040030,     0.0322062947040030,
     C            0.0320344562231092,     0.0320344562231092,
     C            0.0311279589044611,     0.0311279589044611,
     C            0.0315899330770727,     0.0315899330770727,
     C            0.0313164256564661,     0.0313164256564661,
     C            0.0310103296486213,     0.0310103296486213,
     C            0.0306713761233650,     0.0306713761233650,
     C            0.0302999154260027,     0.0302999154260027,
     C            0.0299063844136223,     0.0299063844136223,
     C            0.0294910000859167,     0.0294910000859167,
     C            0.0290543141860565,     0.0290543141860565,
     C            0.0285974110658015,     0.0285974110658015,
     C            0.0281206007516243,     0.0281206007516243,
     C            0.0276241962726029,     0.0276241962726029,
     C            0.0271084857295611,     0.0271084857295611,
     C            0.0265737833075472,     0.0265737833075472,
     C            0.0260203433229343,     0.0260203433229343,
     C            0.0254484641709954,     0.0254484641709954,
     C            0.0248584390115892,     0.0248584390115892,
     C            0.0242505777857721,     0.0242505777857721,
     C            0.0236251444273744,     0.0236251444273744,
     C            0.0229824811911911,     0.0229824811911911,
     C            0.0223228307716223,     0.0223228307716223,
     C            0.0216465611164164,     0.0216465611164164,
     C            0.0209539477477611,     0.0209539477477611,
     C            0.0202453602931605,     0.0202453602931605,
     C            0.0195211867042245,     0.0195211867042245,
     C            0.0187818708421092,     0.0187818708421092,
     C            0.0180277729126094,     0.0180277729126094,
     C            0.0172592817717314,     0.0172592817717314,
     C            0.0164768122954861,     0.0164768122954861,
     C            0.0156807971257114,     0.0156807971257114,
     C            0.0148717033677355,     0.0148717033677355,
     C            0.0140500977111183,     0.0140500977111183,
     C            0.0132164406653082,     0.0132164406653082,
     C            0.0123713939142849,     0.0123713939142849,
     C            0.0115154220744644,     0.0115154220744644,
     C            0.0106490917173634,     0.0106490917173634,
     C            0.0097729722306483,     0.0097729722306483,
     C            0.0088875355852252/
      PI=3.
      N=1
      DO 1 I=1,
      N=
      A=(
      DO 1 J=1,5
      Y=
      CALL
      S=
      N=
      IF(
      END
```

```
      SUBROUTINE BSLJZ(X,FJ,NMAX,A,ND,IERR,FJAPRX,RR)
      REAL*8 FJ(1),FJAPRX(1),RR(1),A,X,EPSLON,SUM,D1,R,S,FL,Y,TANS
      REAL*8 DENOM,FLMBDA
      NMAXT=NMAX
      IF(NMAXT.GE.0)GO TO 30
      IF(DABS(A).LE.1.0D-15)GO TO 10
      GO TO 20
10    IERR=4
      RETURN
20    NMAXAB=IABS(NMAXT)
      NMAXT=1
30    IF(A.GT.0.0)GO TO 40
      IF(DABS(A).LE.1.0D-15)GO TO 40
      IERR=1
      RETURN
40    IF(A.LT.1.0)GO TO 70
      IERR=2
      RETURN
70    IF(X.GT.0.0)GO TO 130
      IERR=3
      RETURN
130   IERR=0
      EPSLON=.5D0*10.**(-ND)
      NMP1=NMAX+1
      DO 160 N=1,NMP1
160   FJAPRX(N)=0.0
      SUM=(X/2.)**A/DGAMMA(1.+A)
      D1=2.302600*ND+1.386300
      IF(NMAXT.LE.0)GO TO 230
      Y=.5D0*D1/NMAXT
      CALL TZ(Y,TANS)
      R=NMAXT*TANS
      GO TO 240
230   R=0.0
240   Y=.7357600*D1/X
      CALL TZ(Y,TANS)
      S=1.359100*X*TANS
      IF(R.GT.S)GO TO 280
      MU=1+IDINT(S)
      GO TO 290
280   MU=1+IDINT(R)
290   M=0
      FL=1.
      LIMIT=(MU/2)
320   M=M+1
      FL=FL*(M+A)/(M+1.D0)
      IF(M.LT.LIMIT)GO TO 320
      M=2*M
      R=0.0
      S=0.0
390   DENOM=2.*(A+M)/X-R
      IF(DABS(DENOM).LE.1.0D-15)DENOM=DENOM+1.0D-15
430   R=1./DENOM
```

```
      MMOD2=MOD(M,2)
      IF(MMOD2.NE.0)GO TO 480
      FL=FL*(M+2.D0)/(M+2.*A)
      FLMBDA=FL*(M+A)
      GO TO 490
480   FLMBDA=0.0
490   S=R*(FLMBDA+S)
      IF(M.LE.MMAXT)RR(M)=R
      M=M-1
      IF(M.GE.1)GO TO 390
      FJ(1)=SUM/(1.+S)
      IF(NMAXT.EQ.0)GO TO 570
      DO 560 M=1,MMAXT
560   FJ(M+1)=RR(M)*FJ(M)
570   DO 640 M=1,MMP1
      IF(DABS((FJ(M)-FJAPRX(M))/FJ(M)).LE.EPSLON)GO TO 640
      DO 610 M=1,MMP1
610   FJAPRX(M)=FJ(M)
      MU=MU+5
      GO TO 290
640   CONTINUE
      IF(MMAX.GE.0)RETURN
      FJ(2)=2.*A*FJ(1)/X-FJ(2)
      IF(MMAXAB.EQ.1)RETURN
      DO 650 M=2,MMAXAB
650   FJ(M+1)=2.*(A-M)*FJ(M)/X-FJ(M-1)
      RETURN
      END
```

```
      SUBROUTINE AUX(X,Y)
      COMMON AA
      REAL*8 X,Y,FJ(2),FJAPRX(2),A,RR(2)
      MMAX=1
      A=0.
      ND=6
      CALL BSLJZ(X,FJ,MMAX,A,ND,IERR,FJAPRX,RR)
      Y=(1./(X*DCOS(X/AA))-((1.-(X/AA)**2)**.5)/2.)*(FJ(2))**2
      RETURN
      END
```

APPENDIX B.
DETERMINATION OF $R_{\ell,p}-R_{\ell,s}$

$$R_{\ell,p} = [(u_\ell+u'_p)^2+(v_\ell+v'_p)^2+(h-(w_\ell+w'_p))^2]^{1/2}$$

and

$$R_{\ell,s} = [(u_\ell+u'_s)^2+(v_\ell+v'_s)^2+(h-(w_\ell+w_s))^2]^{1/2}$$

where

h is the vertical distance from the detector plane to the uv plane passing through the center of the scattering region,

(u_ℓ,v_ℓ,w_ℓ) is the location of the ℓth aggregate, and

$(u'_\ell,v'_\ell,w'_\ell)$ is the location of the scatterer under consideration within the ℓth aggregate.

The restrictions on illuminated volume diameter and plane of observation area allow one to say

$$(u_\ell+u'_p)^2 + (v_\ell+v'_p)^2 << (h-(w_\ell+w'_p))^2$$

and similarly for subscript s replacing p. Thus $R_{\ell,p}$ and $R_{\ell,s}$ can be written

$$R_{\ell,p} = [h-(w_\ell+w'_p)]\ \left[1+\frac{(u_\ell+u'_p)^2+(v_\ell+v'_p)^2}{(h-(w_\ell+w'_p))^2}\right]^{1/2}$$

and

$$R_{\ell,s} = [h-(w_\ell+w')]\ \left[1+\frac{(u_\ell+u'_s)^2+(\bar{v}_\ell+v'_s)^2}{(h-(w_\ell+w'_s))^2}\right]^{1/2}.$$

Using

$$[1+Q]^{1/2} \simeq 1+\frac{Q}{2} \text{ for } Q << 1,$$

one can write $R_{\ell,p}$ and $R_{\ell,s}$ as

$$R_{\ell,p} \simeq (h-(w_\ell+w_p'))\left[1+\frac{(u_\ell+u_p')^2+(v_\ell+v_p')^2}{2(h-(w_\ell+w_p'))^2}\right]$$

and

$$R_{\ell,s} \simeq (h-(w_\ell+w_s'))\left[1+\frac{(u_\ell+u_s')^2+(v_\ell+v_p')^2}{2(h-(w_\ell+w_p'))^2}\right].$$

The h term is constant for any particular point of observation. Thus, (75) can be written as

$$I_o \sum_{\substack{s=1 \\ s\neq p}}^{n_\ell} \left\langle \frac{\exp -2ik\left(w_s'-w_p'+\frac{(u_\ell+u_p')^2+(v_\ell+v_p')^2}{2(h-w_\ell-w_p')}-\frac{(u_\ell+u_s')^2+(v_\ell+v_s')^2}{2(h-w_\ell-w_s')}\right)}{R_{\ell,p}\,R_{\ell,s}} \right\rangle . \quad (B.1)$$

In the denominator $R_{\ell,p}R_{\ell,s} \tilde{\simeq} h^2$. Including only linear terms in the exponential and also letting

$$h-w_\ell-w_p' \tilde{\simeq} h-w_\ell-w_s' \tilde{\simeq} h-w_\ell,$$

(B.1) becomes

$$\frac{I_o}{h^2} \sum_{\substack{s=1 \\ s\neq p}}^{n_\ell} \left\langle \exp -2ik(w_s'-w_p') \right\rangle . \quad (B.2)$$

APPENDIX C.
LIDAR MONTE-CARLO PROGRAM

The program LIDAR is called using the normal control cards appropriate to the G-20. In addition, one data card is needed. The data card should contain: an integer in columns one and two; L_o in columns three to 10; the range, Z, in columns 11 to 18; the number of trials (photons) in columns 19 to 23; the probability of x=0.3 particles in columns 24 to 29; the probability of x=0.6 particles in columns 30 to 35; the probability of x=1.0 particles in columns 26 to 41; the probability of x=2.1 particles in columns 42 to 47; the probability of x=3.6 particles in columns 48 to 53; the probability of x=6.0 particles in columns 54 to 59; the x dimension of the scattering volume at the specified range in columns 60 to 64; the y dimension of the scattering volume at the specified range in columns 65 to 69.

The program LIDAR is listed below.

Main Program--Lidar

```
$     INPUT SOURCE CARDS
$      OUTPUT PROGRAM TAPE
$      EXECUTE
$     FORTRAN
H      NAME LIDAR;
H      EQUIP=CARDRE,PRINTE;
       DIMENSION R(200)
       COMMON A,B,NX,QM,NC,YFL
       A=0.0
       B=1.0
       QM=68435456.
       NC=16381
       NONE=0
       NTWO=0
       NTHREE=0
       NFOUR=0
       NFIVE=0
       NSIX=0
       NSEVN=0
       READ 99,NX,RLO,ZT,MM,PARTA,PARTB,PARTC,PARTD,PARTE,PARTF,APA,APB
99     FORMAT(I2,2F8.0,I5,6F6.4,2F5.1)
       R(1)= .0089
       R(2)= .0089
       R(3)= .0089
       R(4)= .0088
       R(5)= .0088
       R(6)= .0088
       R(7)= .0088
       R(8)= .0088
       R(9)= .0088
       R(10)= .0088
       R(11)= .0200
       R(12)= .0728
       R(13)= .0674
       R(14)= .0611
       R(15)= .0541
       R(16)= .0478
       R(17)= .0425
       R(18)= .0390
       R(19)= .0377
       R(20)= .0386
       R(21)= .0414
       R(22)= .0458
       R(23)= .0514
       R(24)= .0571
       R(25)= .0628
       R(26)= .0672
       R(27)= .0702
       R(28)= .0349
       R(29)= .0086
       R(30)= .0086
       R(31)= .0086
       R(32)= .0086
       R(33)= .0086
       R(34)= .0086
       R(35)= .0085
       R(36)= .0085
       R(37)= .0085
       R(38)= .0085
       R(39)= .0423
       R(40)= .0804
```

R(41)= .0738
R(42)= .0661
R(43)= .0580
R(44)= .0500
R(45)= .0436
R(46)= .0392
R(47)= .0370
R(48)= .0368
R(49)= .0388
R(50)= .0421
R(51)= .0465
R(52)= .0514
R(53)= .0558
R(54)= .0595
R(55)= .0620
R(56)= .0312
R(57)= .0109
R(58)= .0109
R(59)= .0109
R(60)= .0109
R(61)= .0108
R(62)= .0108
R(63)= .0108
R(64)= .0108
R(65)= .0107
R(66)= .0107
R(67)= .0107
R(68)= .0534
R(69)= .1004
R(70)= .0909
R(71)= .0793
R(72)= .0673
R(73)= .0562
R(74)= .0467
R(75)= .0397
R(76)= .0352
R(77)= .0331
R(78)= .0329
R(79)= .0341
R(80)= .0369
R(81)= .0384
R(82)= .0406
R(83)= .0422
R(84)= .0435
R(85)= .0219
R(86)= .0222
R(87)= .0221
R(88)= .0221
R(89)= .0220
R(90)= .0219
R(91)= .0218
R(92)= .0217
R(93)= .0217
R(94)= .0216
R(95)= .0214
R(96)= .1064
R(97)= .1884
R(98)= .1540
R(99)= .1163
R(100)= .0815
R(101)= .0538

R(1 1)= .0322
R(1 2)= .0182
R(1 3)= .0095
R(1 4)= .0045
R(1 5)= .0019
R(1 6)= .0010
R(1 7)= .0010
R(1 8)= .0016
R(1 9)= .0025
R(1 0)= .0034
R(1 1)= .0040
R(1 2)= .0021
R(1 3)= .0364
R(1 4)= .0362
R(1 5)= .0356
R(1 6)= .0353
R(1 7)= .0349
R(1 8)= .0346
R(1 9)= .0342
R(1 0)= .0338
R(1 1)= .0335
R(1 2)= .0331
R(1 3)= .1636
R(1 4)= .2387
R(1 5)= .1355
R(1 6)= .0593
R(1 7)= .0192
R(1 8)= .0056
R(1 9)= .0037
R(1 0)= .0038
R(1 1)= .0030
R(1 2)= .0021
R(1 3)= .0015
R(1 4)= .0013
R(1 5)= .0014
R(1 6)= .0017
R(1 7)= .0024
R(1 8)= .0033
R(1 9)= .0043
R(1 0)= .0023
R(1 1)= .05898
R(1 2)= .05879
R(1 3)= .05828
R(1 4)= .05743
R(1 5)= .05621
R(1 6)= .05475
R(1 7)= .05296
R(1 8)= .05094
R(1 9)= .04866
R(1 0)= .04622
R(1 1)= .21895
R(1 2)= .1641
R(1 3)= .0266
R(1 4)= .0136
R(1 5)= .0132
R(1 6)= .0044
R(1 7)= .0018
R(1 8)= .0028
R(1 9)= .0017
R(1 0)= .0007
R(1 1)= .0014

```
      R(162)= .0013
      R(163)= .0004
      R(164)= .0012
      R(165)= .0022
      R(166)= .0016
      R(167)= .0014
      R(168)= .00085
      R(169)= .20014
      R(170)= .19186
      R(171)= .16864
      R(172)= .13494
      R(173)= .09684
      R(174)= .06061
      R(175)= .03133
      R(176)= .01181
      R(177)= .00236
      R(178)= .00115
      R(179)= .02531
      R(180)= .02393
      R(181)= .00788
      R(182)= .00646
      R(183)= .00494
      R(184)= .00250
      R(185)= .00086
      R(186)= .00096
      R(187)= .00158
      R(188)= .00109
      R(189)= .00019
      R(190)= .00095
      R(191)= .00269
      R(192)= .00189
      R(193)= .00141
      R(194)= .00219
      R(195)= .01056
      R(196)= .0050
      DO 13 M=1,MM
      THETA=0.0
      PHI=0.0
      TL=0.0
      XL=0.0
      YL=0.0
      ZL=0.0
      DO 1 I=1,500
      CALL RANDUU
      NX=0
      Q=1./YFL
      RL=RLO*LOG(Q)
      X=RL*SIN(THETA)*COS(PHI)
      Y=RL*SIN(THETA)*SIN(PHI)
      Z=RL*COS(THETA)
      TL=TL+RL
      XL=XL+X
      YL=YL+Y
      ZL=ZL+Z
      IF(ZL-ZT) 100,2,2
100   CALL RANDUU
      NX=0
      PHI=6.28318*YFL
      CALL RANDUU
      NX=0
      IF(YFL-PARTA)21,201,201
```

```
21      KK=1
        LL=1
        GO TO 207
201     IF(YFL-PARTB)22,202,202
22      KK=29
        LL=29
        GO TO 207
202     IF(YFL-PARTC)23,203,203
23      KK=57
        LL=57
        GO TO 207
203     IF(YFL-PARTD)24,204,204
24      KK=85
        LL=85
        GO TO 207
204     IF(YFL-PARTE)25,205,205
25      KK=113
        LL=113
        GO TO 207
205     IF(YFL-PARTF)26,206,206
26      KK=141
        LL=141
        GO TO 207
206     KK=169
        LL=169
207     CALL RANDUU
        NX=0
        RAN=0.0
        KKK=KK+9
        DO 10 K=KK,KKK
        RAN=RAN+R(K)
        AK=K
        IF(YFL-RAN) 9,9,10
10      CONTINUE
        LLL=LL+16
        DO 11 L=LL,LLL
        N=L+10
        RAN=RAN+R(N)
        AN=L
        AK=(AN*10.) + 2.
        IF(YFL-RAN) 9,9,11
11      CONTINUE
        AK=178.
 9      THETA=3.14159*(AK/180.)
 1      CONTINUE
 2      ZZ=ZT-ZL+Z
        RLL=ZZ/COS(THETA)
        XX=XL-X*(1.-RLL/RL)
        YY=YL-Y*(1.-RLL/RL)
        ZZZ=ZZ+ZL-Z
        TLL=TL-RL+RLL
        AXL=ABSF(XX)
        AYL=ABSF(YY)
        DL=TLL-ZZZ
        IF(AXL-APA)101,4,4
101     IF(AYL-APB)102,4,4
102     PRINT 3,XX,YY,DL,I
 3      FORMAT(3E16.7,I8,/)
        IF(LL-.1) 20,20,31
31      IF(LL-.5) 30,30,32
32      IF(LL-.1) 40,40,33
```

```
33      IF(DL-.5) 50,50,34
34      IF(DL-1.) 60,60,35
35      IF(DL-1.5) 70,70,36
36      NSEVN=NSEVN+1
        GO TO 13
20      NONE=NONE+1
        GO TO 13
30      NTWO=NTWO+1
        GO TO 13
40      NTHRE=NTHRE+1
        GO TO 13
50      NFOUR=NFOUR+1
        GO TO 13
60      NFIVE=NFIVE+1
        GO TO 13
70      NSIX=NSIX+1
        GO TO 13
 4      PRINT 5,XX,YY,DL
 5      FORMAT(3E16.7,/)
13      CONTINUE
        PRINT 16
16      FORMAT(12X,4HNONE,10X,4HNTWO,12X,5HNTHRE,11X,5HNFOUR,11X,5HNFIVE,
       111X,4HNSIX,12X,5HNSEVN)
        PRINT 17,NONE,NTWO,NTHRE,NFOUR,NFIVE,NSIX,NSEVN
17      FORMAT(7I16)
        CALL EXIT
        END
```

Subroutine Randuu

```
H       NAME RANDUU;
H       EQUIP=CARDRE,PRINTE;
        SUBROUTINE RANDUU
        COMMON A,B,NX,QM,NC,C
        IF(NX) 5,6,5
 5      Q=NX
        X=Q/QM
 6      X=X*NC
        KX=X
        X=X-KX
        C=X*(B-A)+A
        RETURN
        END
```

VITA

Herman Charles Sievering was born in Chicago sometime during the month of October 1944. He received the B.S. and M.S. degrees from the University of Illinois in 1966 and 1967. He was a University of Illinois Fellow in 1967, has been a research assistant in the Electro-Physics Laboratory (1968) and Atmospheric Sciences Section of the Water Resources Center (1969) and a Fellow (1970) in the University of Illinois Social Implications of Science Program. He taught an interdisciplinary course in introductory environmental engineering in the fall of 1970. During the fall of 1970 and spring of 1971 he served as research associate with the Illinois Board of Higher Education with interests in developing environmental education.

During the summer of 1966, he was employed as a research engineer with Zenith Radio Corporation and the following summer had the pleasure of employment at the Kernforschungs-anlage near Köln, Germany. The most pleasurable aspect of the latter employment was a trying three-week period of scuba diving in the Bay of Naples for peculiar algae collection while constantly being pursued by Italian mermaids.

His several publications include "Measurement of Acoustic Surface Wave Propagation Characteristics by Reflected Light" (1967), "Material Measurement Schemes for the Far Infrared" (1968), "Laser Radar Coherence Considerations" (1969). He co-authored the papers "An Analysis of the Coherence Problem in Laser Radar" at the Third Laser Radar Conference (1970) in Ocho Rios, Jamaica, and "Air Pollution Discriminatory Measurements," at the Eighth Annual Environmental Engineering Conference (1970) in Washington, D. C.

Mr. Sievering has contributed to the series Advances in Environmental Sciences, and has been an invited lecturer at the University of Michigan.

He was assistant to the Director of the Midwest Conference on Science and Technology and is a member of an advisory body for the Environmental Protection Agency and the Department of the Interior.

Unclassified

Security Classification

DOCUMENT CONTROL DATA - R&D

(Security classification of title, body of abstract and indexing annotation must be entered when the overall report is classified)

1. ORIGINATING ACTIVITY *(Corporate author)*
Department of Electrical Engineering
University of Illinois
Urbana, Illinois 61801

2a. REPORT SECURITY CLASSIFICATION

2b. GROUP

3. REPORT TITLE
THE EFFECT OF COHERENCE AND MULTIPLE SCATTERING ON LASER RADAR AIR POLLUTION MEASUREMENTS

4. DESCRIPTIVE NOTES *(Type of report and inclusive dates)*
Scientific-Interim

5. AUTHOR(S) *(Last name, first name, initial)*
Sievering, H.C.
Mittra, R.

6. REPORT DATE	7a. TOTAL NO. OF PAGES	7b. NO. OF REFS
June 1971	176	86

8a. CONTRACT OR GRANT NO.	9a. ORIGINATOR'S REPORT NUMBER(S)
NGR 14-005-009	Antenna Laboratory Report No. 71-5
b. PROJECT AND TASK NO.	Scientific Report 17
c.	9b. OTHER REPORT NO(S) *(Any other numbers that may be assigned this report)*
d.	UILU-ENG-71-2544

10. AVAILABILITY/LIMITATION NOTICES

11. SUPPLEMENTARY NOTES	12. SPONSORING MILITARY ACTIVITY

13. ABSTRACT

A review of the remote sensing field with applications to air quality monitoring is first undertaken. It is concluded that laser radar is the most promising remote sensing device for the broadest range of air pollution measurements. Two theoretical problems which beset the application of laser radar to atmospheric measurements are coherence and multiple scattering effects upon backscatter and path degradation of the laser pulse.

A radar equation taking account of dependent scattering as related to laser coherence properties is determined. The effect of multiple scattering on laser radar pulse distortion is calculated by a Monte-Carlo technique for all orders of multiple scattering. Multiple scattering effects cause many more photons to be entirely lost from the beam long before pulse distortion occurs. However, the most important conclusion of this work is that dependent scattering may be observed with appropriate laser radar system parameters and that operation in a coherent and an incoherent mode of operation can allow for discrimination of the backscatter signal by pollutant particulates and molecular constituents.

DD FORM 1 JAN 64 1473

Unclassified

Security Classification

Unclassified

Security Classification

14. KEY WORDS	LINK A		LINK B		LINK C	
	ROLE	WT	ROLE	WT	ROLE	WT
Laser Radar						
Air Pollution						
Remote Sensing						
Coherence						
Multiple Scattering						

INSTRUCTIONS

1. ORIGINATING ACTIVITY: Enter the name and address of the contractor, subcontractor, grantee, Department of Defense activity or other organization *(corporate author)* issuing the report.

2a. REPORT SECURITY CLASSIFICATION: Enter the overall security classification of the report. Indicate whether "Restricted Data" is included. Marking is to be in accordance with appropriate security regulations.

2b. GROUP: Automatic downgrading is specified in DoD Directive 5200.10 and Armed Forces Industrial Manual. Enter the group number. Also, when applicable, show that optional markings have been used for Group 3 and Group 4 as authorized.

3. REPORT TITLE: Enter the complete report title in all capital letters. Titles in all cases should be unclassified. If a meaningful title cannot be selected without classification, show title classification in all capitals in parenthesis immediately following the title.

4. DESCRIPTIVE NOTES: If appropriate, enter the type of report, e.g., interim, progress, summary, annual, or final. Give the inclusive dates when a specific reporting period is covered.

5. AUTHOR(S): Enter the name(s) of author(s) as shown on or in the report. Enter last name, first name, middle initial. If military, show rank and branch of service. The name of the principal author is an absolute minimum requirement.

6. REPORT DATE: Enter the date of the report as day, month, year, or month, year. If more than one date appears on the report, use date of publication.

7a. TOTAL NUMBER OF PAGES: The total page count should follow normal pagination procedures, i.e., enter the number of pages containing information.

7b. NUMBER OF REFERENCES: Enter the total number of references cited in the report.

8a. CONTRACT OR GRANT NUMBER: If appropriate, enter the applicable number of the contract or grant under which the report was written.

8b, 8c, & 8d. PROJECT NUMBER: Enter the appropriate military department identification, such as project number, subproject number, system numbers, task number, etc.

9a. ORIGINATOR'S REPORT NUMBER(S): Enter the official report number by which the document will be identified and controlled by the originating activity. This number must be unique to this report.

9b. OTHER REPORT NUMBER(S): If the report has been assigned any other report numbers *(either by the originator or by the sponsor)*, also enter this number(s).

10. AVAILABILITY/LIMITATION NOTICES: Enter any limitations on further dissemination of the report, other than those imposed by security classification, using standard statements such as:

(1) "Qualified requesters may obtain copies of this report from DDC."

(2) "Foreign announcement and dissemination of this report by DDC is not authorized."

(3) "U. S. Government agencies may obtain copies of this report directly from DDC. Other qualified DDC users shall request through _____."

(4) "U. S. military agencies may obtain copies of this report directly from DDC. Other qualified users shall request through _____."

(5) "All distribution of this report is controlled. Qualified DDC users shall request through _____."

If the report has been furnished to the Office of Technical Services, Department of Commerce, for sale to the public, indicate this fact and enter the price, if known.

11. SUPPLEMENTARY NOTES: Use for additional explanatory notes.

12. SPONSORING MILITARY ACTIVITY: Enter the name of the departmental project office or laboratory sponsoring *(paying for)* the research and development. Include address.

13. ABSTRACT: Enter an abstract giving a brief and factual summary of the document indicative of the report, even though it may also appear elsewhere in the body of the technical report. If additional space is required, a continuation sheet shall be attached.

It is highly desirable that the abstract of classified reports be unclassified. Each paragraph of the abstract shall end with an indication of the military security classification of the information in the paragraph, represented as *(TS), (S), (C), or (U).*

There is no limitation on the length of the abstract. However, the suggested length is from 150 to 225 words.

14. KEY WORDS: Key words are technically meaningful terms or short phrases that characterize a report and may be used as index entries for cataloging the report. Key words must be selected so that no security classification is required. Identifiers, such as equipment model designation, trade name, military project code name, geographic location, may be used as key words but will be followed by an indication of technical context. The assignment of links, rules, and weights is optional.

Unclassified

Security Classification